UNIVERSITY OF MODENA AND REGGIO EMILIA

Department of Engineering "Enzo Ferrari"
PhD "Enzo Ferrari" in Industrial and Territorial Engineering

PhD Cycle XXXIII

Analysis of truss structures in finite elasticity with application to nanostructured materials

in collaboration with the Fuzhou University (China)

Candidate: Matteo Pelliciari

Italian tutor: Prof. Angelo Marcello Tarantino

Chinese tutor: Prof. Bruno Briseghella

PhD School Coordinator: Prof. Alberto Muscio

Abstract

The analysis of truss structures involving geometric and material nonlinearities is often performed by means of numerical approaches. Closed-form solutions of the equilibrium are provided only for simple benchmark problems, under the inconsistent hypothesis of linear constitutive behavior of the material. This hypothesis does not reflect the actual behavior of solids subjected to large deformations. Therefore, in this thesis, a fully nonlinear analytical formulation of the equilibrium and stability of truss structures is presented.

The bars of the truss are regarded as hyperelastic bodies composed of a homogeneous, compressible and isotropic material. Both displacement and deformation fields are large, without any restriction. The boundary-value problem is written and the equations governing the equilibrium are derived. The stability of the equilibrium configurations is assessed through an energy criterion. The formulation is firstly obtained for the von Mises (or two-bar) truss, which is the simplest case of truss structure. Despite its apparent simplicity, it exhibits various types of post-critical behaviors, such as snap-through and bifurcation. The formulation is then extended to the three-bar truss, which is an important benchmark test because it shows a number of critical points and stable asymmetric configurations. Several applications to rubber-like materials are performed by assuming a Mooney-Rivlin law for the stored energy function of the bars. The results are of great importance for the validation of finite element simulations and other numerical procedures.

The nonlinear formulation for the analysis of truss structures can be applied to the study of the mechanical behavior of nanostructured materials. In particular, this work is focused on the response of graphene subjected to large in-plane deformations. The atoms of the graphene lattice structure are viewed as nodes connected by continuum elements, whose properties are determined through an energy equivalence with the interatomic potential of the chemical bonds. The equilibrium solutions are given for the cases of uniaxial and equibiaxial tensile loads. The results show that graphene is isotropic only for small deformations, while anisotropy arises for large deformations. Multiple and unstable solutions are found after critical values of deformation.

Differently from many other studies in literature, the model presented in this work accounts for both geometric and material nonlinearities. This is necessary for an accurate analysis of the mechanical behavior of graphene, because it can easily experience strains larger than 15-20% prior to failure. The results allow therefore to deepen the understanding of the mechanics of deformation of graphene and provide insights into its complex mechanical behavior.

Sommario

Le strutture reticolari con non linearità geometriche e materiali vengono spesso analizzate mediante approcci numerici. Soluzioni dell'equilibrio in forma chiusa si trovano solamente per casi semplici di riferimento e sotto l'ipotesi di materiale elastico lineare. Tale ipotesi non è consistente con l'effettivo comportamento di solidi reali soggetti a grandi deformazioni. Pertanto, il lavoro di tesi riporta una formulazione analitica interamente non lineare per il problema dell'equilibrio e stabilità di strutture reticolari.

Le aste della struttura reticolare sono riguardate come solidi iperelastici di materiale omogeneo, comprimibile e isotropo. I campi di spostamento e deformazione sono considerati grandi, senza alcuna restrizione. Il problema a valori al contorno viene risolto, ricavando così le equazioni che governano l'equilibrio. Di conseguenza, la stabilità delle configurazioni di equilibrio viene studiata attraverso un criterio energetico. La formulazione è dapprima sviluppata per il traliccio di von Mises (arco a tre cerniere), il quale rappresenta il caso più semplice di struttura reticolare. Nonostante la sua apparente semplicità, tale sistema esibisce diversi tipi di comportamento post-critico, tra cui snap-through e biforcazione. La trattazione viene poi estesa al caso della struttura reticolare a tre aste, la quale rappresenta un importante problema di riferimento, poichè mostra diversi punti critici e configurazioni di equilibrio stabili non simmetriche. Si riportano alcune applicazioni della teoria a materiali polimerici, utilizzando il modello di Mooney-Rivlin per l'energia di deformazione elastica delle aste della struttura. I risultati hanno particolare importanza per quanto concerne la validazione di simulazioni agli elementi finiti o di altre procedure numeriche.

La trattazione non lineare per l'analisi di strutture reticolari in elasticità finita si applica anche allo studio del comportamento meccanico di materiali nanostrutturali. Nello specifico, in questo lavoro si analizza il grafene soggetto a grandi deformazioni piane. Gli atomi del reticolo cristallino esagonale rappresentano nodi connessi tra loro da elementi strutturali continui, le cui caratteristiche sono determinate attraverso un'equivalenza energetica con il potenziale interatomico dei legami chimici. L'equilibrio viene risolto per i casi di carico uniassiale e equibiassiale. I risultati del lavoro dimostrano l'isotropia del grafene per piccole deformazioni, proprietà che viene persa per grandi deformazioni dando origine a un comportamento anisotropo. Si osservano inoltre soluzioni multiple e instabili dopo valori critici di deformazione.

A differenza di molti altri studi in letteratura, il modello presentato in questo lavoro di tesi tiene conto delle non linearità geometriche e materiali. Ciò è necessario per una modellazione accurata del comportamento meccanico del grafene, in quanto questo materiale può raggiungere deformazioni a rottura superiori a 15-20%. I risultati dello studio permettono quindi di approfondire la comprensione dei meccanismi di deformazione del grafene e del suo complesso comportamento meccanico.

Contents

List of Figures

List of Tables

Acknowledgements

First of all, I must say thank you to my parents and my brother for their support throughout my graduate years and my PhD. I wish to express my deepest gratitude to Federico Falope, Federico Ferrari, Cesare Signorini and Stefano Sirotti, who helped me to get through the hard times with precious and wise advices. Thanks also to all my friends that brought happiness and joy to my life.

I would like to pay my special regards to professors Angelo Marcello Tarantino and Luca Lanzoni, who supported and encouraged my research. I owe my deepest gratitude to professor Bruno Briseghella, the pioneer that opened the door for many students to experience the life in China. During the times spent at the Fuzhou University (China), he supported me with kindness and patience.

The trips to China gave me the opportunity to experience new cultures and collect special memories. Thanks to all the Italian friends that shared such experiences with me, with particular reference to the two Luigis, my life's pillars, my heroes always ready to jump into action without fear and preconceptions. Deep thanks are also due to all the international friends in Fuzhou. I met so many people that any attempt to cite them all would be meaningless.

"The world is a dangerous place, not because of those who do evil, but because of those who look on and do nothing"

Albert Einstein

"I have from an early age abjured the use of meat, and the time will come when men such as I will look upon the murder of animals as they now look upon the murder of men"

Leonardo Da Vinci

"It is not your right – based on YOUR traditions, YOUR customs and YOUR habits – to deny animals THEIR freedom so you can harm them, enslave them and kill them. That's not what rights are about, that's injustice"

Gary Yourofsky

Chapter 1

Introduction

The nonlinear analysis of truss structures often requires the use of numerical approaches. Closed-form solutions are given only for simple benchmark problems, among which the most famous is certainly the von Mises truss [2, 3] (or two-bar truss). The only closed-form solutions that can be found in the literature are based on the assumption of linear elastic material [1, 4–6], which is not proper for solids subjected to large deformations.

In this thesis, an analytical formulation of the equilibrium and stability of planar truss structures is presented. Unlike the other models, both geometric and material nonlinearities are taken into account. The formulation is entirely developed in three-dimensional finite elasticity, with the assumption of isotropic and hyperelastic material. Exact descriptions of both kinematics and equilibrium are given. In this way, critical and post-critical behaviors of truss structures are accurately analyzed.

The analytical model for truss structures can be also applied to the analysis of the mechanical behavior of nanostructured materials subjected to large plane deformations. The case of graphene is studied in this thesis [7]. The original contribution lies in the fact that, differently from the other studies found in the literature, a fully nonlinear analytical approach to this problem is presented.

The thesis is structured as follows. In Chapter 2, the solution of the equilibrium and stability of the von Mises truss is presented. Applications and comparisons with others models are also given. Experimental and numerical analyses of the von Mises truss are carried out in Chapter 3. This provides a validation of the analytical approach presented in this thesis. The case of the three-bar truss is analyzed in Chapter 4, with a final application to the representative cell of the honeycomb nanostructure of graphene. The transition from macroscopic truss structures to nanostructures is completed in Chapter 5, where a molecular mechanics model for graphene subjected to large in-plane deformations is presented. Conclusions are drawn in Chapter 6.

Chapter 2

Equilibrium paths for the von Mises truss in finite elasticity

The equilibrium of the symmetric planar truss composed of two shallow bars and subjected to a concentrated load on its apex node (Fig. 2.1) represents a benchmark in the analysis of structural systems stability. This problem is classically known as the von Mises truss, referring to the scientist who first analyzed its structural stability [2].

In the present chapter, the basic concepts regarding the von Mises truss are introduced. The kinematics of the system is described by assuming two degrees of freedom for the apex node (horizontal and vertical components of displacement), from which the expressions of the longitudinal stretches of the bars are determined. The finite displacement fields and deformation gradients are derived regarding the bars as three-dimensional bodies and assuming homogeneous deformations, which implies that the Eulerian buckling is neglected. The boundary-value problem for the bodies subjected to uniaxial tractions is then formulated. The Piola-Kirchhoff and Cauchy stress tensors are computed and the relations governing the equilibrium of each body are derived. Consequently, the global equilibrium of the apex node of the truss in deformed configuration is expressed and the stability of the equilibrium solutions is assessed through the energy criterion.

Applications are performed by assuming the compressible Mooney-Rivlin law for the stored energy function of the bodies. Comparisons of the results with other models found in the literature are reported. Lastly, the whole finite theory proposed for the von Mises truss is linearized with the hypotheses of infinitesimal displacement and strain fields. Thereby, the classical linearized solution for the two-bar truss is recovered.

2.1 The von Mises truss

The von Mises truss is a bistable system and thus it is used to obtain structures with multiple stable configurations [8–11]. Applications can be found in different fields of engineering, such as lattice truss structures [12] and metamaterials [13, 14].

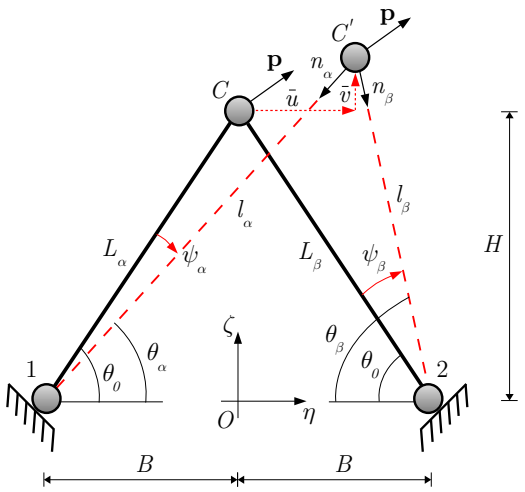

Figure 2.1: The von Mises truss in undeformed and deformed configurations. Central node C undergoes displacement $\mathbf{s}$, with components $\bar{u}$ and $\bar{v}$

Structural morphing applications are also of great interest [15–19]. For instance, Moser et al. [20] used a centrifugally actuated von Mises truss for the morphing mechanism of helicopter rotor blades.

When a vertical load is applied on the von Mises truss, the dominant form of instability is the snap-through [21], which does not involve any bifurcation of the equilibrium path. In fact, the von Mises truss has often been analyzed considering only one degree of freedom for the apex node, disregarding asymmetric deformations (see, among the others, Bellini [22], Savi et al. [23], Psotny [24] and Bazzucchi et al. [25]). However, Pecknold et al. [4] examined also the case of horizontal and combined vertical-horizontal loading condition. It was found out that the behavior of the truss drastically changes, showing a bifurcation instability.

Recently, formulations including more degrees of freedom for the apex node were developed. In particular, Ligarò and Valvo [5] analyzed an elastic space truss with the shape of a regular pyramid. Closed-form solutions under the hypotheses of linear material law, moderate axial deformation and large nodal displacements were found, considering different loading conditions. It was discovered that these systems may show various post-critical responses, not exhausted by the snap-through and bifurcation phenomena. For instance, the equilibrium paths may involve neutral branches, which are entirely composed of bifurcation or limit points. On the basis of the theory developed in [5], Kwasniewski [1] applied the same procedure to the planar von Mises truss, obtaining the complete equilibrium paths and studying the stability through the energy criterion. As a result, the primary branch is always the only path where stable solutions can be found. Instead, all the secondary equilibrium paths, which describe asymmetrical deformations, are unstable. Rezaiee-Pajand and Naghavi [6] found the solutions of eight individual trusses under various loading conditions, adopting the same assumptions of the works cited above. They also performed a validation of the results through a comparison with

the solutions obtained via the numerical arc-length technique.

The equilibrium solutions obtained in [1,4–6] are derived considering large nodal displacements. Nevertheless, it is assumed that the axial components of strain are relatively small. This is done by adopting the Green-Lagrange strain measure and a linear constitutive behavior of the material. Instead, in this work, a fully nonlinear finite theory for the von Mises truss is derived. Differently from the aforementioned works, both displacements and deformations are large, without any restriction. The bars are regarded as hyperelastic bodies composed of a general homogeneous compressible isotropic material. Thus, the hypothesis of linear constitutive law is not introduced.

2.2 Preliminaries and kinematics

Consider a von Mises truss consisting of two equal straight bars, denoted by the symbols α and β. The two bars are connected at the apex node C through a hinge and the truss is loaded by a dead force $[\mathbf{p}] = [p_\eta, p_\zeta]^T$, as shown in Fig. 2.1. Node C undergoes the displacement $\mathbf{s} = [\bar{u}, \bar{v}]^T$.

The lengths of the bars in the initial configuration are

$$L_\alpha = L_\beta = L = \sqrt{B^2 + H^2},$$

whereas the lengths of the bars in deformed configuration become

$$\begin{aligned} l_\alpha &= \sqrt{(B+\bar{u})^2 + (H+\bar{v})^2}, \\ l_\beta &= \sqrt{(B-\bar{u})^2 + (H+\bar{v})^2}. \end{aligned} \tag{2.1}$$

The principal stretches of the bodies are indicated with the symbols λ_j^γ, $\gamma = \alpha, \beta$ and $j = x, y, z$. The superscript represents the body while the subscript represents the local reference system for the γ-th body (Fig. 2.2), which is principal. Therefore, the longitudinal stretches are expressed by the following relations:

$$\begin{aligned} \lambda_z^\alpha &= \frac{l_\alpha}{L} = \sqrt{\frac{(B+\bar{u})^2 + (H+\bar{v})^2}{B^2 + H^2}}, \\ \lambda_z^\beta &= \frac{l_\beta}{L} = \sqrt{\frac{(B-\bar{u})^2 + (H+\bar{v})^2}{B^2 + H^2}}. \end{aligned} \tag{2.2}$$

The equilibrium in deformed configuration reads

$$\begin{aligned} p_\eta - n_\alpha c_\alpha + n_\beta c_\beta &= 0, \\ p_\zeta - n_\alpha s_\alpha - n_\beta s_\beta &= 0, \end{aligned} \tag{2.3}$$

where

$$\begin{aligned} c_\alpha &= \cos\theta_\alpha = \frac{B+\bar{u}}{\sqrt{(B+\bar{u})^2 + (H+\bar{v})^2}}, \qquad s_\alpha = \sin\theta_\alpha = \frac{H+\bar{v}}{\sqrt{(B+\bar{u})^2 + (H+\bar{v})^2}}, \\ c_\beta &= \cos\theta_\beta = \frac{B-\bar{u}}{\sqrt{(B-\bar{u})^2 + (H+\bar{v})^2}}, \qquad s_\beta = \sin\theta_\beta = \frac{H+\bar{v}}{\sqrt{(B-\bar{u})^2 + (H+\bar{v})^2}}, \end{aligned} \tag{2.4}$$

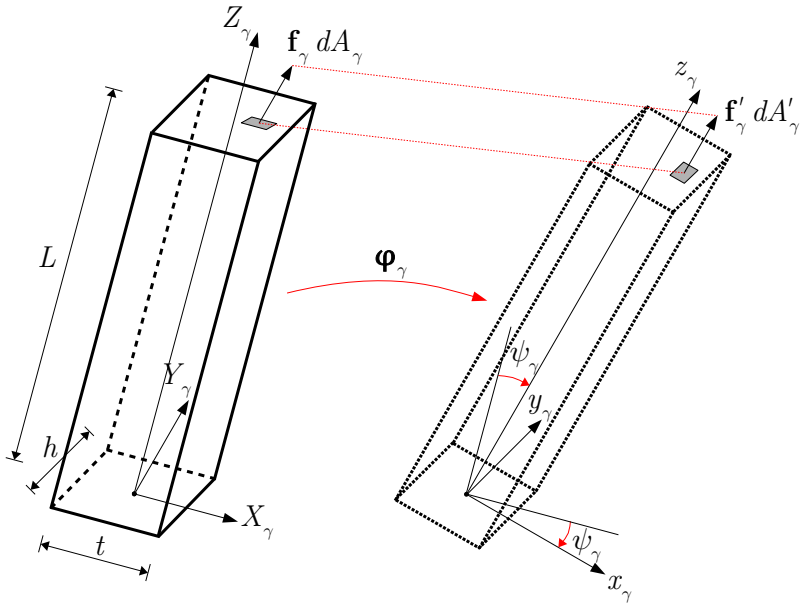

Figure 2.2: Homogeneous deformation of the bar $\mathcal{B}_\gamma$ ($\gamma = \alpha, \beta$) and surface tractions deriving from the external load $\mathbf{p}$. Each bar is subjected to a pure deformation and a rigid rotation, expressed by the rotation angle ψ_γ

and n_α, n_β are the axial forces acting on the bars. Note that, in the system (2.3), the dependence with respect to the displacement components $\bar{u}$ and $\bar{v}$ has been omitted for simplicity.

The two bars of the truss are regarded as three-dimensional bodies that are composed of the same homogeneous hyperelastic material, which is assumed frame-indifferent and isotropic [26, 27]. A material coordinate system $X_\gamma, Y_\gamma, Z_\gamma$ with the origin in the corresponding node 1 and 2 is defined for each body (Fig. 2.2). The two bodies are identified by the closure of the regions

$$\mathcal{B}_\gamma = \left\{ (X_\gamma, Y_\gamma, Z_\gamma) : |X_\gamma| < \frac{t}{2}, |Y_\gamma| < \frac{h}{2}, 0 < Z_\gamma < L \right\}, \quad \gamma = \alpha, \beta,$$

of the three-dimensional Eucledian space $\mathcal{E}$. The quantities t, h and L respectively indicate width, height and length of each body. The boundaries $\partial\mathcal{B}_\gamma$ are Lipschitz-continuous and the domain $\mathcal{B}_\gamma$ is nonempty, connected and bounded. Note that the cross sections of the bodies are assumed to be rectangular for the sake of simplicity, but the formulation can be easily extended to general shapes.

The undeformed configurations $\overline{\mathcal{B}}_\gamma$ are considered as reference configurations, while the deformed configurations are obtained through the deformations $\boldsymbol{\varphi}_\gamma : \overline{\mathcal{B}}_\gamma \to \mathcal{V}$[1], which are smooth enough, injective and orientation-preserving vector fields [28, 29]. The deformations are assumed to be homogeneous, namely the deformation gradients are constant, as actually occurs to bars subjected to axial forces.

[1] $\mathcal{V}$ indicates the vector space associated with $\mathcal{E}$.

Body forces are disregarded and it is supposed that the bodies are maintained in equilibrium under the sole action of surface tractions, which are the result of the application of the dead force $\mathbf{p}$ to the node C. The surface tractions are assumed to be uniformly and orthogonally distributed on the basis of the bodies $\mathcal{B}_\alpha$ and $\mathcal{B}_\beta$. Being $\mathbf{p}$ a dead force, it does not depend on the deformation of the truss. On the other hand, the axial forces n_α and n_β depend on the configuration assumed by the truss through the displacement components $\bar{u}$ and $\bar{v}$.

The deformation of a material point P belonging to a body is expressed by the well-known relationship

$$\boldsymbol{\varphi}_\gamma(P) = \mathbf{id}(P) + \mathbf{u}_\gamma(P), \quad \gamma = \alpha, \beta, \tag{2.5}$$

where $\mathbf{id}(P)$ is the position vector and $\mathbf{u}_\gamma(P)$ is the displacement vector with scalar components $u_\gamma(P)$, $v_\gamma(P)$ and $w_\gamma(P)$. By applying the material gradient operator $\mathbf{D}(\cdot)$ to (2.5) we obtain

$$\mathbf{F}_\gamma = \mathbf{I} + \mathbf{H}_\gamma, \quad \gamma = \alpha, \beta, \tag{2.6}$$

where $\mathbf{F}_\gamma : \overline{\mathcal{B}}_\gamma \to Lin^+$ and $\mathbf{H}_\gamma : \overline{\mathcal{B}}_\gamma \to Lin$ are the deformation and displacement gradients[2], respectively, while $\mathbf{I}$ is the identity tensor [30].

The displacement field of the γ-th body due to the deformation $\boldsymbol{\varphi}_\gamma$ (Fig. 2.2) is the following:

$$\begin{cases} u_\gamma = X_\gamma \left(\lambda_x^\gamma \cos\psi_\gamma - 1\right) + Z_\gamma \lambda_z^\gamma \sin\psi_\gamma \\ v_\gamma = Y_\gamma \left(\lambda_y^\gamma - 1\right) \\ w_\gamma = -X_\gamma \lambda_x^\gamma \sin\psi_\gamma + Z_\gamma \left(\lambda_z^\gamma \cos\psi_\gamma - 1\right), \quad \gamma = \alpha, \beta, \end{cases} \tag{2.7}$$

where the angle ψ_γ describes the rigid rotation of the γ-th body and it can be expressed as a function of $\bar{u}$ and $\bar{v}$. The material gradient of the displacement field (2.7) gives

$$[\mathbf{H}_\gamma] = \begin{bmatrix} \lambda_x^\gamma \cos\psi_\gamma - 1 & 0 & \lambda_z^\gamma \sin\psi_\gamma \\ 0 & \lambda_y^\gamma - 1 & 0 \\ -\lambda_x^\gamma \sin\psi_\gamma & 0 & \lambda_z^\gamma \cos\psi_\gamma - 1 \end{bmatrix}, \quad \gamma = \alpha, \beta.$$

Using (2.6), the components of the deformation gradient are easily obtained

$$[\mathbf{F}_\gamma] = \begin{bmatrix} \lambda_x^\gamma \cos\psi_\gamma & 0 & \lambda_z^\gamma \sin\psi_\gamma \\ 0 & \lambda_y^\gamma & 0 \\ -\lambda_x^\gamma \sin\psi_\gamma & 0 & \lambda_z^\gamma \cos\psi_\gamma \end{bmatrix}, \quad \gamma = \alpha, \beta. \tag{2.8}$$

The deformation gradient of the γ-th body (2.8) can be expressed through the polar decomposition [31, 32] as the product of the rotation tensor,

$$[\mathbf{R}_\gamma] = \begin{bmatrix} \cos\psi_\gamma & 0 & \sin\psi_\gamma \\ 0 & 1 & 0 \\ -\sin\psi_\gamma & 0 & \cos\psi_\gamma \end{bmatrix}, \tag{2.9}$$

[2] Lin^+ is the set of all the second order tensors with positive determinant.

by the stretch tensor,

$$[\mathbf{U}_\gamma] = \begin{bmatrix} \lambda_x^\gamma & 0 & 0 \\ 0 & \lambda_y^\gamma & 0 \\ 0 & 0 & \lambda_z^\gamma \end{bmatrix}, \quad \gamma = \alpha, \beta.$$

2.3 The boundary-value problem

Under the assumptions of frame-indifference and isotropy, the stored energy function ω_γ of the γ-th body depends only on the principal invariants $\imath_j^\gamma (j = 1,2,3)$ of the left Cauchy-Green deformation tensor $\mathbf{B}_\gamma = \mathbf{F}_\gamma \mathbf{F}_\gamma^T$. Thus, $\omega_\gamma = \hat{\omega}_\gamma(\imath_1^\gamma, \imath_2^\gamma, \imath_3^\gamma)$. The (first) Piola-Kirchhoff stress tensor [33] related to the γ-th body is expressed by the constitutive equation [34]

$$\mathbf{T}_{R\gamma}(\mathbf{F}_\gamma) = \frac{\partial \omega_\gamma}{\partial \mathbf{F}_\gamma} = 2\left[\left(\frac{\partial \omega_\gamma}{\partial \imath_1^\gamma} + \imath_1^\gamma \frac{\partial \omega_\gamma}{\partial \imath_2}\right)\mathbf{F}_\gamma - \frac{\partial \omega_\gamma}{\partial \imath_2^\gamma}\mathbf{B}_\gamma \mathbf{F}_\gamma + \imath_3^\gamma \frac{\partial \omega_\gamma}{\partial \imath_3^\gamma}\mathbf{F}_\gamma^{-T}\right], \quad \gamma = \alpha, \beta, \tag{2.10}$$

where

$$\begin{aligned} \imath_1^\gamma &= \|\mathbf{F}_\gamma\|^2 = (\lambda_x^\gamma)^2 + \left(\lambda_y^\gamma\right)^2 + (\lambda_z^\gamma)^2, \\ \imath_2^\gamma &= \left\|\mathbf{F}_\gamma^*\right\|^2 = \left(\lambda_x^\gamma \lambda_y^\gamma\right)^2 + (\lambda_x^\gamma \lambda_z^\gamma)^2 + \left(\lambda_y^\gamma \lambda_z^\gamma\right)^2, \\ \imath_3^\gamma &= (\det \mathbf{F}_\gamma)^2 = \left(\lambda_x^\gamma \lambda_y^\gamma \lambda_z^\gamma\right)^2, \end{aligned} \tag{2.11}$$

in which $\|\mathbf{F}_\gamma\| = \operatorname{tr}\left(\mathbf{F}_\gamma^T \mathbf{F}_\gamma\right)^{1/2}$ and $\mathbf{F}_\gamma^* = (\det \mathbf{F}_\gamma)\mathbf{F}_\gamma^{-T}$ denotes the cofactor of the deformation gradient $\mathbf{F}_\gamma$.

In the absence of body forces, the equilibrium of each body is locally satisfied if the following vectorial equation holds [35]:

$$\mathrm{Div}\mathbf{T}_{R\gamma}(\mathbf{F}_\gamma) = \mathbf{o}, \quad \gamma = \alpha, \beta, \tag{2.12}$$

while the boundary conditions require that

$$\begin{aligned} &\mathbf{T}_{R\gamma}\mathbf{n}_X^\gamma = \mathbf{o}, \\ &\mathbf{T}_{R\gamma}\mathbf{n}_Y^\gamma = \mathbf{o}, \\ &\mathbf{T}_{R\gamma}\mathbf{n}_Z^\gamma = \mathbf{f}_\gamma, \quad \gamma = \alpha, \beta, \end{aligned} \tag{2.13}$$

where $\mathbf{f}_\gamma$ is the surface traction acting on the basis of the γ-th body in undeformed configuration (Fig. 2.2) and $\mathbf{n}_j^\gamma$, with $j = X, Y, Z$, are the outward unit normals of the γ-th body relative to the faces with positive normal. Note that every quantity in (2.13) depends on $\bar{u}$ and $\bar{v}$.

System (2.12) is trivially satisfied since the deformations are assumed to be homogeneous. The outward unit normals in deformed configuration $\left(\mathbf{n}_j^\gamma\right)'$ are obtained through a rigid rotation of the unit normals in reference configuration

$$\left(\mathbf{n}_j^\gamma\right)' = \mathbf{R}_\gamma \mathbf{n}_j^\gamma, \quad \gamma = \alpha, \beta \quad \text{and} \quad j = X, Y, Z, \tag{2.14}$$

where the rotation tensor $\mathbf{R}_\gamma$ is expressed by (2.9). Being the external surface traction $\mathbf{f}'_\gamma$ coaxial with the z_γ axis, using (2.14), the boundary conditions (2.13) can be rewritten as

$$\begin{aligned}
&\mathbf{T}_{R\gamma}\,\mathbf{n}_X^\gamma = \mathbf{o},\\
&\mathbf{T}_{R\gamma}\,\mathbf{n}_Y^\gamma = \mathbf{o},\\
&\mathbf{T}_{R\gamma}\,\mathbf{n}_Z^\gamma = f_\gamma \sin\psi_\gamma\,\mathbf{n}_X^\gamma + f_\gamma\cos\psi_\gamma\,\mathbf{n}_Z^\gamma, \quad \gamma=\alpha,\beta,
\end{aligned} \tag{2.15}$$

where $f_\gamma = \|\mathbf{f}_\gamma\|$.

The constitutive relation (2.10) and the boundary conditions (2.15) provide

$$\mathbf{T}_{R\gamma} = 2\left[(\omega_{\gamma,1} + \imath_1^\gamma\omega_{\gamma,2})\,\mathbf{F}_\gamma - \omega_{\gamma,2}\mathbf{F}_\gamma\mathbf{F}_\gamma^T\mathbf{F}_\gamma + \imath_3^\gamma\omega_{\gamma,3}\mathbf{F}_\gamma^{-T}\right] = \mathbf{S}_\gamma, \tag{2.16}$$

where

$$[\mathbf{S}_\gamma] = \begin{bmatrix} 0 & 0 & f_\gamma\sin\psi_\gamma \\ 0 & 0 & 0 \\ 0 & 0 & f_\gamma\cos\psi_\gamma \end{bmatrix} \tag{2.17}$$

and $\omega_{\gamma,j} = \dfrac{\partial\omega_\gamma}{\partial\imath_j^\gamma}$, for $\gamma=\alpha,\beta$ and $j=1,2,3$. Substituting (2.8) into (2.16), the following system of equations is obtained:

$$\begin{aligned}
&2\cos\psi_\gamma\left[(\omega_{\gamma,1} + \imath_1^\gamma\omega_{\gamma,2})\,\lambda_x^\gamma - \omega_{\gamma,2}\,(\lambda_x^\gamma)^3 + \imath_3^\gamma\omega_{\gamma,3}\,(\lambda_x^\gamma)^{-1}\right] = 0,\\
&2\sin\psi_\gamma\left[(\omega_{\gamma,1} + \imath_1^\gamma\omega_{\gamma,2})\,\lambda_x^\gamma - \omega_{\gamma,2}\,(\lambda_x^\gamma)^3 + \imath_3^\gamma\omega_{\gamma,3}\,(\lambda_x^\gamma)^{-1}\right] = 0,\\
&2\left[(\omega_{\gamma,1} + \imath_1^\gamma\omega_{\gamma,2})\,\lambda_y^\gamma - \omega_{\gamma,2}\left(\lambda_y^\gamma\right)^3 + \imath_3^\gamma\omega_{\gamma,3}\left(\lambda_y^\gamma\right)^{-1}\right] = 0,\\
&2\cos\psi_\gamma\left[(\omega_{\gamma,1} + \imath_1^\gamma\omega_{\gamma,2})\,\lambda_z^\gamma - \omega_{\gamma,2}\,(\lambda_z^\gamma)^3 + \imath_3^\gamma\omega_{\gamma,3}\,(\lambda_z^\gamma)^{-1}\right] = f_\gamma\cos\psi_\gamma,\\
&2\sin\psi_\gamma\left[(\omega_{\gamma,1} + \imath_1^\gamma\omega_{\gamma,2})\,\lambda_z^\gamma - \omega_{\gamma,2}\,(\lambda_z^\gamma)^3 + \imath_3^\gamma\omega_{\gamma,3}\,(\lambda_z^\gamma)^{-1}\right] = f_\gamma\sin\psi_\gamma, \quad \gamma=\alpha,\beta.
\end{aligned} \tag{2.18}$$

System (2.18) must hold for every value of the displacement components $\bar{u}$ and $\bar{v}$, and therefore for every rotation angle ψ_γ. Thus, it reduces to the three equations

$$\begin{aligned}
&(\omega_{\gamma,1} + \imath_1^\gamma\omega_{\gamma,2})\,\lambda_x^\gamma - \omega_{\gamma,2}\,(\lambda_x^\gamma)^3 + \imath_3^\gamma\omega_{\gamma,3}\,(\lambda_x^\gamma)^{-1} = 0,\\
&(\omega_{\gamma,1} + \imath_1^\gamma\omega_{\gamma,2})\,\lambda_y^\gamma - \omega_{\gamma,2}\left(\lambda_y^\gamma\right)^3 + \imath_3^\gamma\omega_{\gamma,3}\left(\lambda_y^\gamma\right)^{-1} = 0,\\
&2\left[(\omega_{\gamma,1} + \imath_1^\gamma\omega_{\gamma,2})\,\lambda_z^\gamma - \omega_{\gamma,2}\,(\lambda_z^\gamma)^3 + \imath_3^\gamma\omega_{\gamma,3}\,(\lambda_z^\gamma)^{-1}\right] = f_\gamma, \quad \gamma=\alpha,\beta,
\end{aligned} \tag{2.19}$$

which correspond to the result obtained by Lanzoni and Tarantino [36], who analyzed the equilibrium configurations of a damaged body under uniaxial tractions. In fact, for every configuration of the truss ($\bar{u}$, $\bar{v}$), the two bodies are subjected to a pair of equal and opposite surface forces that act normally and are uniformly distributed on the two basis (traction problem).

We demonstrate now that the transversal stretches λ_x^γ and λ_y^γ are equal. Suppose that the three principal stretches are different (i.e., $\lambda_x^\gamma \neq \lambda_y^\gamma \neq \lambda_z^\gamma$). The first two equations of the system (2.19) may be simplified dividing them by $(\lambda_x^\gamma - \lambda_y^\gamma)$ and

$(\lambda_x^\gamma + \lambda_y^\gamma)$, respectively. Then, $(\lambda_z^\gamma)^2$ can be derived from the first equation and replaced in the second one, obtaining

$$\omega_{\gamma,1}\omega_{\gamma,3} - \omega_{\gamma,2}^2 = 0,$$

which obviously cannot be satisfied by a generic stored energy function. Therefore, we conclude that, in general, the problem does not admit solutions with $\lambda_x^\gamma \neq \lambda_y^\gamma$. Note that, in the linear theory, the hypothesis of isotropy is sufficient to impose $\lambda_x^\gamma = \lambda_y^\gamma$, while in our case (finite elasticity) this comes as a results of the equilibrium.

Since the transversal stretches are equal, we can write that $\lambda_x^\gamma = \lambda_y^\gamma = \lambda^\gamma$, $\gamma = \alpha, \beta$. System (2.19) reduces to

$$\omega_{\gamma,1} + \left[(\lambda_z^\gamma)^2 + (\lambda^\gamma)^2\right]\omega_{\gamma,2} + (\lambda^\gamma)^2(\lambda_z^\gamma)^2\omega_{\gamma,3} = 0, \tag{2.20}$$

$$2\lambda_z^\gamma\left[\omega_{\gamma,1} + 2(\lambda^\gamma)^2\omega_{\gamma,2} + (\lambda^\gamma)^4\omega_{\gamma,3}\right] = f_\gamma, \quad \gamma = \alpha, \beta. \tag{2.21}$$

Equations (2.20) and (2.21) provide the equilibrium configurations of the γ-th body of the von Mises truss.

The boundary-value problem described above is referred to the undeformed configuration. Thus, a Lagrangian analysis has been performed, where the consistent stress measure is given by the Piola-Kirchhoff stress tensor. Now, switching to the deformed configuration, the Cauchy stress measure will be adopted. The Cauchy stress tensor is obtained from the Piola-Kirchhoff stress tensor by the transformation

$$\mathbf{T}_{R\gamma} = \mathbf{T}_\gamma \mathbf{F}_\gamma^*, \quad \gamma = \alpha, \beta. \tag{2.22}$$

Substituting (2.17) into (2.22), we obtain the Cauchy stress tensor related to the γ-th body

$$[\mathbf{T}_\gamma] = \begin{bmatrix} \dfrac{f_\gamma \sin^2\psi_\gamma}{(\lambda^\gamma)^2} & 0 & \dfrac{f_\gamma \sin\psi_\gamma\cos\psi_\gamma}{(\lambda^\gamma)^2} \\ 0 & 0 & 0 \\ \dfrac{f_\gamma \sin\psi_\gamma\cos\psi_\gamma}{(\lambda^\gamma)^2} & 0 & \dfrac{f_\gamma \cos^2\psi_\gamma}{(\lambda^\gamma)^2} \end{bmatrix}, \quad \gamma = \alpha, \beta. \tag{2.23}$$

The boundary conditions in deformed configuration are

$$\begin{aligned} &\mathbf{T}_\gamma (\mathbf{n}_X^\gamma)' = \mathbf{o}, \\ &\mathbf{T}_\gamma (\mathbf{n}_Y^\gamma)' = \mathbf{o}, \\ &\mathbf{T}_\gamma (\mathbf{n}_Z^\gamma)' = f_\gamma' (\mathbf{n}_Z^\gamma)', \quad \gamma = \alpha, \beta, \end{aligned} \tag{2.24}$$

where f_γ' is the modulus of the surface traction acting on the basis of the body in deformed configuration. The following relation between the traction acting on undeformed and deformed configuration holds:

$$f_\gamma' = \frac{f_\gamma}{\left|\mathbf{F}_\gamma^* \mathbf{n}_Z^\gamma\right|} = \frac{f_\gamma}{(\lambda^\gamma)^2}, \quad \gamma = \alpha, \beta. \tag{2.25}$$

Note that, by substituting (2.23), (2.25) and (2.14) into (2.24), the corresponding boundary conditions in undeformed configurations (2.13) are retrieved.

Since the surface tractions are assumed to be uniformly distributed over the cross sections, the modulus of the axial force acting on the γ-th body is

$$n_\gamma = f'_\gamma A'_\gamma, \quad \gamma = \alpha, \beta, \tag{2.26}$$

where A' is the area of the basis of the γ-th body in deformed configuration. Applying the Nanson's formula for the transformation of the area element dA

$$\left(\mathbf{n}_j^\gamma\right)' dA'_\gamma = \mathbf{F}^*_\gamma \mathbf{n}_j^\gamma dA_\gamma, \quad \gamma = \alpha, \beta \quad \text{and} \quad j = X, Y, Z, \tag{2.27}$$

the following relation is obtained:

$$A'_\gamma = (\lambda^\gamma)^2 A = (\lambda^\gamma)^2 th, \quad \gamma = \alpha, \beta, \tag{2.28}$$

being $A = th$ the area of the basis of each body in undeformed configuration. Hence, using (2.28) and (2.25), the expression of the axial force (2.26) becomes

$$n_\gamma = f_\gamma th, \quad \gamma = \alpha, \beta. \tag{2.29}$$

The eigenvalues of the Cauchy stress tensor, that represent the principal stresses, are evaluated as roots of the characteristic polynomial. Consequently, the Cauchy stress tensor (2.23) can be expressed in diagonal form through its spectral decomposition

$$[\mathbf{T}_\gamma] = \begin{bmatrix} 0 & 0 & 0 \\ 0 & 0 & 0 \\ 0 & 0 & \dfrac{f_\gamma}{(\lambda^\gamma)^2} \end{bmatrix}, \quad \gamma = \alpha, \beta.$$

The following matrix is determined:

$$[\mathbf{D}_\gamma] = \frac{1}{\sqrt{1+\tan^2\psi_\gamma}} \begin{bmatrix} \cot\psi_\gamma & 0 & \tan\psi_\gamma \\ 0 & \sqrt{1+\tan^2\psi_\gamma} & 0 \\ -1 & 0 & 1 \end{bmatrix}, \quad \gamma = \alpha, \beta,$$

whose columns are the eigenvectors associated to the eigenvalues. These eigenvectors represent the principal directions, along which the principal stresses take place. Note that the three principal directions $\left(\frac{\cot\psi_\gamma}{\sqrt{1+\tan^2\psi_\gamma}}, 0, -\frac{1}{\sqrt{1+\tan^2\psi_\gamma}}\right)$, $(0,1,0)$ and $\left(\frac{\tan\psi_\gamma}{\sqrt{1+\tan^2\psi_\gamma}}, 0, \frac{1}{\sqrt{1+\tan^2\psi_\gamma}}\right)$ correspond to the directions x_γ, y_γ and z_γ of the local reference system of the γ-th body.

2.4 Equilibrium equations and stability analysis

From equation (2.20), the transversal stretch can be expressed as a function of the longitudinal stretch

$$\lambda_x^\gamma = \lambda_y^\gamma = \lambda^\gamma = \sqrt{-\frac{\omega_{\gamma,1} + (\lambda_z^\gamma)^2 \omega_{\gamma,2}}{\omega_{\gamma,2} + (\lambda_z^\gamma)^2 \omega_{\gamma,3}}}, \quad \gamma = \alpha, \beta. \tag{2.30}$$

Note that, in general, $\omega_{\gamma,j}$ $(j=1,2,3)$ is a function of λ^γ. Hence, equation (2.30) does not provide an explicit expression for λ^γ and the existence of a solution is not ensured for an arbitrary (isotropic) stored energy function. Therefore, it is assumed that the constitutive response of the material is such as to ensure the existence of a unique solution to equation (2.30).

Substituting (2.30) into (2.21) and using (2.29), the following relation is derived:

$$n_\gamma = -\frac{2th\lambda_z^\gamma\left(\omega_{\gamma,2}^2-\omega_{\gamma,1}\omega_{\gamma,3}\right)\left[\omega_{\gamma,1}+2\left(\lambda_z^\gamma\right)^2\omega_{\gamma,2}+\left(\lambda_z^\gamma\right)^4\omega_{\gamma,3}\right]}{\left[\omega_{\gamma,2}+\left(\lambda_z^\gamma\right)^2\omega_{\gamma,3}\right]^2}, \quad \gamma=\alpha,\beta. \tag{2.31}$$

Using (2.31) and the geometrical relations

$$c_\alpha=\frac{B+\bar{u}}{\lambda_z^\alpha L}, \qquad s_\alpha=\frac{H+\bar{v}}{\lambda_z^\alpha L}, \qquad c_\beta=\frac{B-\bar{u}}{\lambda_z^\beta L}, \qquad s_\beta=\frac{H+\bar{v}}{\lambda_z^\beta L},$$

the equilibrium equations of the von Mises truss (2.3) become

$$\begin{aligned} &p_\eta+\frac{2th}{L}\left[G_\alpha\left(B+\bar{u}\right)-G_\beta\left(B-\bar{u}\right)\right]=0,\\ &p_\zeta+\frac{2th}{L}\left(G_\alpha+G_\beta\right)\left(H+\bar{v}\right)=0, \end{aligned} \tag{2.32}$$

where

$$G_\gamma=\frac{\left(\omega_{\gamma,2}^2-\omega_{\gamma,1}\omega_{\gamma,3}\right)\left[\omega_{\gamma,1}+2\left(\lambda_z^\gamma\right)^2\omega_{\gamma,2}+\left(\lambda_z^\gamma\right)^4\omega_{\gamma,3}\right]}{\left[\omega_{\gamma,2}+\left(\lambda_z^\gamma\right)^2\omega_{\gamma,3}\right]^2}, \quad \gamma=\alpha,\beta.$$

The equilibrium of the system can be also derived through the total potential energy. Being the deformation homogeneous, the determination of the internal deformation energy of the γ-th body is immediate

$$W_\gamma=V_\gamma\omega_\gamma=thL\omega_\gamma, \quad \gamma=\alpha,\beta,$$

where V_γ denotes the volume of each body in undeformed configuration. The total potential energy of the system is then defined by the following functional:

$$\Pi(\bar{u},\bar{v})=\sum_\gamma W_\gamma-\mathbf{p}\cdot\mathbf{s}=thL\sum_\gamma\omega_\gamma-p_\eta\bar{u}-p_\zeta\bar{v}, \quad \gamma=\alpha,\beta.$$

The equilibrium equations are obtained from the stationarity of the total potential energy. Hence, the partial derivatives of $\Pi(\bar{u},\bar{v})$ are

$$\begin{aligned} &\frac{\partial\Pi}{\partial\bar{u}}=thL\sum_\gamma\frac{\partial\omega_\gamma}{\partial\bar{u}}-p_\eta,\\ &\frac{\partial\Pi}{\partial\bar{v}}=thL\sum_\gamma\frac{\partial\omega_\gamma}{\partial\bar{v}}-p_\zeta, \quad \gamma=\alpha,\beta, \end{aligned} \tag{2.33}$$

where the derivatives of the stored energy function ω_γ with respect to the displacement components $\bar{u}$ and $\bar{v}$ can be computed using the chain rule

$$\begin{aligned}
\frac{\partial \omega_\gamma}{\partial \bar{u}} &= \sum_{j=1}^{3} \omega_{\gamma,j} \frac{\partial i_j^\gamma}{\partial \bar{u}} = \sum_{j=1}^{3} \omega_{\gamma,j} \sum_k \frac{\partial i_j^\gamma}{\partial \lambda_k^\gamma} \frac{\partial \lambda_k^\gamma}{\partial \bar{u}}, \\
\frac{\partial \omega_\gamma}{\partial \bar{v}} &= \sum_{j=1}^{3} \omega_{\gamma,j} \frac{\partial i_j^\gamma}{\partial \bar{v}} = \sum_{j=1}^{3} \omega_{\gamma,j} \sum_k \frac{\partial i_j^\gamma}{\partial \lambda_k^\gamma} \frac{\partial \lambda_k^\gamma}{\partial \bar{v}}, \\
&\gamma = \alpha, \beta \quad \text{and} \quad k = x, y, z.
\end{aligned} \tag{2.34}$$

From (2.2), the following derivatives of the longitudinal stretches are computed:

$$\frac{\partial \lambda_z^\alpha}{\partial \bar{u}} = \frac{B + \bar{u}}{\lambda_z^\alpha L^2}, \qquad \frac{\partial \lambda_z^\beta}{\partial \bar{u}} = -\frac{B - \bar{u}}{\lambda_z^\beta L^2}, \qquad \frac{\partial \lambda_z^\alpha}{\partial \bar{v}} = \frac{H + \bar{v}}{\lambda_z^\alpha L^2}, \qquad \frac{\partial \lambda_z^\beta}{\partial \bar{v}} = \frac{H + \bar{v}}{\lambda_z^\beta L^2}. \tag{2.35}$$

Being the transversal stretches expressed as functions of the longitudinal stretches through (2.30), the following derivatives can be evaluated:

$$\frac{\partial \lambda_x^\gamma}{\partial \bar{u}} = \frac{\partial \lambda_y^\gamma}{\partial \bar{u}} = \frac{\partial \lambda_\gamma}{\partial \bar{u}} = \frac{\partial \lambda_\gamma}{\partial \lambda_z^\gamma} \frac{\partial \lambda_z^\gamma}{\partial \bar{u}}, \qquad \frac{\partial \lambda_x^\gamma}{\partial \bar{v}} = \frac{\partial \lambda_y^\gamma}{\partial \bar{v}} = \frac{\partial \lambda_\gamma}{\partial \bar{v}} = \frac{\partial \lambda_\gamma}{\partial \lambda_z^\gamma} \frac{\partial \lambda_z^\gamma}{\partial \bar{v}}, \quad \gamma = \alpha, \beta. \tag{2.36}$$

The derivatives of the invariants with respect to the stretches $\dfrac{\partial i_j^\gamma}{\partial \lambda_k^\gamma}$ ($\gamma = \alpha, \beta$, $j = 1, 2, 3$ and $k = x, y, z$) are computed through (2.11). At this point, substituting (2.35) and (2.36) into (2.34), it is straightforward to verify that the stationarity of the total potential energy (2.33) corresponds to the equilibrium equations (2.32).

The solutions of system (2.32) represent the equilibrium paths. In this section, the stability of the equilibrium paths will be assessed employing the energy criterion, which states that a deformation is locally stable if it renders the total potential energy a minimum among a class of neighboring deformations [37, 38]. In other terms, an equilibrium configuration is stable if the Hessian matrix $\mathbf{K}$ of the total potential energy $\Pi(\bar{u}, \bar{v})$ is positive definite [39–42]. Thus, the stability of the equilibrium paths can be analyzed through the eigenvalues of the matrix $\mathbf{K}$, which is defined as

$$[\mathbf{K}] = \begin{bmatrix} \dfrac{\partial^2 \Pi}{\partial \bar{u}^2} & \dfrac{\partial^2 \Pi}{\partial \bar{u} \partial \bar{v}} \\ \dfrac{\partial^2 \Pi}{\partial \bar{v} \partial \bar{u}} & \dfrac{\partial^2 \Pi}{\partial \bar{v}^2} \end{bmatrix}. \tag{2.37}$$

Note that the load potential energy has a linear dependence with the displacement components $\bar{u}$ and $\bar{v}$, therefore $\mathbf{K}$ does not depend on the load vector.

In the following part of this section, the displacement components $\bar{u}$ and $\bar{v}$ will be replaced by the symbols u_1 and u_2, in order to express the derivatives with a more compact form. Given the above, the second partial derivatives of the total potential energy read

$$\frac{\partial^2 \Pi}{\partial u_j \partial u_i} = thL \sum_\gamma \frac{\partial^2 \omega_\gamma}{\partial u_j \partial u_i}, \quad \gamma = \alpha, \beta \quad \text{and} \quad i, j = 1, 2. \tag{2.38}$$

Applying the Faà di Bruno's formula [43] for the second derivative, the following expression is obtained:

$$\frac{\partial^2\omega_\gamma}{\partial u_j\partial u_i}=\sum_{h=1}^{3}\sum_{k=1}^{3}\omega_{\gamma,kh}\frac{\partial\imath_k^\gamma}{\partial u_j}\frac{\partial\imath_h^\gamma}{\partial u_i}+\sum_{h=1}^{3}\omega_{\gamma,h}\frac{\partial^2\imath_h^\gamma}{\partial u_j\partial u_i},\quad i,j=1,2, \tag{2.39}$$

where $\omega_{\gamma,kh}=\dfrac{\partial^2\omega_\gamma}{\partial\imath_k^\gamma\partial\imath_h^\gamma}$. Using the chain rule and again the Faà di Bruno's formula, (2.39) assumes the form

$$\begin{aligned}\frac{\partial^2\omega_\gamma}{\partial u_j\partial u_i}=&\sum_{h=1}^{3}\sum_{k=1}^{3}\omega_{\gamma,kh}\left(\sum_l\frac{\partial\imath_k^\gamma}{\partial\lambda_l^\gamma}\frac{\partial\lambda_l^\gamma}{\partial u_j}\right)\left(\sum_p\frac{\partial\imath_h^\gamma}{\partial\lambda_p^\gamma}\frac{\partial\lambda_p^\gamma}{\partial u_i}\right)\\&+\sum_{h=1}^{3}\omega_{\gamma,h}\left(\sum_r\sum_s\frac{\partial^2\imath_h^\gamma}{\partial\lambda_s^\gamma\partial\lambda_r^\gamma}\frac{\partial\lambda_s^\gamma}{\partial u_j}\frac{\partial\lambda_r^\gamma}{\partial u_i}+\sum_r\frac{\partial\imath_h^\gamma}{\partial\lambda_r^\gamma}\frac{\partial^2\lambda_r^\gamma}{\partial u_j\partial u_i}\right),\\&i,j=1,2\quad\text{and}\quad l,p,r,s=x,y,z.\end{aligned} \tag{2.40}$$

Substituting (2.40) into (2.38), the following result is achieved:

$$\begin{aligned}\frac{\partial^2\Pi}{\partial u_j\partial u_i}=thL\sum_\gamma\Bigg[&\sum_{h=1}^{3}\sum_{k=1}^{3}\omega_{\gamma,kh}\left(\sum_l\frac{\partial\imath_k^\gamma}{\partial\lambda_l^\gamma}\frac{\partial\lambda_l^\gamma}{\partial u_j}\right)\left(\sum_p\frac{\partial\imath_h^\gamma}{\partial\lambda_p^\gamma}\frac{\partial\lambda_p^\gamma}{\partial u_i}\right)\\&+\sum_{h=1}^{3}\omega_{\gamma,h}\left(\sum_r\sum_s\frac{\partial^2\imath_h^\gamma}{\partial\lambda_s^\gamma\partial\lambda_r^\gamma}\frac{\partial\lambda_s^\gamma}{\partial u_j}\frac{\partial\lambda_r^\gamma}{\partial u_i}+\sum_r\frac{\partial\imath_h^\gamma}{\partial\lambda_r^\gamma}\frac{\partial^2\lambda_r^\gamma}{\partial u_j\partial u_i}\right)\Bigg],\\&\gamma=\alpha,\beta,\quad i,j=1,2\quad\text{and}\quad l,p,r,s=x,y,z.\end{aligned} \tag{2.41}$$

Equation (2.41) expresses the scalar components of the Hessian matrix (2.37). Once computed these components, the characteristic equation is expressed as

$$\det\left(\mathbf{K}-\tau\mathbf{I}\right)=0, \tag{2.42}$$

where $\mathbf{I}$ is the identity tensor. Note that (2.42) is a second degree polynomial equation. Therefore, an equilibrium configuration characterized by a certain pair of values for $\bar{u}$ and $\bar{v}$ is stable if both the roots $\tau_1(\bar{u},\bar{v})$ and $\tau_2(\bar{u},\bar{v})$ of (2.42) are positive.

2.5 Application to Mooney-Rivlin materials

In this section, the Mooney-Rivlin constitutive law will be employed for both the bars of the von Mises truss. Thus, the equilibrium equations will be specialized to the case of a Mooney-Rivlin material. Afterwards, numerical applications for two relevant loading conditions (i.e. vertical and horizontal loads) will be presented. The equilibrium paths and the stability of the solutions will be analyzed.

The stored energy function for a compressible Mooney-Rivlin material is [44–49]

$$\omega(\imath_1,\imath_2,\imath_3)=a\,\imath_1+b\,\imath_2+\Gamma\left(\mu\right), \tag{2.43}$$

where $\mu = \sqrt{\imath_3} = \det \mathbf{F} = \lambda_x \lambda_y \lambda_z$ and Γ is a convex function which satisfies a growth condition for both $\mu \to 0^+$ and $\mu \to \infty^+$. Ciarlet and Geymonat [50] proposed the following expression:

$$\Gamma(\mu) = c\mu^2 - q \ln \mu. \tag{2.44}$$

Constants a, b, c and q are positive scalars. Substituting (2.44) into (2.43), the expression of the stored energy function turns into

$$\omega(\imath_1, \imath_2, \imath_3) = a\imath_1 + b\imath_2 + c\mu^2 - q \ln \mu.$$

A constant term is added so that the stored energy in undeformed configuration vanishes[3]

$$\omega(\imath_1, \imath_2, \imath_3) = a\imath_1 + b\imath_2 + c\mu^2 - q \ln \mu - (3a + 3b + c). \tag{2.45}$$

By computing the derivatives of the stored energy function (2.45) as

$$\omega_{,1} = a, \qquad \omega_{,2} = b, \qquad \omega_{,3} = c - \frac{q}{2\mu^2} \tag{2.46}$$

and by substituting them into (2.30), the relation between longitudinal and transversal stretches becomes

$$\lambda = \sqrt{\frac{-(a + b\lambda_z^2) + \sqrt{(a + b\lambda_z^2)^2 + 2q(b + c\lambda_z^2)}}{2(b + c\lambda_z^2)}}. \tag{2.47}$$

In order to have $\lambda = 1$ when no longitudinal deformation occurs ($\lambda_z = 1$), the constant q is set as

$$q = 2(a + 2b + c). \tag{2.48}$$

This provides also that $f = 0$ when $\lambda = \lambda_z = 1$ (see equation (2.21)). Accordingly, relation (2.47) becomes

$$\lambda = \sqrt{\frac{-(a + b\lambda_z^2) + \sqrt{(a + b\lambda_z^2)^2 + 4(a + 2b + c)(b + c\lambda_z^2)}}{2(b + c\lambda_z^2)}}. \tag{2.49}$$

Through (2.48) and dividing by the scalar a, equations (2.45) and (2.46) are rewritten in dimensionless form

$$\overline{\omega} = \frac{\omega}{a} = 2\lambda^2 + \lambda_z^2 - 3 + \left(\lambda^4 + 2\lambda^2\lambda_z^2 - 3\right)\bar{b} + \left(\mu^2 - 1\right)\bar{c} - 2(1 + 2\bar{b} + \bar{c}) \ln \mu, \tag{2.50}$$

$$\overline{\omega}_{,1} = 1, \qquad \overline{\omega}_{,2} = \bar{b}, \qquad \overline{\omega}_{,3} = \bar{c} - \frac{1 + 2\bar{b} + \bar{c}}{\mu^2}, \tag{2.51}$$

where $\bar{b} = b/a$ and $\bar{c} = c/a$. The relation between longitudinal and transversal stretch given by (2.49) takes the form

$$\lambda = \sqrt{\frac{-\left(1 + \bar{b}\lambda_z^2\right) + \sqrt{\left(1 + \bar{b}\lambda_z^2\right)^2 + 4\left(1 + 2\bar{b} + \bar{c}\right)\left(\bar{b} + \bar{c}\lambda_z^2\right)}}{2\left(\bar{b} + \bar{c}\lambda_z^2\right)}}. \tag{2.52}$$

[3] This position does not affect the equilibrium solutions and it is often employed in literature [51–55].

In the following applications, both bars are composed of a Mooney-Rivlin material, therefore both the stored energy functions ω_γ, $\gamma=\alpha,\beta$, are expressed by (2.43). By substituting equations (2.51) and (2.52) into (2.32), the following global equilibrium equations of the von Mises truss for the case of a compressible Mooney-Rivlin material are derived:

$$\begin{aligned}&\hat{p}_\eta+\frac{2th}{L}\left[Q_\alpha\left(B+\bar{u}\right)-Q_\beta\left(B-\bar{u}\right)\right]=0,\\&\hat{p}_\zeta+\frac{2th}{L}\left(Q_\alpha+Q_\beta\right)\left(H+\bar{v}\right)=0,\end{aligned}\tag{2.53}$$

where

$$Q_\gamma=\frac{\left(\bar{b}^2-\bar{c}+P_\gamma\right)\left[2\bar{b}\left(\lambda_z^\gamma\right)^2+\left(\lambda_z^\gamma\right)^4\left(\bar{c}-P_\gamma\right)+1\right]}{\left[\left(\lambda_z^\gamma\right)^2\left(\bar{c}-P_\gamma\right)+\bar{b}\right]^2},$$

$$P_\gamma=\frac{4(2\bar{b}+\bar{c}+1)\left[\bar{c}\left(\lambda_z^\gamma\right)^2+\bar{b}\right]^2}{\left(\lambda_z^\gamma\right)^2\left\{-\sqrt{4(2\bar{b}+\bar{c}+1)\left[\bar{c}\left(\lambda_z^\gamma\right)^2+\bar{b}\right]+\left[\bar{b}\left(\lambda_z^\gamma\right)^2+1\right]^2}+\bar{b}\left(\lambda_z^\gamma\right)^2+1\right\}^2},$$

with $\gamma=\alpha,\beta$ and $\hat{p}_\eta=p_\eta/a$, $\hat{p}_\zeta=p_\zeta/a$.

Hereinafter, a numerical application is performed assuming the following geometrical parameters for the von Mises truss:

$$B=H=10\text{ cm},\qquad t=h=1\text{ cm}.$$

In addition, the values of the constitutive parameters $\bar{c}$ and $\bar{b}$ must be chosen. The more $\bar{c}$ is high the more the constitutive model involves less volume variations, until the limit situation $\bar{c}\to\infty$, which represents the condition of internal incompressibility ($\det\mathbf{F}_\gamma=1$). For this application, the values $\bar{c}=5$ and $\bar{b}=1$ are considered, which are common values adopted in literature [56]. The corresponding constitutive relation between longitudinal stretch and dimensionless external surface traction $\hat{f}=f/a$ is shown in Fig. 2.3. Although variations of $\bar{b}$ and $\bar{c}$ lead to quantitatively different results, the qualitative aspects regarding the behavior of the system remain unchanged.

It is convenient to define the dimensionless displacement components as

$$\hat{u}=\frac{\bar{u}}{B},\qquad\hat{v}=\frac{\bar{v}}{H}.$$

The dimensionless elastic stored energy function of the truss is then defined as

$$\overline{\omega}=\frac{\omega}{a}=\sum_\gamma\overline{\omega}_\gamma,\quad\gamma=\alpha,\beta.$$

and the dimensionless total potential energy density is expressed by

$$\overline{\pi}=\frac{1}{V}\frac{\Pi}{a}=\sum_\gamma\overline{\omega}_\gamma-\frac{\hat{p}_\zeta}{bhL}\bar{v},\quad\gamma=\alpha,\beta.$$

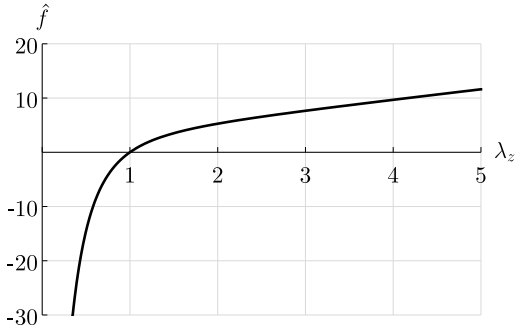

Figure 2.3: Constitutive law of the bar composed of Mooney-Rivlin material with $\bar{b} = 1$, $\bar{c} = 5$. The graph shows normalized traction $\hat{f} = f/a$ vs. longitudinal stretch λ_z

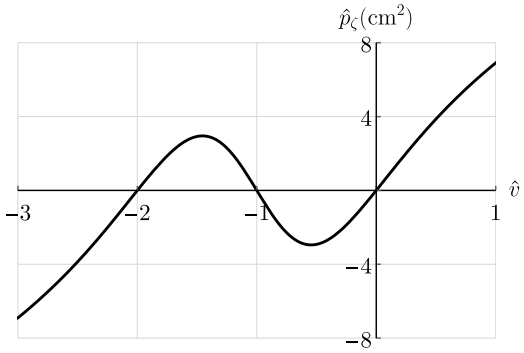

Figure 2.4: Primary branch of equilibrium of the von Mises truss subjected to a vertical load for the case of Mooney-Rivlin material ($\hat{v} = \bar{v}/H$ and $\hat{p}_\zeta = p_\zeta/a$)

2.5.1 Vertical load

The case of vertical load ($p_\eta = 0$) is here analyzed. Fig. 2.4 shows the primary branch of equilibrium, which is obtained by solving the equilibrium equations (2.53) with $\bar{u} = 0$, while Fig. 2.5 shows the complete equilibrium paths. The stability of the equilibrium solutions is assessed by specializing the derivatives of the total potential energy (2.41) for a compressible Mooney-Rivlin material. Subsequently, the sign of the eigenvalues of the characteristic equation (2.42) is analyzed.

As already pointed out, the stability of the equilibrium solutions is not influenced by the load potential energy. Thus, the first considerations about the stability of the primary branch of equilibrium can be done looking at Fig. 2.6, which shows the dimensionless elastic stored energy density $\overline{\omega}$ along the vertical direction ($\bar{u} = 0$). It can be observed that $\overline{\omega}$ presents a concave middle region and two lateral convex regions. The convex parts represent areas where the equilibrium is stable, while in the middle area it is unstable.

Fig. 2.7 shows the second derivative of $\overline{\omega}$ along the vertical direction. It can be observed that there is a middle region of the primary branch where $\partial^2\overline{\omega}/\partial\hat{v}^2$ assumes negative values, which means that the equilibrium is unstable. In particular, that

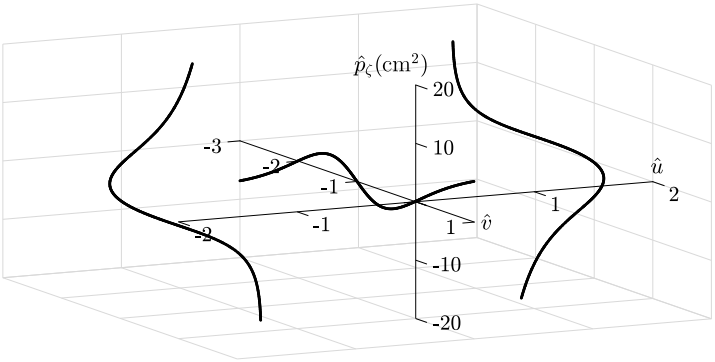

(a) Three-dimensional view ($\hat{u} = \bar{u}/B$, $\hat{v} = \bar{v}/H$ and $\hat{p}_\zeta = p_\zeta/a$)

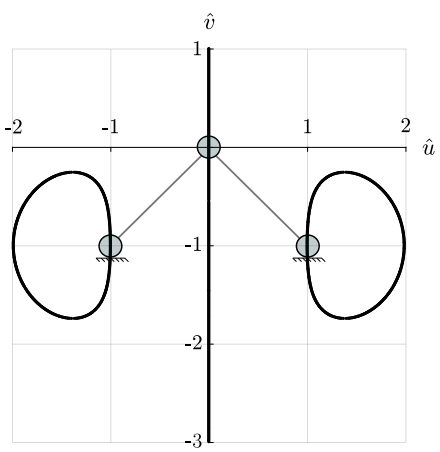

(b) Top view

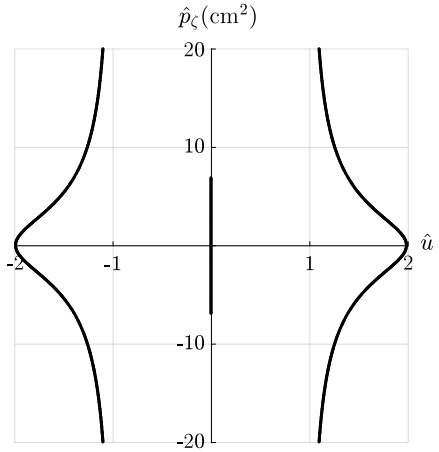

(c) Lateral view

Figure 2.5: Equilibrium paths of the von Mises truss subjected to a vertical load for the case of Mooney-Rivlin material

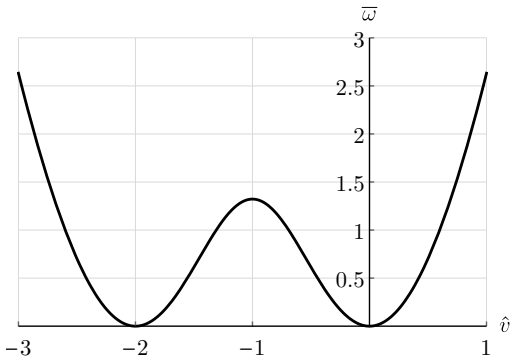

Figure 2.6: Dimensionless elastic stored energy function

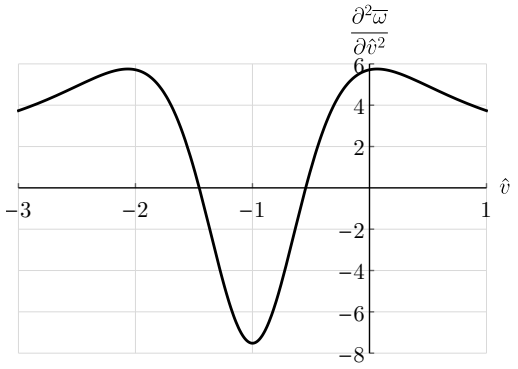

Figure 2.7: Second derivative of the dimensionless elastic stored energy function

region is identified by $\hat{v}_2 = -1.455 < \hat{v} < -0.545 = \hat{v}_1$. The values of the critical loads corresponding to the configurations $\hat{v}_1$ and $\hat{v}_2$, where the equilibrium of the system loses its stability, are $\hat{p}_{\zeta_1} = -2.952$ cm^2 and $\hat{p}_{\zeta_2} = 2.952$ cm^2, respectively. Note also that $\partial^2\overline{\omega}/\partial\hat{v}^2$ assumes positive values everywhere, except for that particular range. Thus, we can conclude that the primary branch of equilibrium is always stable apart from that middle region.

At this point, the behavior of the system inside the range $\hat{v}_2 < \hat{v} < \hat{v}_1$ has to be investigated. In other words, we must understand if stable solutions can be found only along the vertical direction or if other solutions, among the equilibrium paths shown in Fig. 2.5, are also stable. With this aim, the characteristic equation (2.42) is solved numerically, obtaining the eingevalues τ_1 and τ_2.

Fig. 2.8 shows the values assumed by the eigenvalues along the equilibrium paths of Fig. 2.5. We observe that, along the vertical direction ($\bar{u} = 0$), both eigenvalues are always strictly positive except for a middle range that is the unstable region, where τ_1 assumes negative values. Note that this region corresponds to that where $\partial^2\overline{\omega}/\partial\hat{v}^2$ is negative, namely $\hat{v}_2 < \hat{v} < \hat{v}_1$. This confirms that, within this range, the Hessian matrix is indefinite. Hence, this portion of the primary branch of equilibrium is unstable. Fig. 2.8 shows also that, along the other two symmetric branches of the equilibrium paths, τ_1 is always negative and τ_2 is always positive. Therefore, the equilibrium solutions along these two branches are unstable, which means that they can not be observed in laboratory tests.

The combination of the results of equilibrium and stability analyses are shown in Figs. 2.9 and 2.10. We can conclude that, for $\hat{v}$ positive, the equilibrium is always stable and the load $\hat{p}_\zeta$ follows the primary branch of equilibrium shown in Fig. 2.4. Instead, for $\hat{v}$ negative, when the system reaches the configuration $\hat{v}_1$ (that corresponds to the first critical load $\hat{p}_{\zeta_1}$) the loss of stability occurs by the snap-through phenomenon. Thus, in that configuration, a small perturbation produces a jump of the apex node from position $\hat{v}_1$ to position $\hat{v}_2$.

The two critical points $(0, \hat{v}_1, \hat{p}_{\zeta_1})$ and $(0, \hat{v}_2, \hat{p}_{\zeta_2})$ are listed in Tab. 2.1. It is worth mentioning that both critical points 1 and 2 are limit points, which means that they represent the stationary points for the external load. This implies that the instability occurs as buckling, which in the case of the von Mises truss is the so

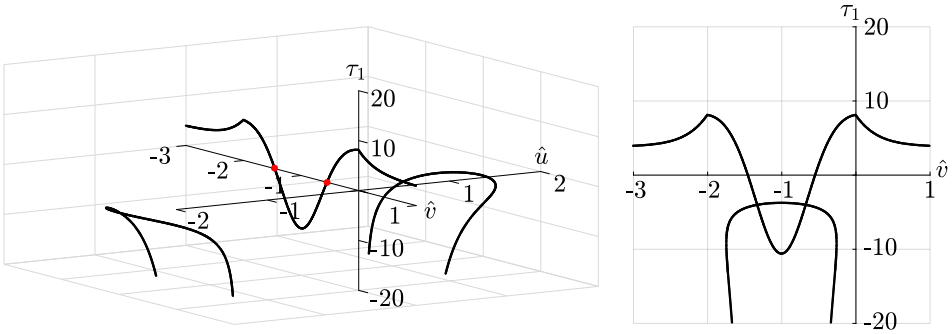

(a) Three-dimensional and lateral views of the first eigenvalue

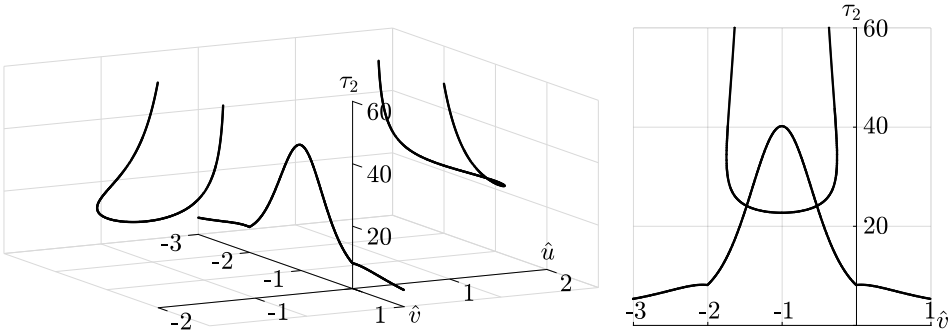

(b) Three-dimensional and lateral views of the second eigenvalue

Figure 2.8: Eigenvalues of the Hessian matrix of the total potential energy for the vertical load case

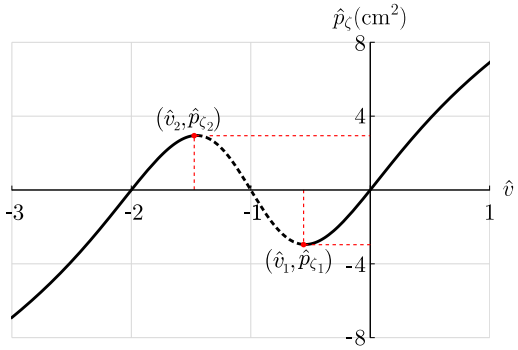

Figure 2.9: Primary branch of equilibrium for the case of vertical load and Mooney-Rivlin material (stable solutions: *continuous lines*, unstable solutions: *dashed lines*)

Table 2.1: Critical points for the von Mises truss subjected to a vertical load in case of Mooney-Rivlin material

Critical point	$\hat{u}$	$\hat{v}$	$\hat{p}_\zeta(\mathrm{cm}^2)$
1	0	-0.545	-2.952
2	0	-1.455	2.952

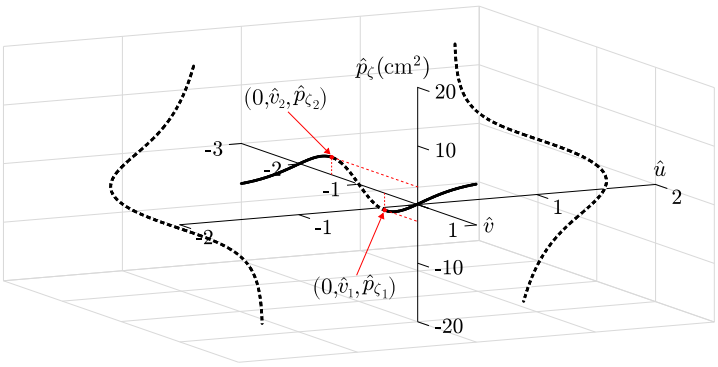

(a) Three-dimensional view

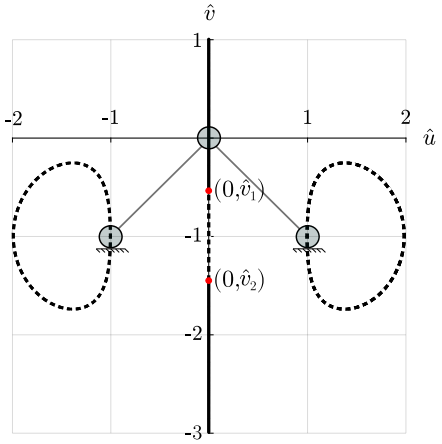

(b) Top view

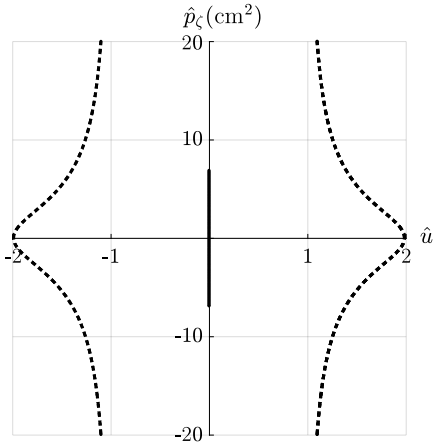

(c) Lateral view

Figure 2.10: Equilibrium paths of the von Mises truss subjected to a vertical load for the case of Mooney-Rivlin material (stable solutions: *continuous lines*, unstable solutions: *dashed lines*)

Table 2.2: Critical points for the von Mises truss subjected to a horizontal load in case of Mooney-Rivlin material

Critical point	$\hat{u}$	$\hat{v}$	$\hat{p}_\eta(\mathrm{cm}^2)$
1	1.958	-0.289	3.737
2	2.193	-1	3.733
3	1.958	-1.711	3.737

called snap-through.

The application to Mooney-Rivlin materials revealed that in case of vertical load the only actual instability is the snap-through, while secondary asymmetric branches are unstable. However, more complex stored energy functions may lead to qualitatively different unstable phenomena. In such circumstance, stable solutions after bifurcation may be observed.

2.5.2 Horizontal load

The case of horizontal load ($p_\zeta = 0$) is now analyzed. The equilibrium paths are obtained as solution of the equilibrium equations (2.53) and the stability analysis is carried out in the same way as the previous application. Namely, the eigenvalues are evaluated along the equilibrium configurations and their sign is investigated.

For the sake of brevity and clarity, the plots of the eigenvalues are not given. Altogether, the solution of equilibrium and stability analyses provides the equilibrium paths of Fig. 2.11. The critical points 1, 2 and 3 are listed in Tab. 2.2.

When a horizontal load is applied, central node C moves along the first branch of equilibrium, which has a shape of an ellipse that has been pinched along the semi-minor axis. The first critical point $(\hat{u}_1, \hat{v}_1, \hat{p}_{\eta_1})$ presents itself as a limit point. In fact, load $\hat{p}_\eta$ is maximum and, in this configuration, buckling takes place. The system jumps to the second critical point $(\hat{u}_2, \hat{v}_2, \hat{p}_{\eta_2})$, which is a bifurcation point. From here, the equilibrium is again stable and node C follows a second branch of equilibrium, characterized by $\hat{v} = -1$.

The equilibrium paths are symmetric with respect to both η and ζ axes. Therefore, critical point $(\hat{u}_1, \hat{v}_3, \hat{p}_{\eta_3})$ takes place in a symmetric configuration with respect to point $(\hat{u}_1, \hat{v}_1, \hat{p}_{\eta_1})$. It is also interesting to observe that along the second branch of equilibrium there are two asymptotes, namely axes $\hat{u} = 1$ and $\hat{u} = -1$ (Fig. 2.12). Specifically, these configurations are the ones where, hypothetically, one bar of the truss degenerates to a point. Note also that the second branch passes through point (0,-1,0) and is always unstable, except from the external regions characterized by $\hat{u} < -\hat{u}_2$ and $\hat{u} > \hat{u}_2$.

The problem of the von Mises truss subjected to a horizontal load was already analyzed by Pecknold et al. [4] by assuming a linear constitutive law for the bars. In this case, the primary path was an ellipse and the secondary path was a cubic curve. Comparisons with such results will be presented in the following.

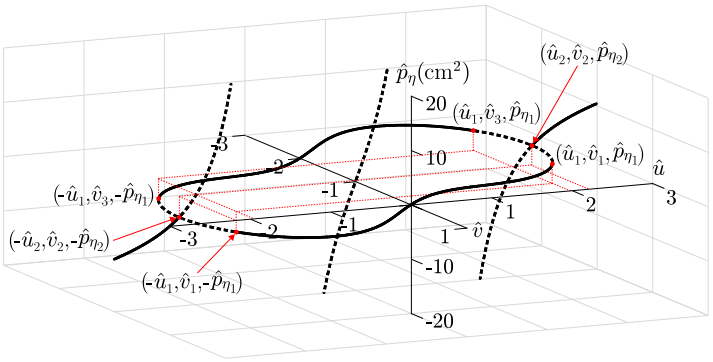

(a) Three-dimensional view ($\hat{u} = \bar{u}/B$, $\hat{v} = \bar{v}/H$ and $\hat{p}_\eta = p_\eta/a$)

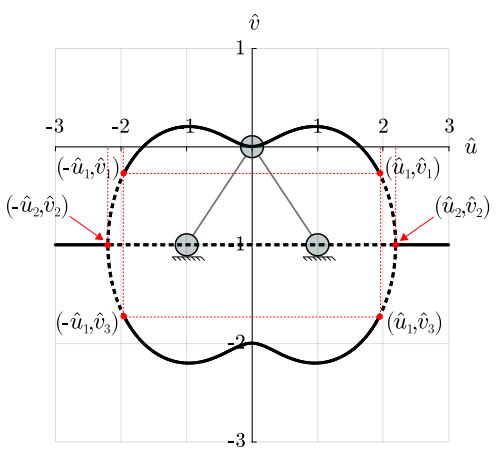

(b) Top view

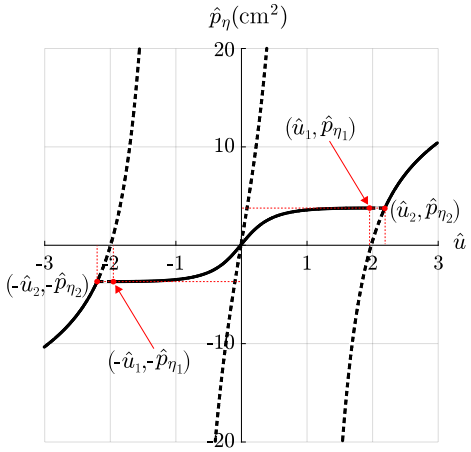

(c) Lateral view

Figure 2.11: Equilibrium paths of the von Mises truss subjected to a horizontal load for the case of Mooney-Rivlin material (stable solutions: *continuous lines*, unstable solutions: *dashed lines*)

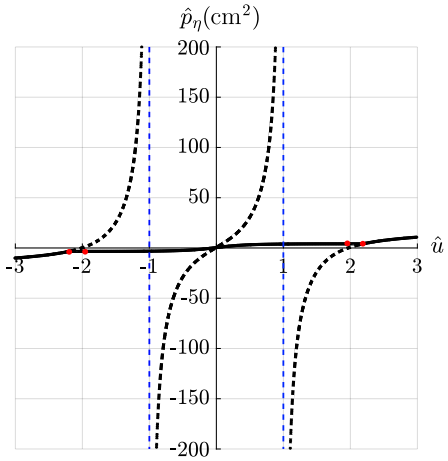

Figure 2.12: Large scale view of load p_η along $\hat{u}$, which shows the asymptotes $\hat{u} = \pm 1$

2.6 Comparison with other models

The theories proposed by Kwasniewski [1] and Pecknold [4] are based on the assumption of linear constitutive law. It is thus interesting to show a comparison between the equilibrium solutions of the present work, which are based on a Mooney-Rivlin law, and the ones obtained by using those theories. It is stressed that their solutions are derived by assuming large nodal displacements and relatively small deformations, which is inconsistent in the context of finite elasticity. Furthermore, a linearly elastic constitutive law is not appropriate for the response of bodies subjected to large deformations.

The formulation provided by the aforementioned authors will be briefly outlined and applied to the case analyzed in Section 2.5. Consequently, a comparison with the results of the fully nonlinear theory presented in this work will be provided.

The Green-Lagrange measure for the axial components of strain adopted in [1,4] is defined as

$$\epsilon_z^\gamma = \frac{l_\gamma^2 - L^2}{2L^2}, \quad \gamma = \alpha, \beta. \tag{2.54}$$

The axial components of stress are thus given by the linear relationship

$$\sigma_z^\gamma = E\epsilon_z^\gamma, \quad \gamma = \alpha, \beta, \tag{2.55}$$

where E is the Young's modulus. Using (2.54) and (2.55), the axial forces are computed as

$$n_\gamma = \sigma_z^\gamma A = bhE\frac{l_\gamma^2 - L^2}{2L^2}, \quad \gamma = \alpha, \beta, \tag{2.56}$$

from which we can define a normalized axial stress $\hat{\sigma}_z^\gamma = \dfrac{\sigma_z^\gamma}{a}$. The red curve of Fig. 2.13 shows normalized axial stress $\hat{\sigma}_z^\gamma$ vs. longitudinal stretch, which represents the constitutive behavior of the bars of the truss. The black curve of Fig. 2.13 represents instead the constitutive behavior of the Mooney-Rivlin material, which was employed in the applications of Section 2.5.

Equation (2.56) expresses a linear relation between σ_z^γ and ϵ_z^γ (Green-Lagrange strain measure). However, in Fig. 2.13, σ_z^γ is plotted as a function of the longitudinal stretch λ_z^γ. This explains the nonlinearity of the red curve. Note also that the two curves correspond only for small axial deformations ($\lambda_z^\gamma \approx 1$). For large contractions ($\lambda_z^\gamma < 1$), the linear constitutive law (red curve) exhibits softening, which is not consistent with the behavior of real materials. The condition of $\lambda_z^\gamma = 0$, for which the bar degenerates into a point, is reached with a finite and relatively low value of axial stress. This is also not representative for the behavior of real bodies subjected to axial contractions. From Fig. 2.13 we also note that, for large elongations ($\lambda_z^\gamma > 1$), the red curve shows a monotonic hardening, which is usually not observed in common materials.

The formulation provided in [1] is retrieved by substituting (2.56) into (2.3),

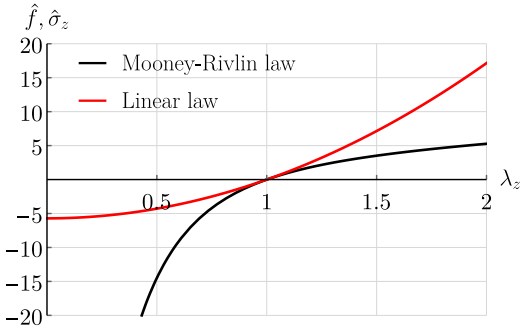

Figure 2.13: Dimensionless traction $\hat{\sigma}_z = \sigma_z/a$ vs. longitudinal stretch of the bar in the formulation of Kwasniewski [1] (*red curve*) and comparison with the Mooney-Rivlin case (*black curve*). Note that σ_z is a linear function of the Green-Lagrange strain ϵ_z, but here it is plotted in function of the longitudinal stretch λ_z^γ. This is why the red curve is nonlinear

from which the following equilibrium equations are derived:

$$\begin{aligned} p_\eta \frac{2L^2}{bhE} - c_\alpha(l_\alpha^2 - L^2) + c_\beta(l_\beta^2 - L^2) = 0, \\ p_\zeta \frac{2L^2}{bhE} - s_\alpha(l_\alpha^2 - L^2) - s_\beta(l_\beta^2 - L^2) = 0. \end{aligned} \tag{2.57}$$

An application will be presented in the following. The geometry of the truss is the one reported in Section 2.5. In order to compare the results, the value of the elastic constant E is computed by introducing $\bar{c} = 5$ and $\bar{b} = 1$ into (2.74), which represents a correlation between the constitutive parameters of the Mooney-Rivlin material and the Young's modulus E. Note that relation (2.74) is derived through a linearization of the nonlinear theory. Thus, it establishes a correspondence between the Mooney-Rivlin constitutive law and the linear elastic law that holds for small displacements and displacement gradients. It goes without saying that, for large deformations, the two constitutive behaviors are different.

2.6.1 Vertical load

The solution of the equilibrium equations (2.57) is represented in Fig. 2.14. Differently from the case of Mooney-Rivlin constitutive law, no other solutions are found except from the primary branch of equilibrium. For this reason, Fig. 2.14 shows only the $\hat{p}_\zeta = p_\zeta/a$ vs. $\hat{v}$ plot. In the same figure, we can observe the comparison with the primary branch obtained with the nonlinear formulation presented in this paper (equation (2.53)).

As expected, for low values of vertical displacement the curves are consistent. As the magnitude of displacement increases, the discrepancy between results rises. This is a consequence of the use of a different strain measure and a different constitutive law. The present fully nonlinear theory provides an exact description of the kinematics of the system, while the linear constitutive behavior is appropriate only for small deformations.

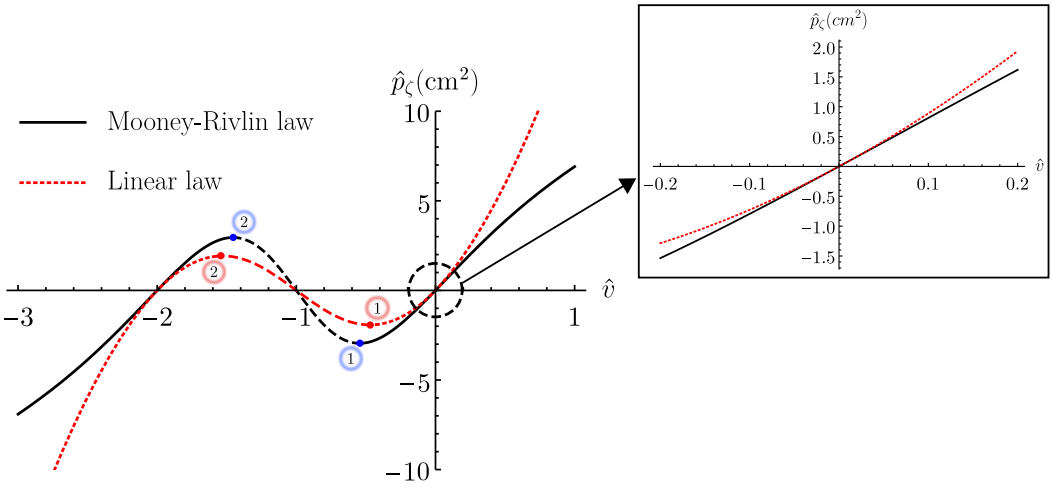

Figure 2.14: Comparison between the primary branch of equilibrium provided by the present theory (*Mooney-Rivlin law*) and the one provided by the formulation of Kwasniewski [1] (*Linear law*) for the von Mises truss subjected to a vertical load

Table 2.3: Critical points for the von Mises truss subjected to a vertical load in case of linear elastic constitutive law (Kwasniewski [1])

Critical point	$\hat{u}$	$\hat{v}$	$\hat{p}_\zeta(\mathrm{cm}^2)$
1	0	-0.423	-1.905
2	0	-1.577	1.905

The critical configurations and critical loads of the fully nonlinear theory are reported in Tab. 2.1. Instead, the unstable region in case of linear constitutive law is identified by the critical points given in Tab. 2.3. Since snap-through takes place when the axial deformation of the bars is relatively large, there is a sensible gap between the critical configurations of the two simulations (Mooney-Rivlin law and linear law). In particular, the relative errors committed on $\hat{v}_1$ and $\hat{v}_2$ are, respectively, 8.42% and 22.47%. The relative error committed on critical loads $\hat{p}_{\zeta_1}$ and $\hat{p}_{\zeta_2}$ is 35.48%.

We remark that the relative errors committed are highly influenced by the geometry of the truss. If the inclination of the truss is very low, the resulting deformations of the bars would be relatively small and the discrepancy between the results of the models would not be so evident. However, in a general case, it is not true that the deformations are small enough to assume a linear constitutive law. Therefore, for an accurate analysis of equilibrium and stability of truss structures, it is recommended that a fully nonlinear model is employed.

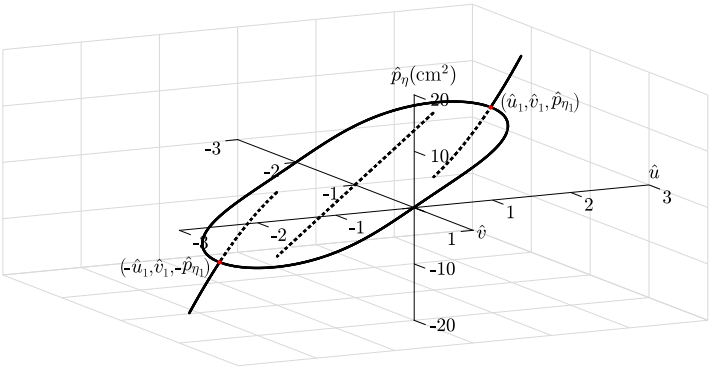

(a) Three-dimensional view ($\hat{u} = \bar{u}/B$, $\hat{v} = \bar{v}/H$ and $\hat{p}_\eta = p_\eta/a$)

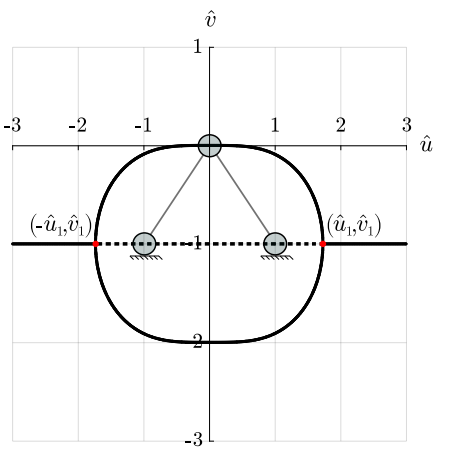

(b) Top view

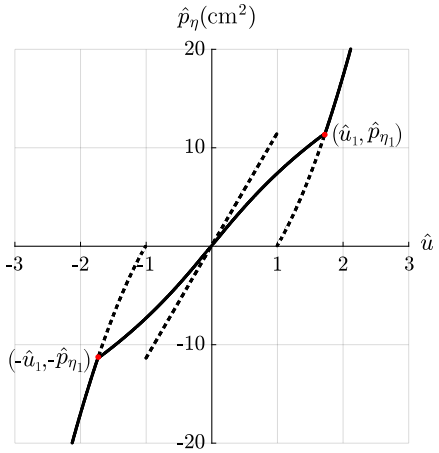

(c) Lateral view

Figure 2.15: Equilibrium paths of the von Mises truss subjected to a horizontal load for the case of linear elastic material [1] (stable solutions: *continuous lines*, unstable solutions: *dashed lines*)

2.6.2 Horizontal load

The equilibrium equations (2.57) are now solved for the horizontal load case. Again, for the sake of brevity and clarity, the plots of the eigenvalues are not given. Altogether, the solution of equilibrium and stability analyses provides the equilibrium paths of Fig. 2.15.

We notice that there are a number of differences with respect to the fully nonlinear simulation given in Fig. 2.11. Firstly, the projection of the first equilibrium path on the $\hat{u}$-$\hat{v}$ plane has the shape of an ellipse, without showing pinching along the semi-minor axis. This is due to the linear constitutive behavior of the bars. Secondly, there are two discontinuities along the secondary branch of equilibrium (which is characterized by $\hat{v} = -1$). The discontinuities take place in the configurations $\hat{u} = \pm 1$, $\hat{v} = -1$. This happens because, in the model proposed in [1, 4], the strain measure adopted is such that the condition of $\lambda_z^\gamma = 0$ (degeneration of

Table 2.4: Critical points for the von Mises truss subjected to a horizontal load in case of linear elastic constitutive law (Kwasniewski [1])

Critical point	$\hat{u}$	$\hat{v}$	$\hat{p}_\eta(\mathrm{cm}^2)$
1	-1.731	-1	-11.417
2	1.731	-1	11.417

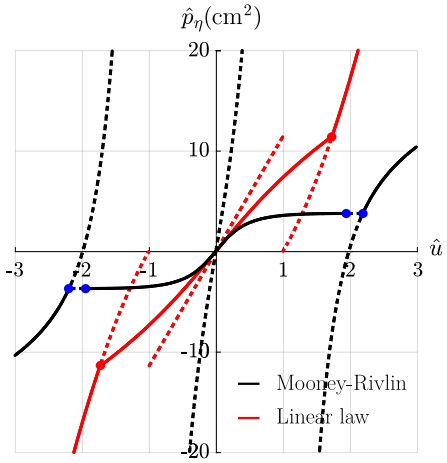

Figure 2.16: Comparison between the solutions provided by the present theory (*Mooney-Rivlin law*) and the formulation of Kwasniewski [1] (*Linear law*) for the von Mises truss subjected to a horizontal load

the bar into a point) is reached with a finite value of axial stress, as shown in Fig. 2.13. Thus, along $\hat{v} = -1$ and inside the region $\hat{u} = \pm 1$, the secondary branch is continuous. When configurations $\hat{u} = \pm 1$, $\hat{v} = -1$ are reached, the axial force acting on the bar in compression changes its sign, causing a jump in the equilibrium path.

The stability of the equilibrium solutions provides two critical points along the secondary branch of equilibrium, given in Tab. 2.4. The two critical configurations take place as bifurcation points, whereas buckling phenomena are not observed. The scenario of solutions is thus less complex than the one derived from the solution of the fully nonlinear formulation (Fig. 2.11). In that case, an interaction between snap-through (buckling) and bifurcation was observed.

Fig. 2.16 shows a comparison of load $\hat{p}_\eta$ along direction $\hat{u}$. As expected, the two curves agree only for small deformations, namely when $\hat{u}$ is close to zero. As the deformation increases, the fully nonlinear model shows a behavior that is less stiff than the linear one. This because the Mooney-Rivlin material displays softening when subjected to tension, reducing thus its stiffness. Instead, the linear elastic behavior responds with its initial stiffness (Young's modulus) regardless of the deformation that the bar is experiencing.

In conclusion, the hypothesis of linear constitutive law leads to solutions that are both quantitatively and qualitatively different. The linear behavior of the material

and the strain measure adopted lead to inconsistencies, such as discontinuity in the equilibrium path.

2.7 Linearization of the fully nonlinear theory

The linearized theory is derived from the finite theory by introducing the hypothesis that both displacements and displacement gradients are small.

The longitudinal stretches (2.2) are developed in Taylor series as functions of $\bar{u}$ and $\bar{v}$. Truncating these series at the first order, the following expressions are obtained:

$$\begin{aligned} \lambda_z^{\alpha} &\cong 1 + \frac{B\bar{u} + H\bar{v}}{L^2} + o(\bar{u}) + o(\bar{v}), \\ \lambda_z^{\beta} &\cong 1 - \frac{B\bar{u} - H\bar{v}}{L^2} + o(\bar{u}) + o(\bar{v}). \end{aligned} \tag{2.58}$$

Introducing (2.58) into the constitutive relation between longitudinal and transversal stretch for the case of a Mooney-Rivlin material (2.52), the approximated expressions for the transversal stretches become

$$\begin{aligned} \lambda_{\alpha} &\cong 1 - \frac{(B\bar{u} + H\bar{v})(\bar{b} + \bar{c})}{L^2(1 + 3\bar{b} + 2\bar{c})} + o(\bar{u}) + o(\bar{v}), \\ \lambda_{\beta} &\cong 1 + \frac{(B\bar{u} - H\bar{v})(\bar{b} + \bar{c})}{L^2(1 + 3\bar{b} + 2\bar{c})} + o(\bar{u}) + o(\bar{v}). \end{aligned} \tag{2.59}$$

The rigid rotations of the bodies are described by the angles ψ_γ, $\gamma = \alpha, \beta$. Using the geometrical relations (2.4), the following expressions for the rigid rotations ψ_α and ψ_β hold:

$$\begin{aligned} \psi_{\alpha} &= \theta_0 - \theta_{\alpha} = \arccos\left(\frac{B}{L}\right) - \arccos\left(\frac{B + \bar{u}}{\sqrt{(B + \bar{u})^2 + (H + \bar{v})^2}}\right), \\ \psi_{\beta} &= \theta_{\beta} - \theta_0 = \arccos\left(\frac{B - \bar{u}}{\sqrt{(B - \bar{u})^2 + (H + \bar{v})^2}}\right) - \arccos\left(\frac{B}{L}\right). \end{aligned} \tag{2.60}$$

Developing (2.60) in Taylor series and truncating them at the first order, the linearized rigid rotations assume the form

$$\begin{aligned} \psi_{\alpha} &\cong \frac{H\bar{u} - B\bar{v}}{L^2} + o(\bar{u}) + o(\bar{v}), \\ \psi_{\beta} &\cong \frac{H\bar{u} + B\bar{v}}{L^2} + o(\bar{u}) + o(\bar{v}). \end{aligned} \tag{2.61}$$

At this point, substituting (2.58), (2.59) and (2.61) into (2.7), the linearized dis-

placement fields are derived

$$\begin{cases} u_\alpha \cong Z\dfrac{H\bar{u}-B\bar{v}}{L^2} - X\dfrac{(B\bar{u}+H\bar{v})\,(\bar{b}+\bar{c})}{L^2(1+3\bar{b}+2\bar{c})} + o(\bar{u}) + o(\bar{v}) \\ v_\alpha \cong -Y\dfrac{(B\bar{u}+H\bar{v})\,(\bar{b}+\bar{c})}{L^2(1+3\bar{b}+2\bar{c})} + o(\bar{u}) + o(\bar{v}) \\ w_\alpha \cong X\dfrac{B\bar{v}-H\bar{u}}{L^2} + Z\dfrac{B\bar{u}+H\bar{v}}{L^2} + o(\bar{u}) + o(\bar{v}), \end{cases} \tag{2.62}$$

$$\begin{cases} u_\beta \cong Z\dfrac{H\bar{u}+B\bar{v}}{L^2} + X\dfrac{(B\bar{u}-H\bar{v})\,(\bar{b}+\bar{c})}{L^2(1+3\bar{b}+2\bar{c})} + o(\bar{u}) + o(\bar{v}) \\ v_\beta \cong Y\dfrac{(B\bar{u}-H\bar{v})\,(\bar{b}+\bar{c})}{L^2(1+3\bar{b}+2\bar{c})} + o(\bar{u}) + o(\bar{v}) \\ w_\beta \cong -X\dfrac{H\bar{u}+B\bar{v}}{L^2} - Z\dfrac{B\bar{u}-H\bar{v}}{L^2} + o(\bar{u}) + o(\bar{v}). \end{cases}$$

The material gradients of (2.62) are

$$[\mathbf{H}_\alpha] = \begin{bmatrix} -\dfrac{(B\bar{u}+H\bar{v})\,(\bar{b}+\bar{c})}{L^2(1+3\bar{b}+2\bar{c})} & 0 & \dfrac{H\bar{u}-B\bar{v}}{L^2} \\ 0 & -\dfrac{(B\bar{u}+H\bar{v})\,(\bar{b}+\bar{c})}{L^2(1+3\bar{b}+2\bar{c})} & 0 \\ -\dfrac{H\bar{u}-B\bar{v}}{L^2} & 0 & \dfrac{B\bar{u}+H\bar{v}}{L^2} \end{bmatrix},$$

$$[\mathbf{H}_\beta] = \begin{bmatrix} \dfrac{(B\bar{u}-H\bar{v})\,(\bar{b}+\bar{c})}{L^2(1+3\bar{b}+2\bar{c})} & 0 & \dfrac{H\bar{u}+B\bar{v}}{L^2} \\ 0 & \dfrac{(B\bar{u}-H\bar{v})\,(\bar{b}+\bar{c})}{L^2(1+3\bar{b}+2\bar{c})} & 0 \\ -\dfrac{H\bar{u}+B\bar{v}}{L^2} & 0 & -\dfrac{B\bar{u}-H\bar{v}}{L^2} \end{bmatrix}. \tag{2.63}$$

The application of the theorem of additive decomposition to the displacement gradients (2.63) allows to compute the symmetric tensors of infinitesimal strain and the skew-symmetric tensors of infinitesimal rigid rotation

$$[\mathbf{E}_\gamma] = \left[\frac{1}{2}\left(\mathbf{H}_\gamma + \mathbf{H}_\gamma^T\right)\right] = \begin{bmatrix} \epsilon_x^\gamma & \dfrac{1}{2}\gamma_{xy}^\gamma & \dfrac{1}{2}\gamma_{xz}^\gamma \\ \dfrac{1}{2}\gamma_{xy}^\gamma & \epsilon_y^\gamma & \dfrac{1}{2}\gamma_{yz}^\gamma \\ \dfrac{1}{2}\gamma_{xz}^\gamma & \dfrac{1}{2}\gamma_{yz}^\gamma & \epsilon_z^\gamma \end{bmatrix},$$

$$[\mathbf{W}_\gamma] = \left[\frac{1}{2}\left(\mathbf{H}_\gamma - \mathbf{H}_\gamma^T\right)\right] = \begin{bmatrix} 0 & -\omega_z^\gamma & \omega_y^\gamma \\ \omega_z^\gamma & 0 & -\omega_x^\gamma \\ -\omega_y^\gamma & \omega_x^\gamma & 0 \end{bmatrix}, \quad \gamma = \alpha, \beta,$$

where

$$\begin{aligned}
&\epsilon_z^\alpha = \frac{B\bar{u}+H\bar{v}}{L^2}, \qquad \epsilon_z^\beta = -\frac{B\bar{u}-H\bar{v}}{L^2},\\
&\epsilon_x^\alpha = \epsilon_y^\alpha = -\frac{\bar{b}+\bar{c}}{1+3\bar{b}+2\bar{c}}\epsilon_z^\alpha, \qquad \epsilon_x^\beta = \epsilon_y^\beta = -\frac{\bar{b}+\bar{c}}{1+3\bar{b}+2\bar{c}}\epsilon_z^\beta,\\
&\gamma_{xy}^\alpha = \gamma_{xz}^\alpha = \gamma_{yz}^\alpha = \gamma_{xy}^\beta = \gamma_{xz}^\beta = \gamma_{yz}^\beta = 0, \qquad \omega_x^\alpha = \omega_z^\alpha = \omega_x^\beta = \omega_z^\beta = 0,\\
&\omega_y^\alpha = \frac{H\bar{u}-B\bar{v}}{L^2}, \qquad \omega_y^\beta = \frac{H\bar{u}+B\bar{v}}{L^2}.
\end{aligned} \tag{2.64}$$

Let us focus on the stress components in the linearized theory. Substituting the linearized expressions of the stretches (2.58) and (2.59) into the constitutive relation (2.21) and neglecting the terms of order greater than one in the components $\bar{u}$ and $\bar{v}$, the following approximated forms are computed:

$$\begin{aligned}
\hat{f}_\alpha &\cong \frac{4\,(B\bar{u}+H\bar{v})\,(1+\bar{b})(1+4\bar{b}+3\bar{c})}{L^2(1+3\bar{b}+2\bar{c})} + o(\bar{u}) + o(\bar{v}),\\
\hat{f}_\beta &\cong -\frac{4\,(B\bar{u}-H\bar{v})\,(1+\bar{b})(1+4\bar{b}+3\bar{c})}{L^2(1+3\bar{b}+2\bar{c})} + o(\bar{u}) + o(\bar{v}).
\end{aligned} \tag{2.65}$$

The linearized Piola-Kirchooff stress tensor for the γ-th body becomes

$$[\boldsymbol{T}_{\boldsymbol{R}\gamma}] = \begin{bmatrix} 0 & 0 & f_\gamma \sin\psi_\gamma \\ 0 & 0 & 0 \\ 0 & 0 & f_\gamma \cos\psi_\gamma \end{bmatrix} \cong \begin{bmatrix} 0 & 0 & 0 \\ 0 & 0 & 0 \\ 0 & 0 & f_\gamma \end{bmatrix}, \quad \gamma = \alpha, \beta,$$

where $f_\gamma = \hat{f}_\gamma\, a$ and ψ_γ are given by (2.65) and (2.61), respectively.

The linearization of the Cauchy stress tensor for the γ-th body yields

$$[\boldsymbol{T}_\gamma] = \begin{bmatrix} \dfrac{f_\gamma \sin^2\psi_\gamma}{(\lambda^\gamma)^2} & 0 & \dfrac{f_\gamma \sin\psi_\gamma \cos\psi_\gamma}{(\lambda^\gamma)^2} \\ 0 & 0 & 0 \\ \dfrac{f_\gamma \sin\psi_\gamma \cos\psi_\gamma}{(\lambda^\gamma)^2} & 0 & \dfrac{f_\gamma \cos^2\psi_\gamma}{(\lambda^\gamma)^2} \end{bmatrix} \cong \begin{bmatrix} 0 & 0 & 0 \\ 0 & 0 & 0 \\ 0 & 0 & \dfrac{f_\gamma}{(\lambda^\gamma)^2} \end{bmatrix}, \quad \gamma = \alpha, \beta. \tag{2.66}$$

Using expressions (2.59) and (2.65), the only nonvanishing component of the Cauchy stress tensor become

$$\begin{aligned}
T_{\alpha_3} = \frac{f_\alpha}{(\lambda^\alpha)^2} &\cong \frac{4a\,(B\bar{u}+H\bar{v})\,(1+\bar{b})(1+4\bar{b}+3\bar{c})}{L^2(1+3\bar{b}+2\bar{c})}\left[1 - \frac{(B\bar{u}+H\bar{v})\,(\bar{b}+\bar{c})}{L^2(1+3\bar{b}+2\bar{c})}\right]^{-2}\\
&\cong \frac{4a\,(B\bar{u}+H\bar{v})\,(1+\bar{b})(1+4\bar{b}+3\bar{c})}{L^2(1+3\bar{b}+2\bar{c})} + o(\bar{u}) + o(\bar{v}) = f_\alpha,
\end{aligned} \tag{2.67}$$

$$\begin{aligned}
T_{\beta_3} = \frac{f_\beta}{(\lambda^\beta)^2} &\cong -\frac{4a\,(B\bar{u}-H\bar{v})\,(1+\bar{b})(1+4\bar{b}+3\bar{c})}{L^2(1+3\bar{b}+2\bar{c})}\left[1 + \frac{(B\bar{u}-H\bar{v})\,(\bar{b}+\bar{c})}{L^2(1+3\bar{b}+2\bar{c})}\right]^{-2}\\
&\cong -\frac{4a\,(B\bar{u}-H\bar{v})\,(1+\bar{b})(1+4\bar{b}+3\bar{c})}{L^2(1+3\bar{b}+2\bar{c})} + o(\bar{u}) + o(\bar{v}) = f_\beta.
\end{aligned} \tag{2.68}$$

Therefore, the components of the Piola-Kichhoff and the Cauchy stress tensors match. Indeed, it is common knowledge that in the infinitesimal theory the two stress measures coincide.

The stress components (2.65) are derived using the constitutive law of a Mooney-Rivlin material. Thus, they do not coincide to those of the usual linearized theory, which are referred to an isotropic linear elastic constitutive law. Although, relations for the constitutive parameters $\bar{b}$ and $\bar{c}$ can be provided, in order to replicate the stresses given by the Navier's inverse relationships

$$\bar{\mathbf{T}}_\gamma = 2G\bar{\mathbf{E}}_\gamma + \bar{\lambda}(\operatorname{tr}\bar{\mathbf{E}}_\gamma)\mathbf{I}, \quad \gamma = \alpha, \beta, \tag{2.69}$$

where G and $\bar{\lambda}$ are the Lamé constants and $\operatorname{tr}\bar{\mathbf{E}}_\gamma = \epsilon_x^\gamma + \epsilon_y^\gamma + \epsilon_z^\gamma$. The tensor $\bar{\mathbf{T}}_\gamma$ is diagonal and, from (2.69), its components are

$$\sigma_x^\alpha = \sigma_y^\alpha = \frac{(B\bar{u} + H\bar{v})\left[\bar{\lambda}(1+\bar{b}) - 2G(\bar{b}+\bar{c})\right]}{L^2(1+3\bar{b}+2\bar{c})}, \tag{2.70}$$

$$\sigma_z^\alpha = \frac{(B\bar{u} + H\bar{v})\left[\bar{\lambda}(1+\bar{b}) + 2G(1+3\bar{b}+2\bar{c})\right]}{L^2(1+3\bar{b}+2\bar{c})}, \tag{2.71}$$

$$\sigma_x^\beta = \sigma_y^\beta = \frac{(B\bar{u} - H\bar{v})\left[-\bar{\lambda}(1+\bar{b}) + 2G(\bar{b}+\bar{c})\right]}{L^2(1+3\bar{b}+2\bar{c})}, \tag{2.72}$$

$$\sigma_z^\beta = -\frac{(B\bar{u} - H\bar{v})\left[\bar{\lambda}(1+\bar{b}) + 2G(1+3\bar{b}+2\bar{c})\right]}{L^2(1+3\bar{b}+2\bar{c})}. \tag{2.73}$$

A linear system of two equations is obtained by imposing the equivalence of σ_x^α (or σ_y^α) and σ_z^α, expressed respectively by (2.70) and (2.71), with the corresponding components of the linearized Cauchy stress tensor $\mathbf{T}_\alpha$, given by (2.66) and (2.67). Note that the same linear system can be obtained by the equivalence of the components of $\bar{\mathbf{T}}_\beta$, expressed by (2.72) and (2.73), with the corresponding components of $\mathbf{T}_\beta$, given by (2.66) and (2.68). The solution of this linear system leads to the following relations:

$$\begin{aligned} G &= 2(a+b), \\ \bar{\lambda} &= 4a(b+c). \end{aligned}$$

In the infinitesimal theory, it is common to use the elastic constants E and ν. Thus, the conversion is

$$E = \frac{G(3\bar{\lambda}+2G)}{\bar{\lambda}+G} = \frac{4(a+b)(a+4b+3c)}{a+3b+2c}, \tag{2.74}$$

$$\nu = \frac{\bar{\lambda}}{2(\bar{\lambda}+G)} = \frac{b+c}{a+3b+2c}. \tag{2.75}$$

Note that relations (2.74) and (2.75) correspond to those reported in [54], where the authors analyzed the problem of a Mooney-Rivlin solid subjected to finite bending.

The components of the strain tensor $\mathbf{E}_\gamma$, expressed by (2.64), and the elastic constants E and ν, given by (2.74) and (2.75), are introduced into (2.69), deriving the following expressions for the components of the tensor $\bar{\mathbf{T}}_\gamma$:

$$\sigma_x^\gamma = \sigma_y^\gamma = 0, \qquad \sigma_z^\gamma = E\epsilon_z^\gamma, \quad \gamma = \alpha, \beta. \tag{2.76}$$

In addition, substituting (2.75) into (2.64), the following relation is obtained:

$$\epsilon_x^\gamma = \epsilon_y^\gamma = -\nu\epsilon_z^\gamma, \quad \gamma = \alpha, \beta. \tag{2.77}$$

These results show that, starting from the finite solution for the von Mises truss, the linearization process correctly leads to the well-know solution of the linearized problem.

The expression of the longitudinal strain rate ϵ_z^γ, $\gamma = \alpha, \beta$, is computed performing the equilibrium in undeformed configuration, whose solution is

$$n_\alpha = \frac{L\,(p_\eta H + p_\zeta B)}{2BH}, \qquad n_\beta = \frac{L\,(p_\zeta B - p_\eta H)}{2BH}. \tag{2.78}$$

Substituting (2.78) into the linear constitutive law $\epsilon_z^\gamma = \dfrac{n_\gamma}{EA}$ for beams subjected to uniaxial force, the following expressions are derived:

$$\epsilon_z^\alpha = \frac{L\,(p_\eta H + p_\zeta B)}{2EABH}, \qquad \epsilon_z^\beta = \frac{L\,(p_\zeta B - p_\eta H)}{2EABH}. \tag{2.79}$$

Transversal components of strain and axial components of stress can be finally derived by substituting relations (2.79) into (2.76) and (2.77). This concludes the linearization process of the finite solution for the von Mises truss.

2.8 Further considerations

This chapter presented an analytical formulation of equilibrium and stability of the von Mises truss in finite elasticity for the case of isotropic, homogeneous and hyperelastic material. The formulation was then specialized for a compressible Mooney-Rivlin material and applications for both vertical and horizontal load cases were given.

The theories developed by Ligarò and Valvo [5], Kwasniewski [1] and Pecknold et al. [4] assumed moderately small deformations and a linear constitutive law for the material. The original contribution of the formulation presented in this chapter is that both displacement and deformation fields are considered large. Therefore, the kinematics of the system is exactly described, without having recourse to hypotheses that could be in contrast with the actual behavior of the truss. Moreover, the equilibrium equations are written for a general stored energy function. Thus, this theory can be applied for any homogeneous and isotropic hyperelastic material. For instance, it can be specialized using sophisticated models for compressible rubber-like materials, such as those proposed by Ogden [57] and Gent [58].

In the next chapter, experimental and numerical investigations on the von Mises truss will be presented. This will provide a validation of the theoretical formulation given in the present chapter.

Chapter 3

Experimental and numerical studies of the equilibrium of the von Mises truss

In this chapter, the equilibrium of the von Mises truss subjected to a vertical load is analyzed from both experimental and numerical points of view [59]. The aim is to validate the analytical approach presented in Chapter 2. A rubber material is employed, so that large deformations can be experimentally observed. The materials classically employed in constructions, such as concrete and steel, hardly experience large deformations when subjected to compression. This is the reason why in the literature there is lack of experimental tests involving both large displacements and deformations.

The constitutive parameters of the Mooney-Rivlin law are identified by means of a genetic algorithm that fits experimental data from uniaxial tests on rubber specimens. The numerical analysis is performed through a finite element (FE) model. Differently from the analytical and FE simulations that can be found in the literature, the models presented in this work are entirely developed in three-dimensional finite elasticity.

Experiments are conducted with a device that allows the rubber specimens to undergo large axial deformations. For the first time, snap-through is observed experimentally on rubber materials. The analytic, experimental and numerical equilibrium paths are compared in order to demonstrate the soundness of the methods proposed.

This chapter is organized as follows. Firstly, the analytical formulation introduced in Chapter 2 is adjusted according to the characteristics of the von Mises truss of the experiment. Consequently, the uniaxial tests for rubber characterization and the experimental investigation of the von Mises truss are described. Then, a description of the FE models for the numerical analysis is given and the strategy for fitting the constitutive model to experimental data is outlined. Finally, analytical, experimental and numerical results are presented and discussed, giving also some insights into the effect of Eulerian buckling on the solution.

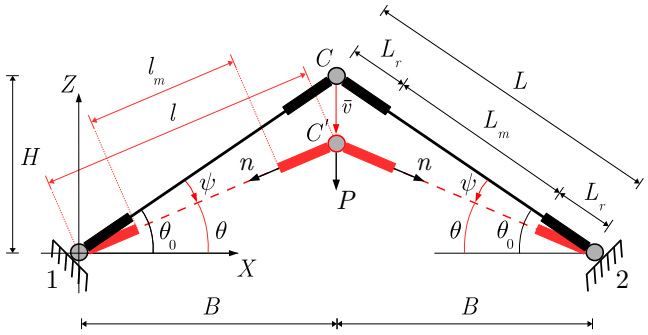

(a) Kinematics of the truss, where the rigid parts represent the space occupied by the undeformable steel hinges of the experimental device (Section 3.2.2)

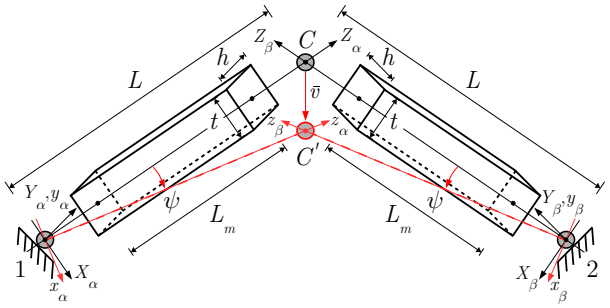

(b) Rubber bodies (rectangular prisms) with corresponding material and principal reference systems

Figure 3.1: The von Mises truss and its configuration in the experiment

3.1 Analytical model

The von Mises truss of Fig. 3.1 consists of two equal rubber bars connected through a hinge at node C. The bars are composed of an inner deformable material, while the terminal parts are rigid elements. The length of the terminal parts is L_r and it represents the space occupied by the hinge in the experimental device, which is presented in Section 3.2.2. The length of the inner deformable part is L_m.

As shown in Fig. 3.1a, the apex node C is loaded by the external dead force P, acting in the Z direction of the global reference system XYZ with origin in node 1. Under the effect of the external load, node C undergoes the vertical displacement $\bar{v}$. Note that, for reasons of convenience, $\bar{v}$ is assumed positive in downward direction (in Chapters 2 it was assumed positive in upward direction). The horizontal degree of freedom of control point C is not considered here. This because the results presented in Section 2.5.1 demonstrated that stable solutions can be found only along the vertical degree of freedom.

The entire length of both bars in reference configuration is $L = \sqrt{B^2 + H^2}$, while in deformed configuration $l = \sqrt{B^2 + (H - \bar{v})^2}$. The length of the deformable part

of the bars in reference configuration is

$$L_m = \sqrt{(B - 2L_r\cos\theta_0)^2 + (H - 2L_r\sin\theta_0)^2},$$

whereas in deformed configuration

$$l_m = \sqrt{(B - 2L_r\cos\theta)^2 + (H - \bar{v} - 2L_r\sin\theta)^2},$$

where

$$\cos\theta_0 = \frac{B}{L}, \qquad \cos\theta = \frac{B}{l}, \qquad \sin\theta_0 = \frac{H}{L}, \qquad \sin\theta = \frac{H-\bar{v}}{l}, \tag{3.1}$$

being θ_0 and θ the inclination angle of the truss in reference and deformed configurations, respectively.

The bars are three-dimensional bodies with a rectangular cross section of width t and height h, as shown in Fig. 3.1b. It is assumed that the material is homogeneous, isotropic and hyperelastic. The deformation of the bodies is assumed to be homogeneous.

The fixed material coordinate systems $X_\gamma Y_\gamma Z_\gamma$ ($\gamma = \alpha, \beta$) are defined. In addition, the coordinate systems $x_\gamma y_\gamma z_\gamma$ are established in deformed configuration. As depicted in Fig. 3.1b, the reference systems $x_\gamma y_\gamma z_\gamma$ follow the rigid rotation ψ of the bodies, thus they are principal.

Due to symmetry, the two bars undergo the same deformation field, which means that the stretches are equal. The expression of the longitudinal stretch of both bars is

$$\lambda_z^\alpha = \lambda_z^\beta = \lambda_z = \frac{l_m}{L_m} = \frac{\sqrt{(B - 2L_r\cos\theta)^2 + (H - \bar{v} - 2L_r\sin\theta)^2}}{\sqrt{(B - 2L_r\cos\theta_0)^2 + (H - 2L_r\sin\theta_0)^2}}.$$

The equilibrium in deformed configuration is expressed by

$$P + 2n\sin\theta = 0, \tag{3.2}$$

where n is the axial force acting on the bars.

As reported in Section 2.4, the solution of the boundary value problem leads to the following relations:

$$\lambda_x = \lambda_y = \sqrt{-\frac{\omega_{,1} + \lambda_z^2\omega_{,2}}{\omega_{,2} + \lambda_z^2\omega_{,3}}}, \tag{3.3}$$

$$n = -2th\lambda_z\left(\omega_{,2}^2 - \omega_{,1}\omega_{,3}\right)\frac{\omega_{,1} + 2\lambda_z^2\omega_{,2} + \lambda_z^4\omega_{,3}}{\left(\omega_{,2} + \lambda_z^2\omega_{,3}\right)^2}, \tag{3.4}$$

where $\omega_{,j} = \partial\omega/\partial\imath_j$ ($j = 1, 2, 3$). By introducing equations (3.1), (3.3) and (3.4) into (3.2), the global equilibrium equation of the von Mises truss becomes

$$P - 4th\lambda_z\frac{H - \bar{v}}{\sqrt{B^2 + (H - \bar{v})^2}}\left(\omega_{,2}^2 - \omega_{,1}\omega_{,3}\right)\frac{\omega_{,1} + 2\lambda_z^2\omega_{,2} + \lambda_z^4\omega_{,3}}{\left(\omega_{,2} + \lambda_z^2\omega_{,3}\right)^2} = 0. \tag{3.5}$$

Equation (3.5) provides a direct relation between external load P and vertical displacement of the apex node $\bar{v}$, namely the equilibrium path.

The equilibrium equation can be alternatively obtained by introducing the total potential energy

$$\Pi(\bar{v}) = 2thL_m\omega - P\bar{v}$$

and its first derivative

$$\frac{\mathrm{d}\Pi}{\mathrm{d}\bar{v}} = 2thL_m \sum_{j=1}^{3} \sum_{k} \omega_{,j} \frac{\partial \imath_j}{\partial \lambda_k} \frac{\partial \lambda_k}{\partial \bar{v}} - P, \quad k = x, y, z.$$

It is straightforward to verify that the stationarity condition $\mathrm{d}\Pi/\mathrm{d}\bar{v} = 0$ corresponds to the equilibrium equation (3.5).

Similarly to what we did in Chapter 2, the stability of the equilibrium solutions is assessed through the energy criterion. In this case, the second derivative of the total potential energy reads

$$\frac{\mathrm{d}^2\Pi}{\mathrm{d}\bar{v}^2} = thL_m \left[\sum_{j=1}^{3} \sum_{k=1}^{3} \omega_{,kj} \left(\sum_{p} \frac{\partial \imath_k}{\partial \lambda_p} \frac{\partial \lambda_p}{\partial \bar{v}} \right) \left(\sum_{q} \frac{\partial \imath_j}{\partial \lambda_q} \frac{\partial \lambda_q}{\partial \bar{v}} \right) + \right.$$
$$\left. \sum_{r=1}^{3} \omega_{,r} \left(\sum_{s} \sum_{t} \frac{\partial^2 \imath_r}{\partial \lambda_t \partial \lambda_s} \frac{\partial \lambda_t}{\partial \bar{v}} \frac{\partial \lambda_s}{\partial \bar{v}} + \sum_{s} \frac{\partial \imath_r}{\partial \lambda_s} \frac{\partial^2 \lambda_s}{\partial \bar{v}^2} \right) \right],$$

with $l, p, r, s = x, y, z$. An equilibrium configuration is stable if the sign of the second derivative of $\Pi(\bar{v})$ is positive.

Since Eulerian buckling is neglected, the unstable phenomenon that takes place in the von Mises truss of Fig. 3.1 is the snap-through. Namely, when the external load reaches its maximum value, the system snaps to a non-adjacent equilibrium configuration.

Fig. 3.2 defines five characteristic configurations: (0) reference configuration, where no external load is applied; (I) first critical point, where the load reaches its maximum value P_{I} and the snap-through activates; (II) self-equilibrated load-free configuration, where the equilibrium takes place in absence of external load even though the stresses in the bars are non-zero; (III) second critical point, where the load reaches the value $P_{\mathrm{III}} = P_{\mathrm{I}}$ and the equilibrium is again stable; (IV) specular undeformed configuration.

The characteristic configurations listed above allow to distinguish four regions: (a) compressive loading region; (b) snap-through region where the equilibrium is unstable; (c) unloading region where the bars are compressed; (d) tension region where the bars are subjected to tension.

As already pointed out, the constitutive behavior of the rubber specimen is described by the compressible Mooney-Rivlin (MR) law. Hence, the equilibrium equation (3.5) is now specialized to the case of compressible MR material. We recall that the MR constitutive law is characterized by the stored energy function

$$\omega(\imath_1, \imath_2, \imath_3) = a\,\imath_1 + b\,\imath_2 + c\,\mu^2 - 2\,(a + 2b + c)\ln\mu - (3a + 3b + c), \tag{3.6}$$

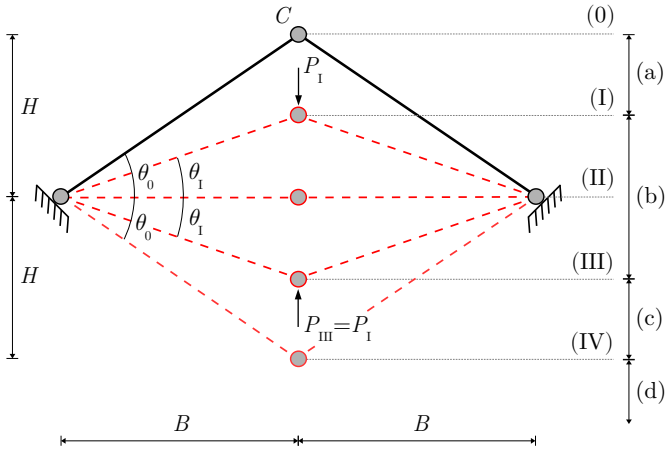

Figure 3.2: Characteristic configurations and regions: (a), (c) and (d) are the stable regions, while (b) is the snap-through region

where a, b and c are positive constants. The derivatives of the stored energy function (3.6) with respect to the invariants are computed and, by substitution into (3.5), the equilibrium equation in case of compressible MR material becomes

$$\hat{P} - \frac{4th}{L} Q\,(H - \bar{v}) = 0, \tag{3.7}$$

where

$$Q = \left(\bar{b}^2 - \bar{c} + G\right) \frac{1 + 2\bar{b}\lambda_z^2 + \lambda_z^4\,(\bar{c} - G)}{\left[\bar{b} + \lambda_z^2\,(\bar{c} - G)\right]^2},$$

$$G = \frac{4(1 + 2\bar{b} + \bar{c})\left(\bar{b} + \bar{c}\lambda_z^2\right)^2}{\lambda_z^2} \left[1 + \bar{b}\lambda_z^2 - \sqrt{4(1 + 2\bar{b} + \bar{c})\left(\bar{b} + \bar{c}\lambda_z^2\right) + \left(1 + \bar{b}\lambda_z^2\right)^2}\right]^{-2},$$

and $\hat{P} = P/a$, $\bar{b} = b/a$, $\bar{c} = c/a$.

3.2 Experimental investigation

In this section, the experimental activities are presented. The material used is a synthetic neoprene rubber with shore hardness 70 ± 5 produced by FIP through polymerization of chloroprene (https://www.fipitaly.it). Experimental uniaxial tests are carried out in order to characterize its behavior when subjected to tension and compression.

The uniaxial tests are briefly described in the following. Afterwards, the experimental device for the test on the von Mises truss is presented in detail. Finally, the digital image correlation (DIC) strategy for the monitoring of the experiment on the von Mises truss is described.

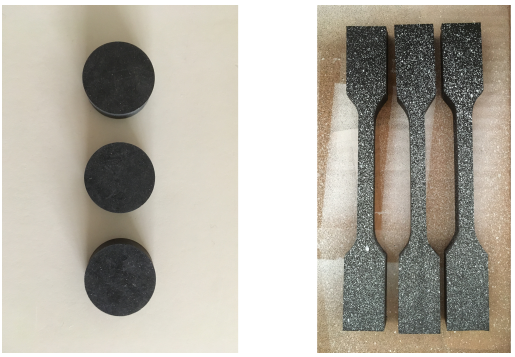

Figure 3.3: Cylindrical and dog-bone specimens used respectively for uniaxial compression and tensile tests

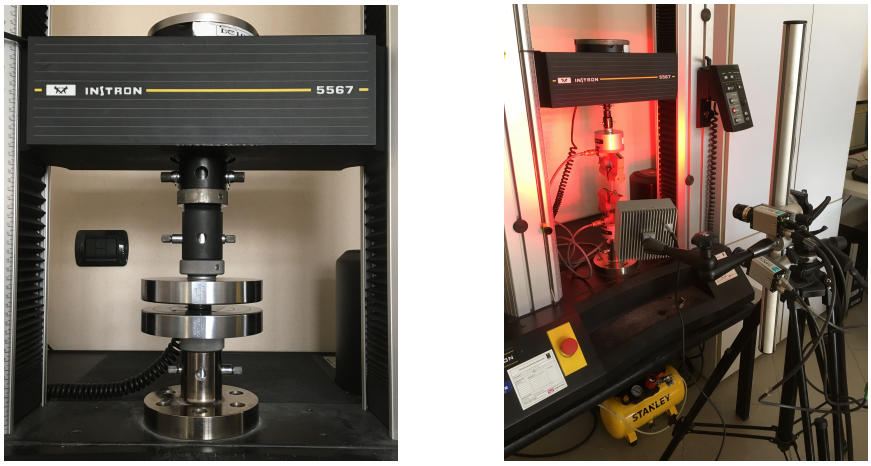

(a) Compression test (b) Tensile test

Figure 3.4: Uniaxial tests for rubber characterization

3.2.1 Uniaxial tests for rubber characterization

The rubber characterization is performed by carrying out separately uniaxial compression and tension tests. The testing machine is the Instron 5567, equipped with a 30 kN load cell for the compression test and a 1 kN load cell for the tension test.

Three squat cylindrical specimens of 28.85 mm diameter and 10.56 mm thickness are tested under compression. Three dog-bone specimens of 83.43 mm^2 cross section area and 65.25 mm effective length are tested under tension (Fig. 3.3). The displacement rate is 0.5 and 50 mm/min for compression and tensile tests, respectively. The setup of both compression and tensile tests is depicted in Fig. 3.4.

Nominal (Piola-Kirchhoff) stress and stretch are computed for each test. The nominal stress vs. stretch curves in compression and tension are merged and the three resulting experimental curves are named S_1, S_2 and S_3. These experimental results are used in Section 3.5.1 to estimate the best fitting parameters of the MR constitutive law.

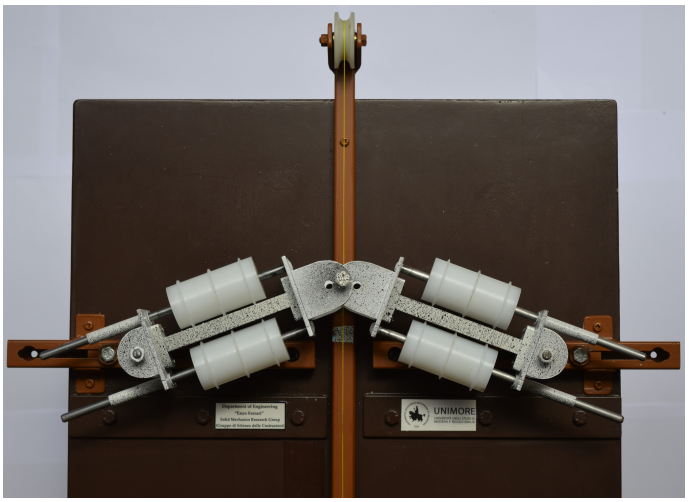

(a) Photo of the top view (XZ plane)

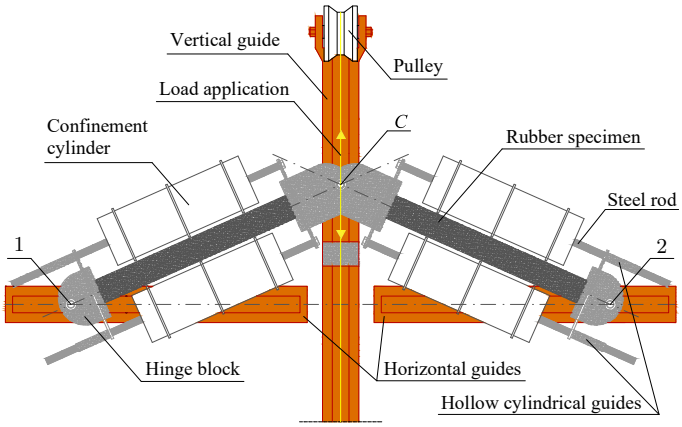

(b) Device components

Figure 3.5: Experimental device for the test on the von Mises truss

3.2.2 Experimental device for the von Mises truss

The experimental device of Fig. 3.5a is designed specifically to simulate the von Mises truss subjected to a vertical load. The device is composed of three steel guides fixed on a supporting table. Control point C is forced to slide along the vertical guide, allowing only the vertical degree of freedom $\bar{v}$. Nodes 1 and 2 are placed on the horizontal guides and their distance can be adjusted according to the geometry of the problem (Fig. 3.5b).

The hinges of the truss are realized with steel blocks that rotate around the corresponding nodes. The hinge in node C is connected to the hinges in 1 and 2 using two steel rods that avoid relative rotations. Namely, the terminal faces of the steel blocks are forced to remain parallel to one another. As shown in Fig.

Table 3.1: Geometry of the von Mises truss and rubber specimen

Parameter	Value	Unit
θ_0	20	deg
L	146.5	mm
L_m	90	mm
L_r	28.25	mm
t	10	mm
h	20.5	mm

3.5a, the steel rods slide through hollow cylindrical guides. This allows the axial deformation of the prismatic rubber specimen, which is glued to the hinge blocks with an adhesion primer for steel-rubber connection.

The theoretical formulation of the equilibrium presented in Section 3.1 does not include Eulerian buckling of the specimens. In order to adhere as much as possible with this, two hollow cylinders made of nylon are inserted in the steel rods. The function of the cylinders is to confine the rubber specimen so as to limit its bending deformation and prevent buckling.

The contact between cylinder and rubber specimen affects the deformation of the rubber. For this reason the cylinders are carved in a way to ensure only three contact points with the specimen. A free space of 0.2 mm between cylinder and specimen is left in order to minimize the influence on the lateral deformation of the rubber.

The concentrated load P is applied through two synthetic fishing lines with a load capacity of 200 N. One end of both the lines is tied to the central hinge C, while the other ends are connected to containers where the load is manually placed. Two pulleys are placed on the two opposite sides of the vertical guide, between hinge C and the load containers. Each line slides through the corresponding pulley. In this way, the vertical load can be applied in both upward and downward directions.

Three pairs of specimens are tested. All the specimens have the same geometry, which is given in Tab. 3.1. The test consists in the application of a load that is gradually increased by adding weight in the container. For each load increment, the vertical displacement of node C is monitored by means of digital image correlation (DIC).

The test starts from the initial configuration (0). The load is applied downwards and the compression of the specimens increases as the load increases, until critical point (I) is reached and snap-through activates downwards. At this point the system is unloaded and the truss attains the specular undeformed configuration (IV). The load is then applied downwards and both specimens are subjected to tension. No unstable phenomena take place. The system is again unloaded and the truss comes back to configuration (IV). The load is now applied upwards and both specimens are subjected to compression until the truss attains critical point (III), where snap-

Figure 3.6: Set up of the DIC instrumentation during the experimental test on the von Mises truss

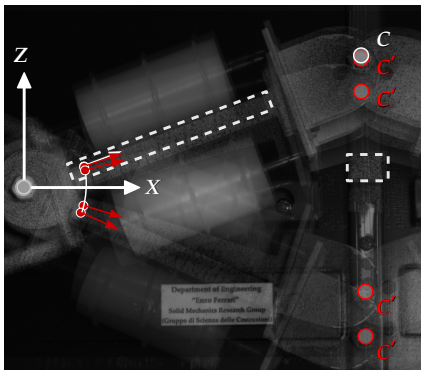

Figure 3.7: View of the DIC cameras with the masks (white dashed frames) monitored during the experimental test

through takes place in the upward direction. The entire equilibrium paths are finally obtained by repeating this procedure for each pair of specimens.

3.2.3 DIC monitoring of the experiment

The displacement field during the experimental test is acquired by means of DIC technology. The instrumentation used is Dantec Dynamics Q400. The DIC monitoring is performed in stereo mode [60] by placing two cameras above the truss (Fig. 3.6). The displacement field is thus captured on the XZ plane at $Y = -t/2$. The optical device calibration and pre-processing operations are such to ensure a resolution of ± 20 μm.

The upper surfaces of the rubber specimens, the hinge blocks and a portion of the vertical guide are painted with a random pattern for the DIC monitoring. Two masks are then defined for the displacement field monitoring. The investigated masks are shown in Fig. 3.7 with framed white dashed areas. One mask is set on the vertical guide to acquire the displacement of control point C. The other mask traces the margins of the left rubber specimen and it is used to obtain the displacement

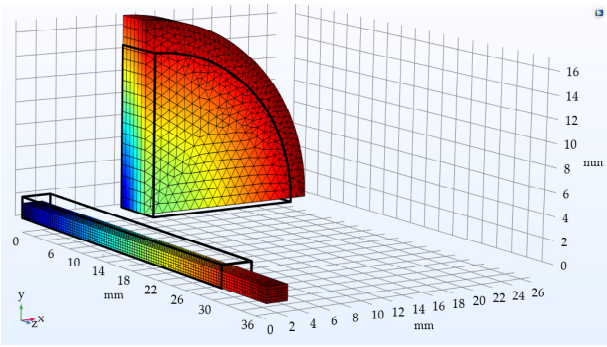

Figure 3.8: FE models for rubber characterization: Prismatic specimen under tension and cylindrical specimen under compression

field of the specimen itself. Note that, given the symmetry of the problem, only the displacement field of the left rubber specimen is monitored.

The DIC cameras acquire a single frame for each load step. The data resulting from the DIC monitoring of the experimental tests are discussed in Section 3.5.2.

3.3 Finite element (FE) analysis

The FE models are realized by using the FE code COMSOL Multiphysics® v.5.5 [61]. Four different FE models are created: two for the rubber characterization, one for compression and one for tension; two for the von Mises truss, which differ only in an internal solid constrain. A detailed description of each model is given in the following.

3.3.1 Models for rubber characterization

The FE constitutive curve is obtained by reproducing compression and tension tests on cylindrical and dog-bone specimens respectively. The rubber specimens are modeled in agreement with the samples geometries described in Section 3.2.2.

For the tension test, only the effective length of the dog-bone is modeled. Due to symmetry conditions, only one fourth of the specimen is modeled, as shown in Fig. 3.8. The displacement component normal to each plane of symmetry is neglected.

The material is defined by setting the MR stored energy function (3.6) in the user defined material. Tetrahedral elements are used for compression while hexagonal elements for tension. In both cases, quadratic serendipity shape functions are employed.

A nonlinear incremental analysis is performed by applying a displacement in the z direction at the final cross section of the solid, as shown in Fig. 3.8. The incremental steps are -0.005 and 0.5 mm for compression and tension respectively. The inertial load is not taken into account.

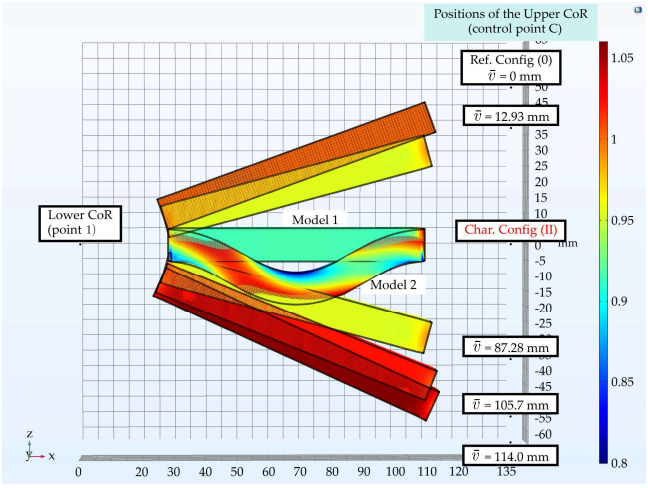

Figure 3.9: Details of the FE models: mesh, centers of rotation (CoR) and deformed configurations with contour plot of stretch λ_z. The deformed configuration at point (II) shows that Eulerian buckling takes place in model 2 but not in model 1

3.3.2 Models for the von Mises truss

Two FE models are built for the simulation of the von Mises truss. The first model, named model 1, does not include Eulerian buckling of the rubber specimen. This model simulates the condition of the experimental test performed in this work, where the confinement cylinders prevent buckling phenomena. The second model, named model 2, simulates the response of the system without confinement cylinders. In this circumstance buckling plays an important role, which is discussed in detail in Section 3.5.3. Model 1 differs from model 2 only for an added constraint in order to avoid Eulerian buckling.

In both FE models, the MR material is defined in the same way of the previous section. The specimen geometries are set according to Tab. 3.1. Hexagonal elements with quadratic serendipity shape functions are used for the mesh.

Two symmetry conditions are employed. Firstly, only one bar is modeled because of the symmetry with respect to the vertical axis through the central node C. Secondly, only half of the bar is modeled thanks to the symmetry with respect to the XZ plane at $Y = 0$.

The hinge blocks are accounted for by using the feature rigid connector of the FE code. The rigid connector is a COMSOL constraining tool which attributes to a surface domain the rigid constraint associated to a moving or fixed center of rotation. The offset of the center of rotation with respect to the centroid of the surface element is L_r, which is the size of the hinge block. The final cross sections of the rubber specimen are constrained through two rigid connectors that are associated to the points 1 and C of Fig. 3.9.

A lower rigid connector is applied to the lower final cross section of the rubber specimen and associated to the fixed center of rotation 1. Likewise, an upper rigid connector is attributed to the final cross section of the rubber specimen and

associated to the moving center of rotation C.

A nonlinear incremental analysis is performed by applying a vertical displacement $\bar{v}$ at the upper center of rotation C. The incremental displacement step is -0.1 mm, ranging in the interval $\bar{v} \in [0, -3H]$. In addition, both rigid connectors are constrained to rotate of the rigid rotation $\psi(\bar{v})$ around the corresponding center of rotation. This constraint ensures that the final cross sections of the specimen remain coaxial during the deformation.

As previously pointed out, model 1 contains an additional constraint to the ones described above. Specifically, also the middle cross section of the specimen is constrained to rotate by $\psi(\bar{v})$ around the lower center of rotation 1. This kinematic constraint of model 1 ensures the absence of Eulerian buckling in the solution. In fact, the deformed configurations of Fig. 3.9 show that at the characteristic point (II) only model 2 is affected by buckling.

3.4 Fitting of the constitutive model

Stress and stretch data obtained from the uniaxial tests are used to perform a nonlinear fitting of the MR constitutive parameters a, b and c.

The parameters are collected into the parameter vector $\mathbf{q} = [a, b, c]^T$. The fitting function $f(\lambda_z, \mathbf{q})$ is the nominal stress vs. stretch relation for a compressible MR material, which is obtained by writing the expression of the axial force (3.4) in case of MR material and diving by the cross section area th. The objective function $\mathrm{obj}(\mathbf{q})$ is defined as the averaged sum of normalized square error between simulated and experimental data, namely

$$\mathrm{obj}(\mathbf{q}) = \sqrt{\frac{\sum_i^m \left[f(\lambda_{zi}, \mathbf{q}) - f_i\right]^2}{\sum_i^m f(\lambda_{zi}, \mathbf{q})^2}}, \tag{3.8}$$

where m is the number of data points, f_i and λ_{zi} are experimental nominal stress and stretch respectively, while $f(\lambda_{zi}, \mathbf{q})$ is the fitting function sampled at the data points.

The minimization of the objective function (3.8) is performed via a genetic algorithm [62]. Specifically, the fitting procedure is implemented in a MATLAB® code by using the *ga* function of the *global optimization toolbox*.

At first, an unconstrained optimization was carried out. The optimal value of parameter c provided by the algorithm was six orders of magnitude larger than parameters a and b ($\bar{c} \approx 10^6$). Although the stress vs. stretch curve was accurately depicted, this result was treated with suspicion. In fact, an application to the nonlinear bending theory [55] led to unsatisfying results. Therefore, a constrained optimization was later carried out. The following lower and upper bounds of parameters were set:

$$a \in [10^2, 10^4], \qquad b \in [10^2, 10^4], \qquad c \in [10^3, 2 \times 10^5],$$

where the values are expressed in kPa.

Table 3.2: Best fitting parameters of the Mooney-Rivlin material

Const. param.	Experimental curve			Mean± Dev.St
	S_1	S_2	S_3	
a (kPa)	442	461	468	457 ± 13
b (kPa)	391	366	386	381 ± 13
c (kPa)	35092	30211	29971	31758 ± 2889
obj($\mathbf{q}$) (%)	6.04	5.12	5.10	-

3.5 Results and discussion

The first part of this section presents the experimental results of the rubber characterization, which are also put in comparison with analytic and FE constitutive behaviors of the rubber. Subsequently, the results of the test on the von Mises truss are presented and compared with analytical and FE simulations. Finally, further considerations on Eulerian buckling are given.

3.5.1 Results of the rubber characterization

The constrained optimization is carried out for the three experimental stress vs. stretch curves S_1, S_2 and S_3 resulting from the experimental uniaxial tests. The best fitting parameters obtained are listed in Tab. 3.2.

The values of the objective function are around $5-6\%$, which indicate that the results of the optimization are accurate. Tab. 3.2 shows also mean value and standard deviation of each parameter over the three simulations. The standard deviation of parameter c is not very low, but its variations do not influence much the constitutive response, therefore this result is still considered reliable. The mean values of constitutive parameters a, b and c are thus chosen as optimal set of parameters.

The optimal set of parameters is introduced into the fitting function and into the FE model. The resulting analytic and FE stress vs. stretch curves are shown in Fig. 3.10, along with the experimental one.

Analytic and FE curves are both derived with homogeneous deformations and MR constitutive law, thus they perfectly overlap. Well agreement is also found with the experimental data in compression, while in tension it is evident that the MR constitutive law is not capable of accurately describe the constitutive behavior of the rubber. However, the stretch of the rubber specimen during the experimental test on the von Mises truss ranges in the gray area of Fig. 3.10. Within this range, both compression and tension are satisfactorily depicted by both analytic and FE curves.

Although in the range of interest the result is accurate enough, some considerations must be made. The detail of Fig. 3.10 shows that, for relatively small contractions of the bars, the experimental constitutive behavior is stiffer than the

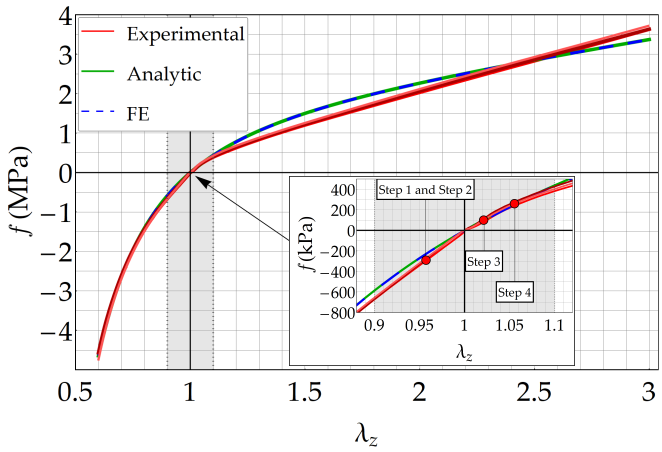

Figure 3.10: Experimental, analytic and FE constitutive behaviors (nominal stress f vs. stretch λ_z) obtained with the mean values of the best fitting parameters, given in Tab. 3.2

analytic one. On the contrary, small extensions are well described by the analytic constitutive law. However, while the extension increases, the accuracy of the analytic law with respect to the experimental data decreases. In particular, the experimental curve is less stiff.

3.5.2 Results of the test on the von Mises truss

The equilibrium paths derived from experimental tests, analytic model and FE simulation are shown in Fig. 3.11. Displacement $\bar{v}$ is normalized with respect to the height H of the truss and load P is normalized with respect to the Eulerian buckling load of the system in undeformed configuration, expressed as

$$P_{\text{bk}} = \frac{8\pi^2 E I_x}{L_m^2} \sin(\theta_0), \tag{3.9}$$

where I_x is the cross section's moment of inertia with respect to axis x and E is the Young's modulus of the rubber, which is computed using (2.74)

$$E = \frac{4(a+b)(a+4b+3c)}{a+3b+2c}. \tag{3.10}$$

Note that the rubber specimens are considered clamped to the hinge blocks. Accordingly, relation (3.9) is derived introducing the buckling load of a double-clamped beam $n_{\text{bk}} = 4\pi^2 E I_x / L_m^2$ into (3.2).

Overall, there is a good agreement between experimental, analytic and FE equilibrium paths. The three main reasons of discrepancy between results are discussed in the following.

Firstly, the equilibrium equation (3.7) is based on the hypothesis of homogeneous deformation. However, for both FE model and experimental test this is not true.

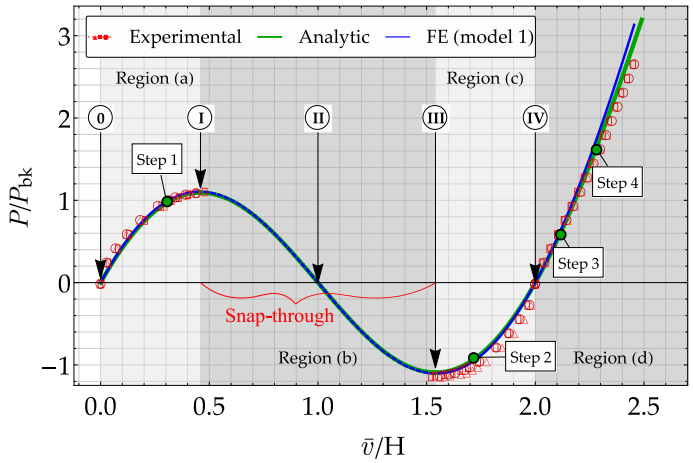

Figure 3.11: Experimental, analytic and FE equilibrium paths of the von Mises truss subjected to a vertical load

In both cases the final cross sections of the specimen are clamped to the rigid hinge blocks. This influences the deformation of the areas near the hinges.

Secondly, as shown in Fig. 3.10, the experimental constitutive behavior is sensibly stiffer than the analytic one for relatively small contractions of the bars. This explains why for both regions (a) and (c) of Fig. 3.11 the experimental data show higher stiffness. On the contrary, small extensions are well described by the analytic constitutive law. Indeed, experimental data in region (d) fit well the analytic curve. However, as the extension increases, the discrepancy between experimental, analytic and FE results increases as well. This because the accuracy of the analytic constitutive law decreases for large extensions.

Lastly, geometric imperfections and friction in the guides of the experimental device play a role on accuracy of the data. Although friction is reduced by using lubricant, its contribute is not negligible for low values of load. In fact, it contributes to increase the stiffness of the experimental curve close to points (0) and (IV).

Four reference steps in terms of applied load are selected and reported in Fig. 3.11. The values of normalized displacement $\hat{v} = \bar{v}/H$ of node C are given in Tab. 3.3, for each reference step and for critical points (I) and (III). Relative errors of FE simulation and experimental tests with respect to the analytic solution are also given.

The highest experimental errors are committed close to critical points (I) and (III) because it is hard to catch the exact configuration where snap-through takes place. Indeed, the reference load steps with highest errors are step 1 and step 2, due to their proximity to the critical points. Overall, the results are satisfactory and the errors are very low. The maximum error committed is 13%, which is largely acceptable.

Table 3.3: Normalized displacement $\hat{v} = \bar{v}/H$ and relative error $\mathrm{e}_r = |1 - \hat{v}/\hat{v}_{\mathrm{Analytic}}|$

Step	Analytic	FEM		Experimental					
				S_1		S_2		S_3	
	$\hat{v}$	$\hat{v}$	$\mathrm{e_r}(\%)$	$\hat{v}$	$\mathrm{e_r}(\%)$	$\hat{v}$	$\mathrm{e_r}(\%)$	$\hat{v}$	$\mathrm{e_r}(\%)$
1	0.291	0.280	3.78	0.293	0.546	0.280	3.87	0.264	9.27
2	1.71	1.72	0.431	1.78	3.92	1.74	1.68	1.74	1.96
3	2.12	2.11	0.331	2.11	0.0916	2.10	0.775	2.11	0.188
4	2.28	2.26	0.702	2.30	0.930	2.28	0.147	2.30	0.837
Char.pts.	$\hat{v}$	$\hat{v}$	$\mathrm{e_r}(\%)$	$\hat{v}$	$\mathrm{e_r}(\%)$	$\hat{v}$	$\mathrm{e_r}(\%)$	$\hat{v}$	$\mathrm{e_r}(\%)$
(I)	0.459	0.399	13.0	0.415	9.59	0.442	3.77	0.440	4.15
(III)	1.54	1.60	3.61	1.66	7.68	1.58	2.59	1.60	4.03

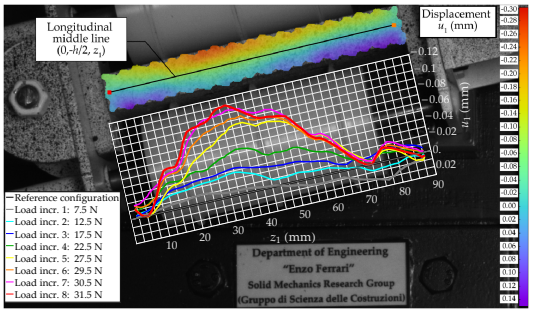

Figure 3.12: Line plots and contour plot at load increment 8 of displacement component u_1 in the principal reference system $x_1y_1z_1$ for the specimen S_3

3.5.3 Considerations on Eulerian buckling of the rubber specimens

The experimental device described in Section 3.2.2 is specifically designed to avoid Eulerian buckling of the rubber specimen. Fig. 3.12 shows a contour plot of the transversal displacement component u_1 at load increment 8 and the line plots of $u_1(0, -t/2, z_1)$.

From Fig. 3.12, it is clear that a slight bending deformation occurred during the tests, but it was contained by the nylon cylinders. In particular, the values of u_1 at load increments 1 and 2 are less than the DIC accuracy (± 20 μm). This indicates that actual buckling phenomena took place presumably between load increments 3 and 5, for an applied load between 17.5 N and 27.5 N. After load increment 5, the transversal displacement profiles are much closer to each other. This reveals that the specimen is crushing against the cylinder and the confinement effect activates, limiting the bending deformation and ensuring a behavior as close as possible to a homogeneous deformation. The necessity of the confinement cylinders in the experimental tests is thus confirmed.

The experimental evidence of buckling is supported by the simulation provided

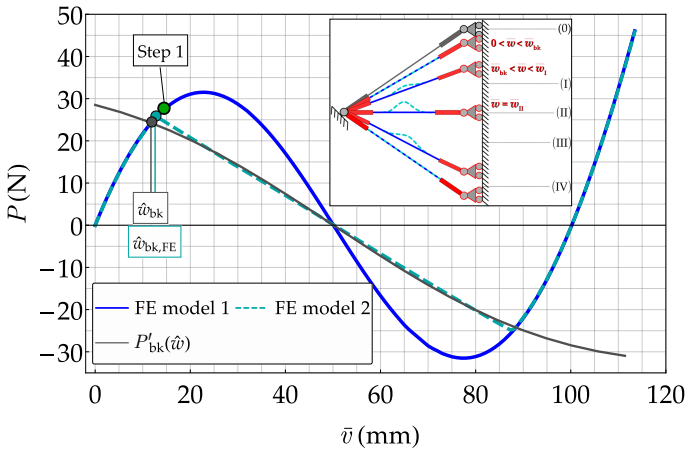

Figure 3.13: Equilibrium paths of the FE models and analytic Eulerian buckling load computed in deformed configuration

by FE model 2, the outcome of which is shown in Fig. 3.13. The load paths of model 1 and model 2 perfectly agree until the critical buckling load is reached at $\bar{v}_{bk,FE} = 12.97$ mm ($\hat{v}_{bk,FE} = 0.259$). At this point, model 2 experiences buckling and deviates from model 1. This would be the behavior of the truss in the event that the confinement cylinders are removed.

From an analytic point of view, buckling occurs at the intersection between equilibrium path and Eulerian buckling load [25]. The Eulerian buckling load of the system in deformed configuration is computed as

$$P'_{bk}(\bar{v}) = \frac{8\pi^2 E I_x}{l_m^2} \sin\theta \tag{3.11}$$

and it is represented with the gray curve in Fig. 3.13. Equation (3.11) shows dependence on the constitutive parameters through E, which is given by (3.10), and on the geometry of the system through l_m and I_x.

The intersection between analytic equilibrium path, given by (3.7), and analytic Eulerian buckling load, expressed by (3.11), takes place at $\bar{v}_{bk} = 11.78$ mm ($\hat{v}_{bk} = 0.235$). There is a relative error of 10.2% between analytic critical displacement $\bar{v}_{bk}$ and FE critical displacement $\bar{v}_{bk,FE}$. This mismatch is mainly due to the linearization of the constitutive behavior. In fact, since the constitutive behavior of rubber is nonlinear, the value of E in equation (3.11) should be updated while the configuration of the truss changes. It is worth mentioning that also I_x undergoes slight changes while the specimen deforms, but this contribution is also neglected. Despite the above simplifying assumptions, buckling predicted analytically is still in good agreement with the FE simulation.

As previously mentioned, during the experimental test buckling took place with a load between 17.5 N and 27.5 N, and it was then contained by the confinement cylinders. The critical load of the FE simulation is 25.66 N, which in some way agrees with the experimental observation. Clearly, buckling in the experimental test

arose earlier than the FE prediction because of the geometrical imperfections of specimens and device. Note that, since the confinement cylinders promptly stopped buckling phenomena during the test, its effect on the experimental equilibrium path is almost negligible.

3.6 Comments on the validity of the proposed analytical model

Both experimental results and FE simulation agree well with analytical results. This provides a validation of the theoretical formulation presented in this thesis, which is entirely developed in the context of finite elasticity. The analytical model gives an accurate description of equilibrium and post-critical behavior of truss structures, therefore it represents an important tool for the validation of numerical simulations.

The confinement cylinders of the experimental device ensure that Eulerian buckling is promptly stopped, thus allowing to observe the classical snap-through instability. In the event that the confinement cylinders are removed, the system experiences buckling and the equilibrium path deviates from the analytical one. This interaction between snap-through and Eulerian buckling will be further examined in forthcoming research. Theoretical formulations will be developed and new experimental tests will be carried out.

Chapter 4

Equilibrium paths for the three-bar truss in finite elasticity with an application to graphene

In this chapter, we extend the nonlinear formulation developed in Chapter 2 to the case of the three-bar truss, which is depicted in Fig. 4.1. Based on the formulation provided by Kwasniewski [1], Rezaiee-Pajand and Naghavi [6] derived the analytical solution of this problem for the vertical load case. It was found out that, differently from the von Mises truss, the presence of the upper bar renders the system always stable. Cengiz Toklu et al. [63] analyzed the same three-bar truss using a total potential optimization algorithm. The equilibrium was solved for three levels of vertical load, showing that the system undergoes a snap-through. In both the works [6] and [63] asymmetrical equilibrium configurations were not detected. However, such apparently simple results are affected by the assumptions of moderately small strains and linear constitutive law. In this work, such hypotheses are removed and an exact formulation in finite elasticity is provided.

An application assuming a compressible Mooney-Rivlin material is reported. It is discovered that, taking into account both geometric and material nonlinearities, the three-bar truss analyzed shows unexpectedly complex responses. In particular, for both vertical and horizontal load cases, primary and secondary branches of equilibrium are detected, showing interesting post-critical behaviors involving multiple critical points and stable asymmetric configurations. Exact closed-form solutions of this nonlinear problem have great importance as benchmark tests for finite element simulations and other numerical procedures.

The truss structure considered in this chapter is also representative for the analysis of the in-plane mechanical behavior of the representative cell of the hexagonal nanostructure of graphene [7], which has gained tremendous interest in the research on innovative materials. It is widely known that, under a generic state of tension at room temperature, this material can experience strains larger than 15-20% prior

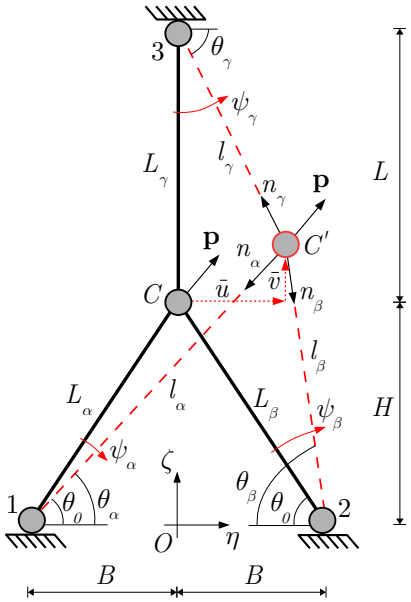

Figure 4.1: The three-bar truss in undeformed and deformed configurations. Central node C undergoes displacement $\mathbf{s}$, with components $\bar{u}$ and $\bar{v}$

to failure [64–67]. In light of this, an exhaustive analysis of the mechanical behavior of graphene should account for finite deformations and material nonlinearities, considering also possible unstable phenomena.

The general formulation of the equilibrium of the three-bar truss is therefore specialized to the geometry of the representative cell of graphene. The C-C (covalent) bonds are viewed as bars of the truss structure. It goes without saying that this chapter is not focused on the accurate description of the mechanical behavior of graphene subjected to finite deformations, which will be investigated in the next chapter. In fact, the bars describe only the covalent bonds between carbon atoms, while angular and long range interactions are not taken into account. Nevertheless, this application allows interesting conclusions on the interactions among atoms inside the graphene honeycomb lattice, which can influence the macroscopic behavior of this material. Moreover, the simple applications reported in this chapter show complex behaviors that are not usually observed in ordinary structures.

The chapter is structured as follows. Kinematic quantities and equations expressing the global equilibrium of the system are introduced. The longitudinal stretches of the bars are derived considering two degrees of freedom for the central node (horizontal and vertical components of displacement). Displacement fields and deformation gradients of the bars are expressed. As for the von Mises truss, the bars are regarded as three-dimensional bodies subjected to homogeneous deformations. Again, this assumption implies that the Euler load of each bar is large enough to avoid buckling phenomena. The boundary-value problem for the bars subjected to uniaxial tractions is then formulated and the equilibrium equations of each body are derived. Thanks to this result, the global equilibrium equations of the three-bar

truss for a general homogeneous, hyperelastic and isotropic material are written. Applications to compressible Mooney-Rivlin materials and to the representative cell of the graphene sheet are presented. For both cases, the equilibrium equations are specialized by introducing the corresponding strain energy functions. Consequently, the equilibrium paths are presented, including the stability analysis.

4.1 Preliminaries and basic equations

The three-bar truss of Fig. 4.1 is composed of three equal straight bars, denoted by the symbols α, β and γ. The three bars are hinged at the central node C and the truss is loaded by a dead force $[\mathbf{p}] = [p_\eta, p_\zeta]^T$, where η and ζ are the axes of the global Cartesian reference system. The joints located at the vertices are identified by 1, 2 and 3, following a counter-clockwise order. All the joints are assumed to behave as frictionless hinges. Therefore, the bars experience only axial forces.

The lengths of the bars in the initial (undeformed) configuration are

$$L_\delta = L = \sqrt{B^2 + H^2}, \quad \delta = \alpha, \beta, \gamma,$$

where B and H are the projections of both bars α and β along the η and ζ axes, respectively. The central node C undergoes the displacement $[\mathbf{s}] = [\bar{u}, \bar{v}]^T$. Hence, the lengths of the bars in deformed configuration become

$$\begin{aligned} l_\alpha &= \sqrt{(B+\bar{u})^2 + (H+\bar{v})^2}, \\ l_\beta &= \sqrt{(B-\bar{u})^2 + (H+\bar{v})^2}, \\ l_\gamma &= \sqrt{\bar{u}^2 + (L-\bar{v})^2}. \end{aligned} \tag{4.1}$$

The three bars are regarded as three-dimensional bodies composed of the same homogeneous and isotropic hyperelastic material. The principal stretches are denoted by λ_j^δ ($\delta = \alpha, \beta, \gamma$ and $j = x, y, z$). The superscript represents the body while the subscript indicates the local reference system of the body itself, which is principal (Fig. 4.2). The longitudinal stretches are thus expressed as

$$\begin{aligned} \lambda_z^\alpha &= \frac{l_\alpha}{L} = \frac{\sqrt{(B+\bar{u})^2 + (H+\bar{v})^2}}{L}, \\ \lambda_z^\beta &= \frac{l_\beta}{L} = \frac{\sqrt{(B-\bar{u})^2 + (H+\bar{v})^2}}{L}, \\ \lambda_z^\gamma &= \frac{l_\gamma}{L} = \frac{\sqrt{\bar{u}^2 + (L-\bar{v})^2}}{L}. \end{aligned} \tag{4.2}$$

The equilibrium of the three-bar truss in deformed configuration reads

$$\begin{aligned} p_\eta - n_\alpha c_\alpha + n_\beta c_\beta - n_\gamma c_\gamma &= 0, \\ p_\zeta - n_\alpha s_\alpha - n_\beta s_\beta + n_\gamma s_\gamma &= 0, \end{aligned} \tag{4.3}$$

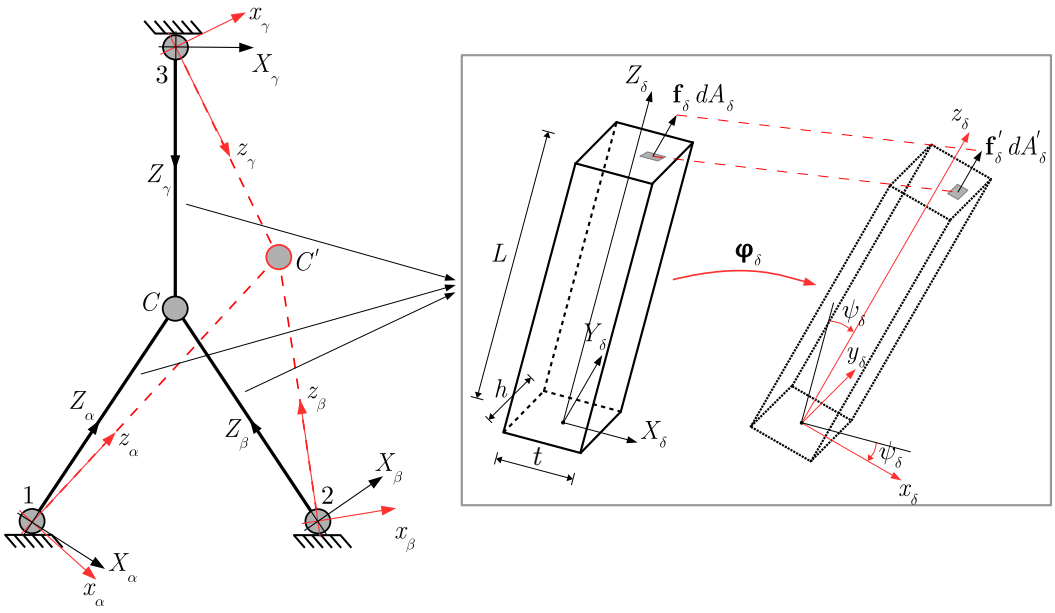

Figure 4.2: Representation of local reference systems of the bodies (rectangular prisms), deformation and surface tractions

where n_α, n_β and n_γ are, respectively, the axial forces acting on the bars α, β and γ, while

$$\begin{aligned} c_\alpha &= \cos\theta_\alpha = \frac{B+\bar{u}}{l_\alpha}, \qquad & s_\alpha &= \sin\theta_\alpha = \frac{H+\bar{v}}{l_\alpha}, \\ c_\beta &= \cos\theta_\beta = \frac{B-\bar{u}}{l_\beta}, \qquad & s_\beta &= \sin\theta_\beta = \frac{H+\bar{v}}{l_\beta}, \\ c_\gamma &= \cos\theta_\gamma = \frac{\bar{u}}{l_\gamma}, \qquad & s_\gamma &= \sin\theta_\gamma = \frac{L-\bar{v}}{l_\gamma}, \end{aligned} \tag{4.4}$$

in which θ_α, θ_β and θ_γ are the angles between the bars and the axis η, as shown in Fig. 4.1.

4.2 Displacement field and deformation

A material coordinate system $X_\delta, Y_\delta, Z_\delta$ $(\delta = \alpha, \beta, \gamma)$ with the origin in the corresponding node 1, 2 and 3 is defined for each body (see Fig. 4.2). For the sake of simplicity, the bodies have the shape of rectangular prisms with t, h and L that denote width, height and length, respectively. The formulation can be readily extended to generic cross sections. The deformation of each body is assumed to be homogeneous, namely the deformation gradient is constant, as occurs to non-slender bars subjected to axial forces. The Euler's critical load is considered large enough to avoid buckling phenomena.

The bodies are subjected to surface tractions only, whereas body forces are disregarded. The surface tractions are the consequence of the application of the external

force $\mathbf{p}$ to the central node C and are assumed to be uniformly and orthogonally distributed on the basis of the bodies in the deformed configuration. As for the von Mises truss, $\mathbf{p}$ is considered as a dead force and does not depend on the configuration assumed by the structure after the deformation. However, the axial force n_δ acting on the δ-th bar depends on the configuration assumed by the bar itself. Accordingly, n_δ is a function of the displacement components $\bar{u}$ and $\bar{v}$.

Position vector $\mathbf{id}(P)$ and displacement vector $\mathbf{u}_\delta(P)$ are defined as

$$\begin{aligned}\mathbf{id}(P) &= X_\delta \mathbf{i}_\delta + Y_\delta \mathbf{j}_\delta + Z_\delta \mathbf{k}_\delta,\\ \mathbf{u}_\delta(P) &= u_\delta(P)\mathbf{i}_\delta + v_\delta(P)\mathbf{j}_\delta + w_\delta(P)\mathbf{k}_\delta,\end{aligned}$$

where $\mathbf{i}_\delta$, $\mathbf{j}_\delta$ and $\mathbf{k}_\delta$ are the unit vectors of the material coordinate system $X_\delta, Y_\delta, Z_\delta$. The deformation $\boldsymbol{\varphi}_\delta$ of the δ-th body consists of a rigid rotation ψ_δ around the corresponding hinged joint and a pure deformation, described by the longitudinal and transversal stretches. By summing these two contributions, the displacement field reads

$$\begin{cases} u_\delta = X_\delta\left(\lambda_x^\delta \cos\psi_\delta - 1\right) + Z_\delta \lambda_z^\delta \sin\psi_\delta \\ v_\delta = Y_\delta\left(\lambda_y^\delta - 1\right) \\ w_\delta = -X_\delta \lambda_x^\delta \sin\psi_\delta + Z_\delta\left(\lambda_z^\delta \cos\psi_\delta - 1\right), \quad \delta = \alpha,\beta,\gamma. \end{cases} \tag{4.5}$$

It is obvious that the displacement field of the bodies of the three-bar truss (4.5) corresponds to that of the bodies of the von Mises truss, expressed by (2.7).

The material gradient of the displacement field (4.5) yields

$$[\mathbf{H}_\delta] = \begin{bmatrix} \lambda_x^\delta \cos\psi_\delta - 1 & 0 & \lambda_z^\delta \sin\psi_\delta \\ 0 & \lambda_y^\delta - 1 & 0 \\ -\lambda_x^\delta \sin\psi_\delta & 0 & \lambda_z^\delta \cos\psi_\delta - 1 \end{bmatrix}, \quad \delta = \alpha,\beta,\gamma,$$

from which the expression of the deformation gradient is obtained

$$[\mathbf{F}_\delta] = \begin{bmatrix} \lambda_x^\delta \cos\psi_\delta & 0 & \lambda_z^\delta \sin\psi_\delta \\ 0 & \lambda_y^\delta & 0 \\ -\lambda_x^\delta \sin\psi_\delta & 0 & \lambda_z^\delta \cos\psi_\delta \end{bmatrix}, \quad \delta = \alpha,\beta,\gamma.$$

4.3 Equilibrium configurations of the three-bar truss

In this section, the equilibrium equations of the fully nonlinear problem for the three-bar truss are obtained. Firstly, the boundary-value problem is formulated, thereby providing the equations governing the equilibrium of each body of the truss. Subsequently, the global equilibrium equations of the central node in the deformed configuration are written.

The boundary-value problem is formulated in the same way as done in Section 2.3. Hence, we assume that the material is frame-indifferent and isotropic. The stored energy function ω_δ of the δ-th body depends only on the principal invariants $\imath_j^\delta$ $(j = 1,2,3)$ of the left Cauchy-Green deformation tensor $\mathbf{B}_\delta$. The (first) Piola-Kirchhoff stress tensor is given by the constitutive equation (2.10). Local equilibrium

and boundary conditions are expressed according to equations (2.12) and (2.13), respectively.

The constitutive relation for the Piola-Kirchhoff stress tensor along with the boundary conditions provide the following equations governing the equilibrium of the δ-th body [36, 56]:

$$\omega_{\delta,1} + \left[\left(\lambda_z^\delta\right)^2 + \left(\lambda^\delta\right)^2\right]\omega_{\delta,2} + \left(\lambda^\delta\right)^2\left(\lambda_z^\delta\right)^2\omega_{\delta,3} = 0, \tag{4.6}$$

$$2\lambda_z^\delta\left[\omega_{\delta,1} + 2\left(\lambda^\delta\right)^2\omega_{\delta,2} + \left(\lambda^\delta\right)^4\omega_{\delta,3}\right] = f_\delta, \quad \delta = \alpha,\beta,\gamma, \tag{4.7}$$

where $\omega_{\delta,j} = \frac{\partial\omega_\delta}{\partial\iota_j^\delta}$ $(j = 1,2,3)$ and $\lambda^\delta = \lambda_x^\delta = \lambda_y^\delta$, as a consequence of the isotropy of the material. Since kinematics and assumptions are the same as the case of the bodies composing the von Mises truss, equations (4.6) and (4.7) correspond to equations (2.20) and (2.21). Equation (4.6) gives the relation between transversal stretch and longitudinal stretch

$$\lambda^\delta = \sqrt{-\frac{\omega_{\delta,1} + \left(\lambda_z^\delta\right)^2\omega_{\delta,2}}{\omega_{\delta,2} + \left(\lambda_z^\delta\right)^2\omega_{\delta,3}}}, \quad \delta = \alpha,\beta,\gamma.$$

The surface tractions acting on deformed and undeformed configurations are related through expression (2.25) and the transformation of the area element dA_δ from undeformed to deformed configuration (dA'_δ) is expressed by the Nanson's formula (2.27). Combining these relations (see Section 2.4), the modulus of the axial force acting on the δ-th body in deformed configuration is computed as

$$n_\delta = -\frac{2bh\lambda_z^\delta\left(\omega_{\delta,2}^2 - \omega_{\delta,1}\omega_{\delta,3}\right)\left[\omega_{\delta,1} + 2\left(\lambda_z^\delta\right)^2\omega_{\delta,2} + \left(\lambda_z^\delta\right)^4\omega_{\delta,3}\right]}{\left[\omega_{\delta,2} + \left(\lambda_z^\delta\right)^2\omega_{\delta,3}\right]^2}, \quad \delta = \alpha,\beta,\gamma. \tag{4.8}$$

Through (4.8) and the geometrical relations (4.4), the equilibrium equations of the three-bar truss (4.3) assume the following form:

$$\begin{aligned} p_\eta + \frac{2bh}{L}\left[G_\alpha\left(B + \bar{u}\right) - G_\beta\left(B - \bar{u}\right) + G_\gamma\bar{u}\right] = 0, \\ p_\zeta + \frac{2bh}{L}\left[\left(G_\alpha + G_\beta\right)\left(H + \bar{v}\right) - G_\gamma\left(L - \bar{v}\right)\right] = 0, \end{aligned} \tag{4.9}$$

where

$$G_\delta = \frac{\left(\omega_{\delta,2}^2 - \omega_{\delta,1}\omega_{\delta,3}\right)\left[\omega_{\delta,1} + 2\left(\lambda_z^\delta\right)^2\omega_{\delta,2} + \left(\lambda_z^\delta\right)^4\omega_{\delta,3}\right]}{\left[\omega_{\delta,2} + \left(\lambda_z^\delta\right)^2\omega_{\delta,3}\right]^2}, \quad \delta = \alpha,\beta,\gamma.$$

The stability of the equilibrium solutions is assessed through the energy criterion, which was already explained in detail in Section 2.4. The total potential energy of the system is

$$\Pi(\bar{u},\bar{v}) = bhL\sum_\delta \omega_\delta - p_\eta\bar{u} - p_\zeta\bar{v}, \quad \delta = \alpha,\beta,\gamma,$$

from which the components of the Hessian matrix, expressed by (2.37), are computed by applying the chain rule twice

$$\begin{aligned}\frac{\partial^2\Pi}{\partial u_j\partial u_i} = bhL\sum_{\delta}\Bigg[\sum_{h=1}^{3}\sum_{k=1}^{3}\omega_{\delta,kh}\left(\sum_{l}\frac{\partial\imath_k^\delta}{\partial\lambda_l^\delta}\frac{\partial\lambda_l^\delta}{\partial u_j}\right)\left(\sum_{p}\frac{\partial\imath_h^\delta}{\partial\lambda_p^\delta}\frac{\partial\lambda_p^\delta}{\partial u_i}\right)\\ +\sum_{h=1}^{3}\omega_{\delta,h}\left(\sum_{r}\sum_{s}\frac{\partial^2\imath_h^\delta}{\partial\lambda_s^\delta\partial\lambda_r^\delta}\frac{\partial\lambda_s^\delta}{\partial u_j}\frac{\partial\lambda_r^\delta}{\partial u_i}+\sum_{r}\frac{\partial\imath_h^\delta}{\partial\lambda_r^\delta}\frac{\partial^2\lambda_r^\delta}{\partial u_j\partial u_i}\right)\Bigg],\\ \delta=\alpha,\beta,\gamma,\quad i,j=1,2\quad\text{and}\quad l,p,r,s=x,y,z.\end{aligned}\tag{4.10}$$

The displacement components $\bar{u}$ and $\bar{v}$ have been replaced by u_1 and u_2, in order to express the derivatives in a more convenient form.

Once computed the scalar components of the Hessian matrix, the eigenvalue problem is stated and the characteristic equation

$$\det\left(\mathbf{K}-\tau\mathbf{I}\right)=0\tag{4.11}$$

is solved. Being (4.11) a second degree polynomial equation, an equilibrium configuration $(\bar{u},\bar{v})$ is stable if both the eigenvalues $\tau_1(\bar{u},\bar{v})$ and $\tau_2(\bar{u},\bar{v})$ are positive.

4.4 Application to Mooney-Rivlin materials

The equilibrium equations are now specialized to the case of a compressible Mooney-Rivlin material. Consequently, numerical applications for the vertical and horizontal loading conditions are performed and the stability of the equilibrium paths is assessed.

The stored energy function for a compressible Mooney-Rivlin material is given by (2.50) and its derivatives are expressed by (2.51). The relation between longitudinal and transversal stretch is (2.52). By substituting equations (2.51) and (2.52) into (4.9), the following global equilibrium equations of the three-bar truss for the case of a compressible Mooney-Rivlin material are derived:

$$\begin{aligned}\hat{p}_\eta+\frac{2bh}{L}\left[Q_\alpha\left(B+\bar{u}\right)-Q_\beta\left(B-\bar{u}\right)+Q_\gamma\bar{u}\right]=0,\\ \hat{p}_\zeta+\frac{2bh}{L}\left[\left(Q_\alpha+Q_\beta\right)\left(H+\bar{v}\right)-Q_\gamma\left(L-\bar{v}\right)\right]=0,\end{aligned}\tag{4.12}$$

where

$$Q_\delta=\frac{\left(\bar{b}^2-\bar{c}+P_\delta\right)\left[2\bar{b}\left(\lambda_z^\delta\right)^2+\left(\lambda_z^\delta\right)^4\left(\bar{c}-P_\delta\right)+1\right]}{\left[\left(\lambda_z^\delta\right)^2\left(\bar{c}-P_\delta\right)+\bar{b}\right]^2},$$

$$P_\delta=\frac{4(2\bar{b}+\bar{c}+1)\left[\bar{c}\left(\lambda_z^\delta\right)^2+\bar{b}\right]^2}{\left(\lambda_z^\delta\right)^2\left\{-\sqrt{4(2\bar{b}+\bar{c}+1)\left[\bar{c}\left(\lambda_z^\delta\right)^2+\bar{b}\right]+\left[\bar{b}\left(\lambda_z^\delta\right)^2+1\right]^2}+\bar{b}\left(\lambda_z^\delta\right)^2+1\right\}^2},$$

with $\delta=\alpha,\beta,\gamma$ and $\hat{p}_\eta=p_\eta/a$, $\hat{p}_\zeta=p_\zeta/a$.

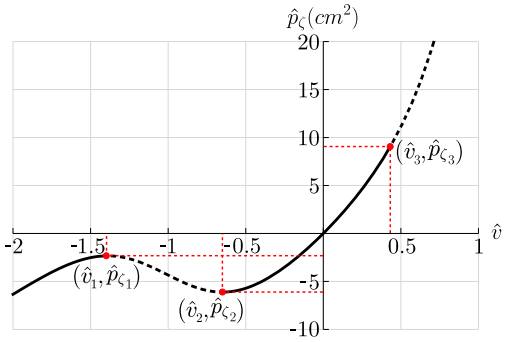

Figure 4.3: Primary branch of equilibrium for the case of vertical load and Mooney-Rivlin material (stable solutions: *continuous lines*, unstable solutions: *dashed lines*)

4.4.1 Vertical load

The first loading condition considered is the vertical load, which is expressed by $p_\eta = 0$ and $p_\zeta \neq 0$. The following numerical values are adopted for the geometry of the three-bar truss:

$$B = H = 10 \text{ cm}, \qquad b = h = 1 \text{ cm}.$$

In addition, the constitutive parameters are set as $\bar{b} = 1$ and $\bar{c} = 5$, as it was done in Section 2.5. The corresponding constitutive relation between longitudinal stretch and dimensionless external surface traction $\hat{f} = f/a$ is shown in Fig. 2.3. Note that Variations of $\bar{b}$ and $\bar{c}$ produce results that are quantitatively different, but from a qualitative point of view the global scenario remains unchanged. Finally, the dimensionless displacement components are introduced

$$\hat{u} = \frac{\bar{u}}{B}, \qquad \hat{v} = \frac{\bar{v}}{H}.$$

Hereinafter, the equilibrium solutions are represented using continuous lines to indicate stable configurations and dot lines to indicate unstable configurations. The stability is assessed as described in Section 4.3. Namely, the eigenvalues τ_1 and τ_2 are computed by solving equation (4.11). The sign of $\tau_1(\bar{u}, \bar{v})$ and $\tau_2(\bar{u}, \bar{v})$ determines whether the configuration $(\bar{u}, \bar{v})$ is stable or not.

The equilibrium equations (4.12) are firstly solved for $\bar{u} = 0$, obtaining the primary branch of equilibrium shown in Fig. 4.3, while the complete solutions of the equilibrium are represented in Fig. 4.4. The primary branch of the equilibrium configurations involves three critical points, as reported in Tab. 4.1. Another critical point can be found along asymmetric branches.

When the applied load is negative and the system reaches the first critical point, the loss of stability occurs as a snap-through phenomenon. Hence, an application of a small perturbation produces an abrupt transition of node C from configuration $(0, \hat{v}_2)$ to $(0, \hat{v}_1)$. At first glance, this behavior is quite unexpected. In fact, the presence of the bar γ subjected to a tensile load tends to ensure the stability of the system when the bars α and β are compressed. However, when the longitudinal stretch reaches relatively high values, the energy required to stretch a bar composed

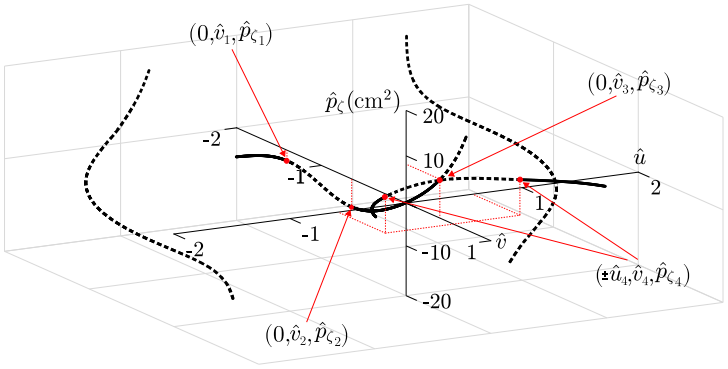

(a) Three-dimensional view ($\hat{u} = \bar{u}/B$, $\hat{v} = \bar{v}/H$ and $\hat{p}_\zeta = p_\zeta/a$)

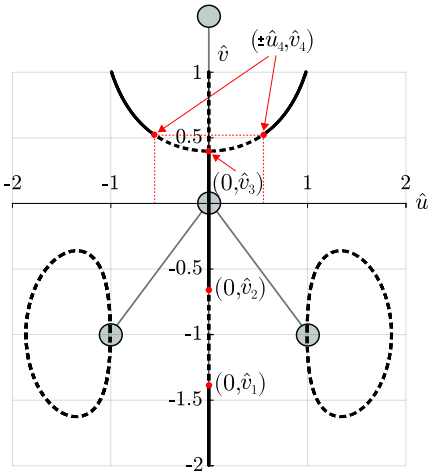

(b) Top view

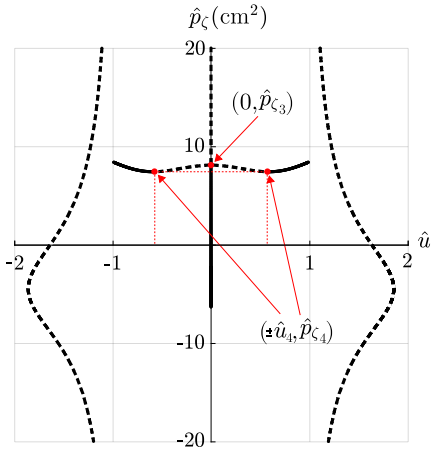

(c) Lateral view

Figure 4.4: Equilibrium paths of the three-bar truss subjected to a vertical load for the case of Mooney-Rivlin material (stable solutions: *continuous lines*, unstable solutions: *dashed lines*)

Table 4.1: Critical points for the three-bar truss subjected to a vertical load in case of Mooney-Rivlin material

Critical point	$\hat{u}$	$\hat{v}$	$\hat{p}_\zeta(\mathrm{cm}^2)$
1	0	-1.389	-2.332
2	0	-0.651	-6.111
3	0	0.396	8.076
4	$\pm$0.587	0.539	7.412

of a Mooney-Rivlin material is significantly less than the one required to compress it by the same amount (Fig. 2.3). Consequently, at some point the contribution of the bar γ is negligible and the three-bar truss undergoes a snap-through instability. Indeed, this behavior is commonly observed in the two-bar (or von Mises) truss [56].

Fig. 4.4 shows that, when the load is positive and the system reaches the configuration $(0, \hat{v}_3)$, the truss experiences a bifurcation instability. The primary branch is no longer stable and the central node jumps to one of the two asymmetric configurations $(\pm\hat{u}_4, \hat{v}_4)$. This behavior is again a consequence of the nonlinear constitutive law of the material. When the bar γ is compressed, the presence of the stretched bars α and β renders the system stable. Although, when their contribution becomes unimportant the stability is no more ensured and the system undergoes a bifurcation phenomenon.

It is interesting to observe that portions of the asymmetric equilibrium paths are stable, which means that they can be observed during laboratory tests. This does not happen without the contribution of the bar γ. In fact, in Section 2.5.1 it was demonstrated that, for the case of the von Mises truss subjected to a vertical load, asymmetric equilibrium solutions are always unstable (Fig. 2.10).

Other authors [6, 63] analyzed the three-bar in the case of vertical load. Moderately small deformations and a linear constitutive law were assumed. This leads to a single equilibrium path that is always stable, without showing snap-through or bifurcation phenomena. However, the hypothesis of linear elastic behavior is not suitable to describe the response of bodies subjected to large deformations. On the contrary, as demonstrated by the above application, the introduction of a nonlinear constitutive law provides a wider scenario of equilibrium solutions, involving unstable phenomena and asymmetric configurations. In Section 4.5, comparisons with the model employed in [6, 63] will be presented.

4.4.2 Horizontal load

The second loading condition considered is the horizontal load, which is expressed by $p_\eta \neq 0$ and $p_\varsigma = 0$. The same geometry and constitutive parameters of the previous application are assumed.

The results of the solution of the equilibrium equations (4.12) along with the stability analysis are represented in Fig. 4.5. In this case, the behavior of the system is extremely different from the case of the vertical load. In fact, a single stable primary path is found, while the other two branches are always unstable. Therefore, when a horizontal load is applied, the central node follows the primary branch without encountering any critical point. Fig. 4.5b shows that the projection of the primary branch on the $(\hat{u}, \hat{v})$ plane is not a horizontal line. This is due to the asymmetry of the truss with respect to the horizontal axis $\hat{u}$.

In conclusion, the system does not experience any unstable phenomenon and the only observable equilibrium path is given by the primary branch of equilibrium. Note that this relatively simple behavior may not be encountered if a more complex stored energy function is adopted.

It should be pointed out that the analysis has been limited to the range $\hat{u} \in$

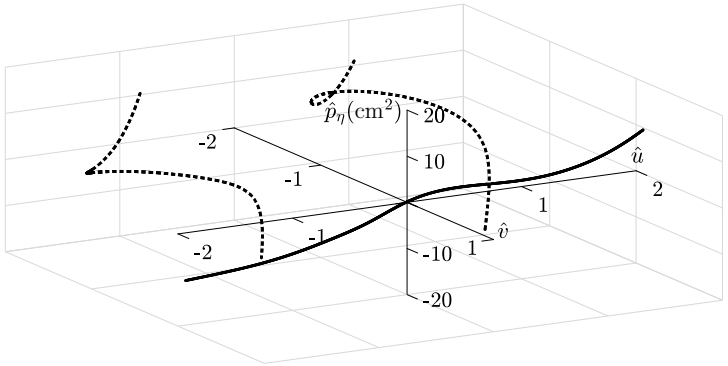

(a) Three-dimensional view ($\hat{u} = \bar{u}/B$, $\hat{v} = \bar{v}/H$ and $\hat{p}_\eta = p_\eta/a$)

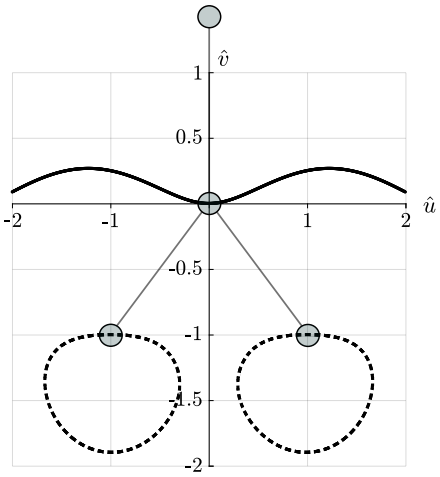

(b) Top view

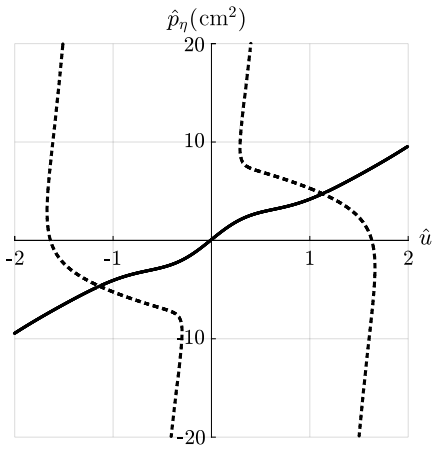

(c) Lateral view

Figure 4.5: Equilibrium paths of the three-bar truss subjected to a horizontal load for the case of Mooney-Rivlin material (stable solutions: *continuous lines*, unstable solutions: *dashed lines*)

$[-2,2]$ and $\hat{v} \in [-2,2]$. This because the remarkable features of the behavior of the three-bar truss with Mooney-Rivlin material are observed inside these ranges. It is straightforward to expand the results for wider ranges of $\hat{u}$ and $\hat{v}$, but from a physical point of view it is not of interest.

4.5 Comparison with other models

Also for the case of the three-bar truss it is interesting to provide a comparison between the equilibrium solutions derived in the present work and the ones obtained with other theories based on simplifying assumptions. In particular, Rezaiee-Pajand and Naghavi [6] used the formulation developed by Kwasniewski [1] to obtain an analytical solution of this problem for the vertical load case. It was found out that the presence of the upper bar renders the system always stable. In the present work, we found instead that adopting a nonlinear constitutive law for the material (Mooney-Rivlin law) a complex scenario of solutions arises, with a combination of snap-through and bifurcation instability.

The analytical formulation reported in [1] was already outlined in Section 2.6. The Green-Lagrange strain measure is adopted and the axial component of stress is expressed through a linear relation with the axial component of strain. The comparison between the constitutive laws assumed in the present work and in the simplified theories mentioned above is given in Fig. 2.13. The equilibrium equations of the three-bar truss obtained using the formulation of Kwasniewski [1] read

$$\begin{aligned} p_\eta \frac{2L^2}{bhE} - c_\alpha(l_\alpha^2 - L^2) + c_\beta(l_\beta^2 - L^2) - c_\gamma(l_\gamma^2 - L^2) = 0, \\ p_\zeta \frac{2L^2}{bhE} - s_\alpha(l_\alpha^2 - L^2) - s_\beta(l_\beta^2 - L^2) + s_\gamma(l_\gamma^2 - L^2) = 0. \end{aligned} \tag{4.13}$$

An application will be presented in the following. The geometry of the truss is the one reported in Section 2.5. The value of the elastic constant E is computed by introducing $\bar{c} = 5$ and $\bar{b} = 1$ into (2.74), which represents a correlation between the constitutive parameters of the Mooney-Rivlin material and the Young's modulus E.

4.5.1 Vertical load

The solution of the equilibrium equations (4.13) is represented in Fig. 4.6. For negative values of load $\hat{p}_\zeta$, the equilibrium is always stable. This result was expected because in this case the contribution of the bar γ, subjected to a tensile load, ensures the stability of the system when bars α and β are compressed. This happens because it is assumed that the bars behave following a linear elastic constitutive law. The contribution of bar γ is therefore not negligible and snap-through does not take place. However, assuming a nonlinear and more realistic constitutive law, snap-through is likely to be observed (see the application presented in Section 4.4.1).

For positive values of load $\hat{p}_\zeta$, the system reaches configuration $(0, \hat{v}_1)$ and the truss experiences a bifurcation instability. A secondary branch appears, showing stable asymmetric equilibrium solutions. When configuration $(0, \hat{v}_2)$ is reached, the

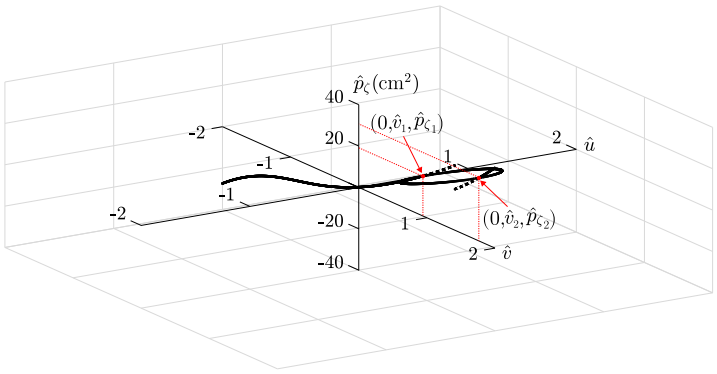

(a) Three-dimensional view ($\hat{u} = \bar{u}/B$, $\hat{v} = \bar{v}/H$ and $\hat{p}_\varsigma = p_\varsigma/a$)

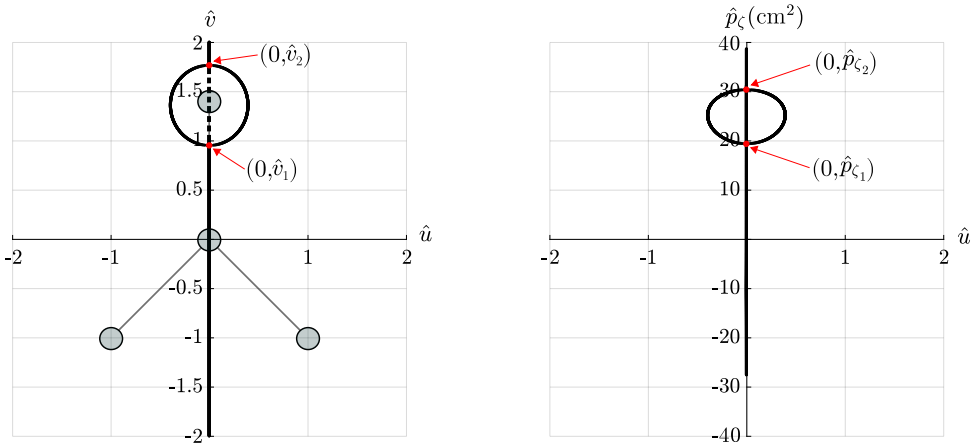

(b) Top view

(c) Lateral view

Figure 4.6: Equilibrium paths of the three-bar truss subjected to a vertical load for the case of linear elastic material [1] (stable solutions: *continuous lines*, unstable solutions: *dashed lines*)

Table 4.2: Critical points for the three-bar truss subjected to a vertical load in case of linear elastic constitutive law (Kwasniewski [1])

Critical point	$\hat{u}$	$\hat{v}$	$\hat{p}_\zeta(\mathrm{cm}^2)$
1	0	0.951	19.363
2	0	1.765	30.338

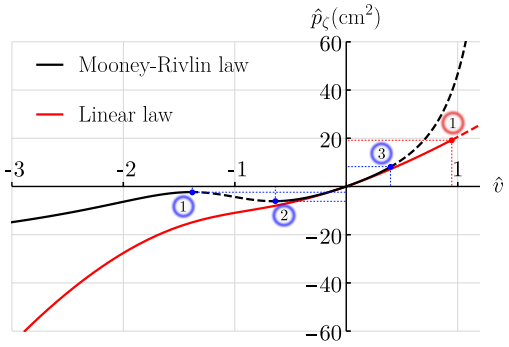

Figure 4.7: Comparison between the primary branch of equilibrium provided by the present theory (*Mooney-Rivlin law*) and the one provided by the formulation of Kwasniewski [1] (*Linear law*) for the three-bar truss subjected to a vertical load

solution becomes again unique and follows the primary branch of equilibrium. The critical points are listen in Tab. 4.2.

Fig. 4.7 shows a comparison between the primary branches of equilibrium of the fully nonlinear formulation with Mooney-Rivlin constitutive law and the formulation of Kwasniewski [1]. The two solutions correspond for low values of displacement $\hat{v}$, for which the deformation of the bars is still small. Due to differences in constitutive laws and strain measures, the solutions differ significantly for large values of $\hat{v}$. When load $\hat{p}_\zeta$ is negative, the solution obtained with a linear constitutive law is sensibly stiffer than the fully nonlinear one (Mooney-Rivlin law). This because, adopting a linear constitutive law, when bar γ is stretched its contribution is much higher than the case of a Mooney-Rivlin law. On the contrary, for positive values of load $\hat{p}_\zeta$, the fully nonlinear solution is stiffer because the contributions of compressed bars α and β are greater.

4.5.2 Horizontal load

The solution of the equilibrium equations (4.13) for the case of horizontal load is represented in Fig. 4.8. Only one branch of equilibrium is found. Instead, using the fully nonlinear theory also other solutions are found, but they are all unstable (Fig. 4.5).

From a qualitative point of view, there is not much difference between the two results. However, since the constitutive laws of the bars are different, the values of load applied in order to deform the truss are significantly different (Fig. 4.9).

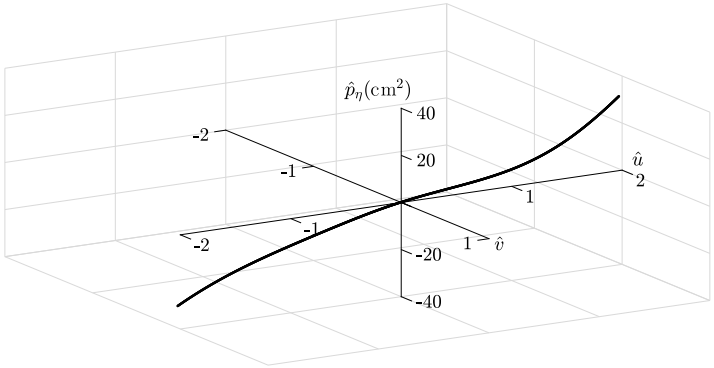

(a) Three-dimensional view ($\hat{u} = \bar{u}/B$, $\hat{v} = \bar{v}/H$ and $\hat{p}_\eta = p_\eta/a$)

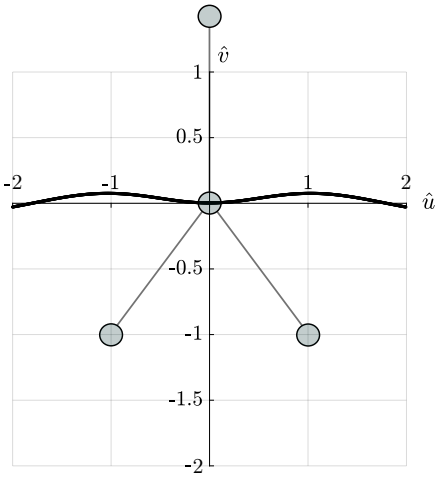

(b) Top view

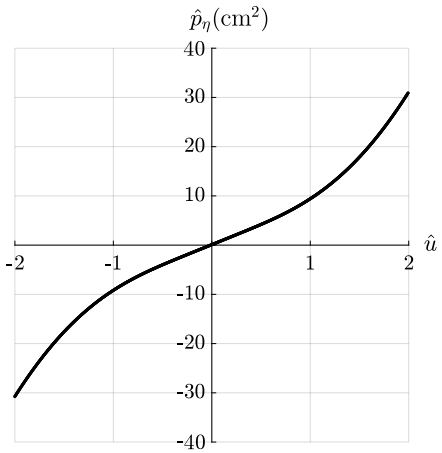

(c) Lateral view

Figure 4.8: Equilibrium paths of the three-bar truss subjected to a horizontal load for the case of linear elastic material [1] (stable solutions: *continuous lines*, unstable solutions: *dashed lines*)

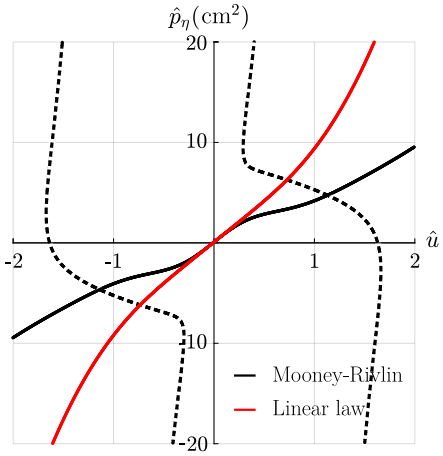

Figure 4.9: Comparison between the solutions provided by the present theory (*Mooney-Rivlin law*) and the formulation of Kwasniewski [1] (*Linear law*) for the three-bar truss subjected to a horizontal load

As in all the other cases, the equilibrium paths correspond for small deformations. For large deformations the solution obtained with the linear constitutive law is considerably stiffer. Again, this is due to the fact that the bars subjected to tension provide a higher contribution with respect to the case of Mooney-Rivlin constitutive law.

This last comparison with the results of other models found in the literature proved again the importance of the assumptions on the constitutive behavior of the material. A linear elastic law should not be employed in the nonlinear analysis of truss structures. The results obtained under this assumption are misleading and inconsistent.

4.6 Application to the crystal structure of graphene

In the present section, the nonlinear formulation proposed in this work is applied to the representative cell of the hexagonal nanostructure of graphene (Fig. 4.10). The carbon atoms are seen as material points (hinged nodes) and the chemical C-C bonds are simulated as the bars of the three-bar truss. The link between the real atomic structure and the elastic truss structure is established by incorporating a proper interatomic potential into the constitutive law of the bars [68].

Both vertical and horizontal load cases are analyzed. Note that, as shown in Fig. 4.10, the vertical load corresponds to a load applied along the direction of the armchair configuration, while the horizontal load corresponds to a load applied along the direction of the zigzag configuration.

As already mentioned, this application is not intended to give an accurate description of the mechanical properties of graphene, which will be instead analyzed

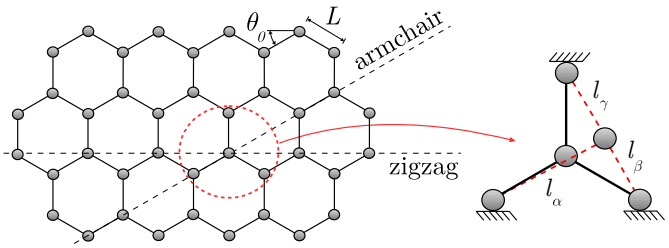

Figure 4.10: Graphene lattice geometry and three-bar truss as representative cell

in the next chapter. In this case we will consider only the direct (covalent) bonds between carbon atoms, without taking into account angular and long range interactions. Another limit of this application is that the external nodes are fixed. Therefore, the interaction with adjacent cells inside the graphene haxagonal lattice is not envisaged.

The goal of the present application is mainly to give an idea of the influence of the constitutive behavior of the bars on the global response of the structure. In fact, the highly nonlinear potential employed for the covalent bonds leads to a very complex scenario of solutions and unstable phenomena.

4.6.1 Interatomic potential, equilibrium equations and stability

Many functions for the interatomic potential describing the C-C bond can be found in literature. Most of the works regarding the simulation of the mechanical properties of graphene are based on the Tersoff-Brenner interatomic potential [69, 70], which has a complex analytical form and a significant number of parameters.

Genoese et al. [71] pointed out that, using the Tersoff-Brenner potential, the values of Young's modulus and Poisson's ratio obtained through advanced homogenization approaches (around 0.7 TPa and 0.4, respectively) are less accurate than those provided by the standard Cauchy-Born rule [72–79] (around 1 TPa and 0.16, respectively). This fact indicates that such potential requires a not straightforward reparametrization. Instead, the modified Morse potential [80] has a relatively simple form and it involves a limited number of parameters, allowing a simple adjustment on the basis of the results given by atomistic simulations. In light of this, Genoese et al. [71] proposed a new set of values for the parameters of the modified Morse potential, which is considered for this application. It has to be said that many works in literature (see, e.g, [81–86]) showed that, when the Morse potential is employed, the prediction of the mechanical properties of graphene is consistent with the results of ab-initio and molecular dynamics simulations.

The modified Morse potential is expressed as a function of the relative position of the carbon atoms

$$V(\Delta L) = D_e \left[\left(1 - e^{-\kappa \Delta L} \right)^2 - 1 \right], \tag{4.14}$$

where $\Delta L = l - L$ is the bond length variation, with l and $L = 0.142$ nm that indicate

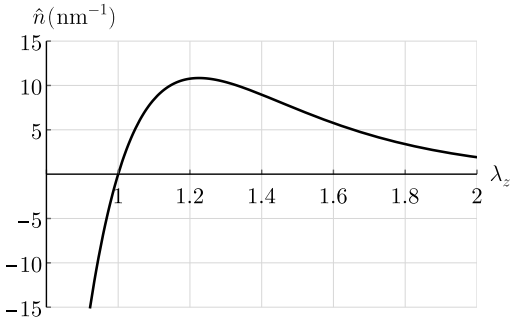

Figure 4.11: Constitutive behavior of the bar in case of Modified Morse potential, represented as normalized axial force $\hat{n} = n/D_e$ vs. longitudinal stretch λ_z

deformed and undeformed bond lengths, respectively. Genoese et al. [71] proposed the values $D_e = 7.90 \times 10^{10}$ N nm and $\kappa = 21.67$ nm^{-1}, which are considered in the present work. The following relation between bond length variation and longitudinal stretch holds:

$$\Delta L = L\,(\lambda_z - 1)\,.$$

The modified Morse potential (4.14) can be thus expressed as a function that depends solely on the longitudinal stretch λ_z. Thereby, the dimensionless stored energy function of the δ-th bar of the three-element truss becomes

$$\overline{\omega}_\delta\left(\lambda_z^\delta\right) = \frac{V\left(\lambda_z^\delta\right)}{D_e} = \left[1 - e^{-\kappa L\left(\lambda_z^\delta - 1\right)}\right]^2 - 1. \tag{4.15}$$

From now on, the lengths of the bars of the three-bar truss in deformed configuration are indicated as l_δ, with $\delta = \alpha, \beta, \gamma$.

The normalized axial force acting on the δ-th bar is determined as

$$\hat{n}_\delta = \frac{d\overline{\omega}_\delta}{d(\Delta L_\delta)} = \frac{d\overline{\omega}_\delta}{d\lambda_z^\delta}\frac{d\lambda_z^\delta}{d(\Delta L_\delta)} = 2\kappa e^{-\kappa L\left(\lambda_z^\delta - 1\right)}\left[1 - e^{-\kappa L\left(\lambda_z^\delta - 1\right)}\right], \quad \delta = \alpha, \beta, \gamma. \tag{4.16}$$

Fig. 4.11 shows the constitutive law resulting from the adoption of the modified Morse potential. Note that the derivation of equation (4.16) is much simpler than what has been done in Section 4.3. This because the elastic stored energy is now a function of the longitudinal stretch only, while in the general theory of three-dimensional bodies the transversal stretches are also involved. It is also noted that the modified Morse potential does not meet the requirement of isotropy, which is necessary for the validity of the constitutive equation (2.10). However, this does not raise any problem, since relation (4.16) is derived independently from equation (2.10).

The equilibrium equations of the representative cell are obtained by substituting

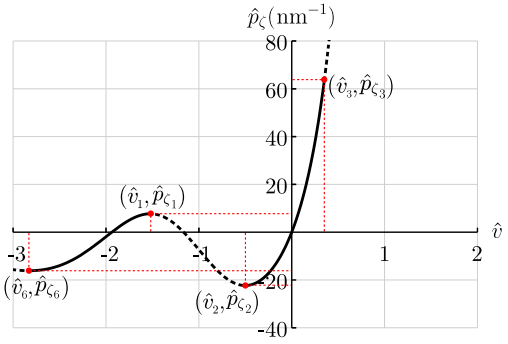

Figure 4.12: Application to the graphene representative cell: primary branch of equilibrium for the vertical load case (stable solutions: *continuous lines*, unstable solutions: *dashed lines*)

(4.16) into (4.3)

$$\begin{aligned}
&\hat{p}_\eta + 2\kappa e^{-\kappa L\left(\lambda_z^\delta - 1\right)}\left[1 - e^{-\kappa L\left(\lambda_z^\delta - 1\right)}\right](-c_\alpha + c_\beta - c_\gamma) = 0,\\
&\hat{p}_\zeta + 2\kappa e^{-\kappa L\left(\lambda_z^\delta - 1\right)}\left[1 - e^{-\kappa L\left(\lambda_z^\delta - 1\right)}\right](-s_\alpha - s_\beta + s_\gamma) = 0,
\end{aligned} \tag{4.17}$$

where $\hat{p}_\eta = p_\eta/D_e$, $\hat{p}_\zeta = p_\zeta/D_e$ and the kinematic quantities c_δ and s_δ, with $\delta = \alpha, \beta, \gamma$, are given by (4.4).

The stability of the equilibrium solutions is assessed through the energy criterion, as described in Section 4.3. However, in the modified Morse potential there is no dependence on the transversal stretches. Thus, equation (4.10) assumes the simplified form

$$\frac{\partial^2 \overline{\Pi}}{\partial u_j \partial u_i} = \sum_\delta \frac{\partial^2 \overline{\omega}_\delta}{\partial \left(\lambda_z^\delta\right)^2} \frac{\partial \lambda_z^\delta}{\partial u_j} \frac{\partial \lambda_z^\delta}{\partial u_i} + \sum_\delta \frac{\partial \overline{\omega}_\delta}{\partial \lambda_z^\delta} \frac{\partial^2 \lambda_z^\delta}{\partial u_j \partial u_i}, \quad \delta = \alpha, \beta, \gamma \quad \text{and} \quad i, j = 1, 2, \tag{4.18}$$

where $\overline{\Pi} = \frac{\Pi}{D_e}$ and the displacement components $\bar{u}$ and $\bar{v}$ have been replaced by u_1 and u_2 for the sake of clarity. The longitudinal stretch λ_z^δ, the dimensionless stored energy function $\overline{\omega}_\delta$ and their derivatives can be easily computed using (4.2) and (4.15). Note that the crystal structure of graphene is composed of regular hexagons, therefore

$$\theta_0 = \frac{\pi}{6}, \quad B = \frac{\sqrt{3}}{2} L = 0.123 \text{ nm}, \quad H = \frac{L}{2} = 0.071 \text{ nm}.$$

4.6.2 Vertical load

The equilibrium equations (4.17) are solved for the vertical load case, namely $p_\eta = 0$ and $p_\zeta \neq 0$. As already pointed out, this particular case corresponds to the application of a load along the direction of the armchair configuration. The stability analysis is performed using (4.18). Fig. 4.12 shows the primary branch of equilibrium, while the complete equilibrium paths are represented in Fig. 4.13. Tab. 4.3 lists the critical points resulting from the stability analysis.

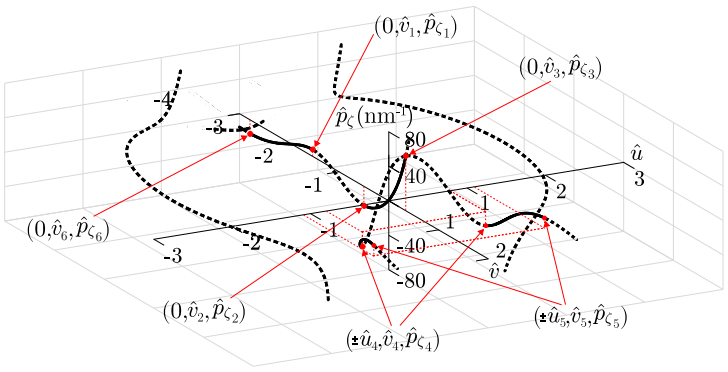

(a) Three-dimensional view ($\hat{u} = \bar{u}/B$, $\hat{v} = \bar{v}/H$ and $\hat{p}_\zeta = p_\zeta/D_e$)

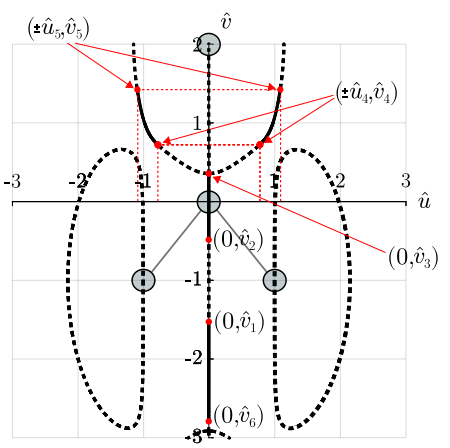

(b) Top view

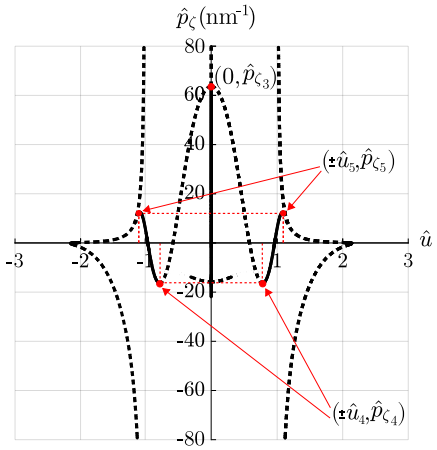

(c) Lateral view

Figure 4.13: Application to the graphene representative cell: equilibrium solutions for the vertical load case (stable solutions: *continuous lines*, unstable solutions: *dashed lines*)

Table 4.3: Application to the graphene representative cell: critical points of the equilibrium paths for the vertical load case

Critical point	$\hat{u}$	$\hat{v}$	$\hat{p}_\zeta(\mathrm{nm}^{-1})$
1	0	-1.524	7.696
2	0	-0.501	-22.321
3	0	0.351	63.410
4	$\pm$0.785	0.724	-16.530
5	$\pm$1.090	1.416	11.923
6	0	-2.829	-16.128

Qualitatively, the behavior of the system is similar to the one of Mooney-Rivlin materials, analyzed in Section 4.4.1. For negative values of the load, the primary branch is stable until the central node reaches the configuration $(0, \hat{v}_2)$. In this circumstance, a snap-through instability occurs and the node jumps to the configuration $(0, \hat{v}_1)$. Differently from the case of Mooney-Rivlin materials, the system presents another unstable phenomenon when the configuration $(0, \hat{v}_6)$ is reached. More precisely, as revealed by Fig. 4.13b, the equilibrium solutions become unstable and a bifurcation of the primary branch takes place.

Note that the critical point 6 is defined by $\hat{v}_6 = -2.829$, which means that this behavior occurs at a very large elongation of the bars. It is reasonable to consider that what happens outside the regions $\hat{u} \in [-3, 3]$ and $\hat{v} \in [-3, 2]$ is not relevant. In addition, it is difficult to conceive that such a scenario would take place when the representative cell is introduced in the hexagonal lattice of a graphene sheet. In view of the above, it is wise to treat this result with suspicion.

For positive loads, the equilibrium follows the primary branch until the critical point 3, where a bifurcation occurs and the truss assumes one of the two asymmetric configurations $(\pm\hat{u}_4, \hat{v}_4)$. Subsequently, the equilibrium remains stable until the system attains one of the critical points $(\pm\hat{u}_5, \hat{v}_5)$. Hence, for a moderate deformation of the bars (representing the bonds between carbon atoms) the response of the representative cell of a graphene sheet is symmetric, while for large a deformation $(\hat{v} > \hat{v}_3)$ the system is capable of assuming an asymmetric equilibrium configuration. This information could be useful to explain and predict the behavior of a graphene sheet when subjected to large deformations. Further comments on the results of this application are presented in Section 4.6.4, giving qualitative comparisons with other works.

It is worthwhile to notice that inside the region analyzed there are three stable self-equilibrated configurations, as displayed in Figs. 4.12 and 4.13c. In such configurations, the equilibrium takes place in absence of applied loads. By solving the equilibrium equations (4.17) with $p_\eta = 0$ and $p_\zeta = 0$ and considering only the stable solutions, the three self-equilibrated points $(0, -1.937)$ and $(\pm 0.969, 0.969)$ are detected.

4.6.3 Horizontal load

In this last case, equations (4.17) governing the equilibrium are solved with $p_\zeta = 0$, which corresponds to the application of a load along the zigzag configuration. The solutions are shown in Fig. 4.14 and the critical points resulting from the stability analysis are listed in Tab. 4.4.

Unlike the case of Mooney-Rivlin materials reported in Section 4.4.2, the system exhibits a rich variety of behaviors. The strongly nonlinear constitutive law deriving from the modified Morse potential leads to a very complex scenario of equilibrium solutions, composed of a primary and a secondary branch of equilibrium. Both of them include stable and unstable solutions.

As clearly visible in Fig. 4.14b, starting from the undeformed configuration, the central node follows an inclined direction along which the total potential en-

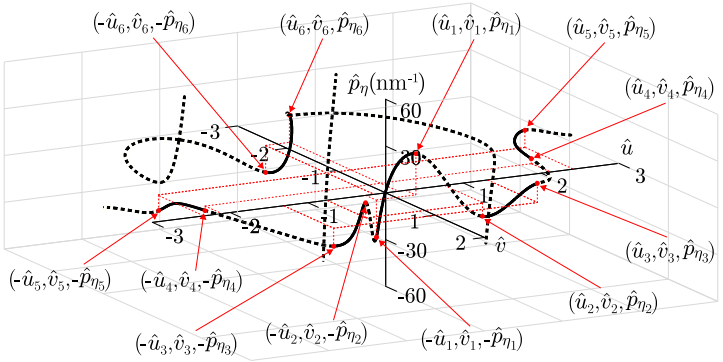

(a) Three-dimensional view ($\hat{u} = \bar{u}/B$, $\hat{v} = \bar{v}/H$ and $\hat{p}_\eta = p_\eta/D_e$)

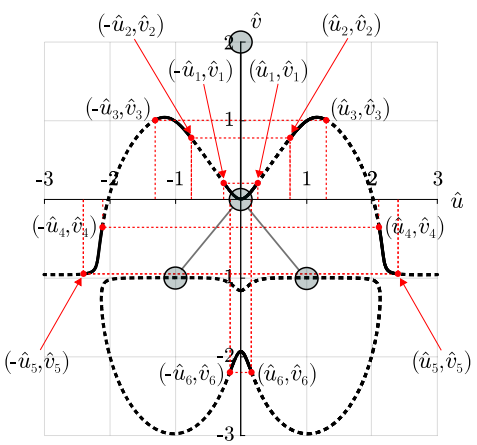

(b) Top view

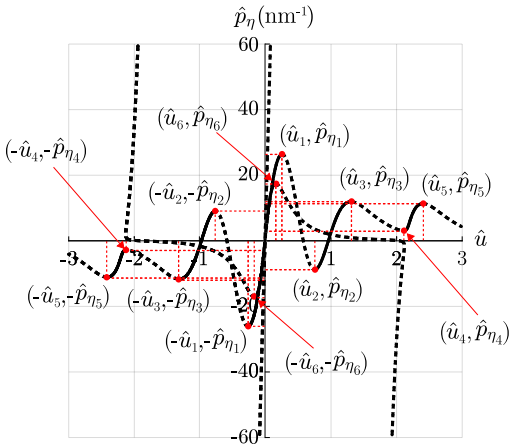

(c) Lateral view

Figure 4.14: Application to the graphene representative cell: equilibrium solutions for the horizontal load case (stable solutions: *continuous lines*, unstable solutions: *dashed lines*)

Table 4.4: Application to the graphene representative cell: critical points of the equilibrium paths for the horizontal load case

Critical point	$\hat{u}$	$\hat{v}$	$\hat{p}_\eta(\text{nm}^{-1})$
1	$\pm$0.259	0.205	$\pm$26.261
2	$\pm$0.760	0.779	$\pm$8.949
3	$\pm$1.310	1.001	$\pm$11.798
4	$\pm$2.112	-0.360	$\pm$2.930
5	$\pm$2.409	-0.954	$\pm$11.229
6	$\pm$0.162	-2.204	$\pm$17.296

ergy is minimum. The equilibrium turns then unstable and a sudden transition from $(\pm\hat{u}_1, \hat{v}_1)$ to $(\pm\hat{u}_2, \hat{v}_2)$ takes place. This unexpected behavior occurs because the contribution of the stretched bars α and β becomes irrelevant with respect to the compressed bar γ and their effect on the stability of the truss vanishes. This consideration is made clear by looking at the constitutive law of the bars, shown in Fig. 4.11. For large longitudinal deformations, the energy required to compress a bar (i.e. to bring the carbon atoms closer to each other) is much higher than the one required to stretch the bar by the same amount. The same happens for Mooney-Rivlin materials, as pointed out in Section 4.4.1. However, in the case of the modified Morse potential this phenomenon is more pronounced and leads to unusual results. In fact, when the longitudinal stretch approaches the value 2, the bond between carbon atoms is almost broken and the energy needed to keep stretching the bond is very low. Instead, the bar composed of a Mooney-Rivlin material preserves a significant stiffness also for higher values of the longitudinal stretch.

Another instability of the same kind occurs along the primary branch when the node reaches one of the positions $(\pm\hat{u}_3, \hat{v}_3)$. Consequently, the equilibrium solutions are unstable until $(\pm\hat{u}_4, \hat{v}_4)$. Then, when one of the configurations $(\pm\hat{u}_5, \hat{v}_5)$ is achieved, the equilibrium turns again unstable.

It goes without saying that the most interesting part of the solutions obtained is the one close to the origin, where the deformation is still contained. It gives a qualitative idea of the directions of minimum energy, along which a graphene sheet could deform when subjected to horizontal loads. Instead, the subsequent intricate behavior along the primary branch allows concluding that the post-critical response of the representative cell of the hexagonal lattice is not exhausted by the usual unstable phenomena affecting truss structures. Further comments are reported in the next section.

The stable self-equilibrated configurations are obviously the same as the ones detected in the vertical load case (Section 4.6.2), because both self-equilibrated configurations and stability analysis do not depend on the applied load. In particular, the secondary branch starts from the configuration $(0, -1.937)$, which occurs in absence of applied loads. A single stable region is found until the positions $(\pm\hat{u}_6, \hat{v}_6)$ are reached. The other configurations along the secondary branch are not experienced by the system.

4.6.4 Further considerations

This modest application showed the influence of the potential adopted for the constitutive law of the bars. As observed, the behavior of the truss changed completely for both vertical and horizontal load cases. Moreover, the application gave some insights into the mechanical behavior of the representative cell of a graphene sheet subjected to applied loads, which is rather complex. It goes without saying that the results here presented are not representative of the behavior of the entire structure of a graphene sheet. However, the following general considerations can be made:

(i) as observed by other authors, for infinitesimal in-plane deformations graphene behaves as an orthotropic material (often referred as nearly isotropic). For

instance, Ni et al. [87] performed molecular dynamics simulations on a square-shaped graphene sheet, computing an average Young's modulus of 1.13 TPa and 1.05 TPa along armchair and zigzag directions, respectively. Gao and Hao [88] used quantum mechanics and quantum molecular dynamics approaches obtaining similar results in terms of elastic properties. Xu et al. [89] applied the density functional theory on zigzag and armchair graphene sheets, confirming that for small uniaxial deformations graphene is nearly isotropic. However, all the aforementioned studies agree on the fact that, when the in-plane deformation gets large, graphene becomes highly anisotropic. From the results obtained in the present application, it can be clearly noticed that for finite deformations the behavior in the armchair and zigzag configurations are extremely different, which reflects the anisotropy of the system. On the other hand, by looking at Figs. 4.12 and 4.14c, one can infer that for small deformations the stiffness of armchair and zigzag configurations is similar, which agrees with what has been said above;

(ii) Lu and Huang [90] and Singh and Patel [91] modeled the graphene sheet as an equivalent continuum, considering the Tersoff-Brenner potential and a plane stress condition for the derivation of the elastic in-plane properties. The tangent stiffness coefficients under finite extensional in-plane deformations were computed and it was shown that the material displays a softening behavior for finite deformations. Consistently, looking at Figs. 4.12 and 4.14c, it can be noticed that also in the present application the system tends to possess a softening behavior. The only exception takes place for the vertical load case, when the central atom C gets closer to the upper atom 3 (see Fig. 4.12). In this circumstance, the strong compressive stiffness of the C-C bond leads to a hardening behavior. However, this case would represent a contraction of the graphene sheet, which is not in the interest of this discussion;

(iii) it is widely known that for noncentrosymmetric crystals a continuum model must account for the discrete nature of the atomic structure inside the cells. While the deformation is homogeneous at the representative cell level, the single atoms do not follow the same rule, otherwise the internal equilibrium would not be satisfied [68]. Several authors [92–94] accounted for this effect by introducing an internal lattice relaxation and maintaining a homogeneous deformation at the macroscopic scale. Instead, the application presented in this work is based on a discrete formulation and it includes the analysis of the stability of the equilibrium configurations assumed by the atoms. As previously observed, for both vertical load (Fig. 4.13a) and horizontal load (Fig. 4.14a) cases the critical points are manifold. Thus, while the deformation of a hypothetical continuum cell proceeds, such internal unstable phenomena occur, affecting the macroscopic behavior of the material.

The above considerations are solely intended to provide an overall idea of the complex mechanical phenomena taking place within a graphene sheet and to highlight some possible issues that are worthy of consideration. The analysis of the

stability of the equilibrium configurations assumed by the atoms showed that internal unstable phenomena may take place for both vertical and horizontal load cases. Their implications on the global response of a graphene sheet should be accounted for in mechanical models.

Some interesting comments were made after having observed the results of this application. However, given the limitations of the application, only qualitative considerations about the behavior of graphene can be draw. In the next chapter, an accurate nonlinear model for the in-plane mechanical behavior of graphene will be presented.

Chapter 5

A nonlinear molecular mechanics model for graphene subjected to large in-plane deformations

The formulation for three-dimensional bodies subjected to uniaxial tractions in finite elasticity was applied to investigate equilibrium and stability of the three-bar truss. An application by assuming geometry and interatomic potential of graphene was presented in Section 4.6. The limitations of the application are: long range and angular interactions are neglected; the influence of adjacent cells is not taken into account because the external nodes are fixed. In this chapter, the truss model is extended by introducing elements that allows to give an accurate description of the mechanics of graphene [95, 96].

5.1 Graphene and molecular mechanics approach

Graphene attracted a lot of interest due to its excellent mechanical, thermal and electrical properties [97–102]. Indeed, numerous applications can be found in different research fields. For instance, graphene is used for micro-and nano-electronic devices [103–107], energy generation and storage [108, 109], biomedicine [110] and composite materials [111–116]. Graphene nanocomposites had a great impact on new technologies [117] because a small amount of graphene produces a significant enhancement of the mechanical properties. Rafiee et al. [118] reported that, in case of epoxy matrix, the Young's modulus increased by 31% just by adding 0.1 wt% of graphene and the tensile strength was enhanced by 40%. Fang et al. [119] added 0.9 wt% of graphene in polystyrene sheets, obtaining an increase of 57.2% in Young's modulus. These examples give an idea of the capabilities of this material for advanced engineering applications.

The potentialities of graphene can be fully exploited only with a deep understanding of its mechanical behavior. To this regard, few experimental tests were

carried out [64, 120–122]. The lack of experimental results is due to the technical difficulties connected to the extremely small scale of the problem. Reliable models for the simulation of the mechanical behavior of graphene are thus necessary.

The modeling techniques can be distinguished mainly in three categories: atomistic, equivalent continuum and molecular mechanics. Atomistic simulations, such as molecular dynamics (MD) and *ab initio*, are the most physically accurate. However, they require a large computational effort, which makes them suitable only for systems with a small number of atoms. Continuum models are based on the assumption that the discrete nature of the lattice structure can be neglected by viewing the system as a continuum medium [123]. For instance, the mechanical properties of CNTs were investigated by using the theory of continuum shells in [124–128]. Although continuum modeling is the simplest approach, some parameters such as the effective thickness of CNTs (or graphene) are not well established in continuum mechanics. Yakobson et al. [129] fitted the results of a MD simulation with the ones of a continuum shell model and estimated an effective thickness of 0.066 nm. Odegard et al. [130] developed a truss model and proposed a thickness of around 0.65 nm, while Zhou et al. [131] proposed a value of 0.71 nm. In addition to this issue, it is still not clear how to properly incorporate size effects into an equivalent continuum model.

Molecular mechanics formulations are probably the best compromise for the modeling of nanostructures. In this case, the atoms of the lattice structure are viewed as nodes connected by continuum elements, whose properties are determined through an energy equivalence with the interatomic potential of the chemical bonds [132–136]. Of particular importance was the idea of Chang and Gao [137], who developed the stick-and-spring model. Stick elements represent the covalent C-C bonds and spring elements account for bond angle variations. The constitutive behavior of sticks and springs is often described by harmonic potentials and the elastic constants of graphene in linear elasticity are evaluated under the assumption of small displacements and deformations [137–140]. However, it is widely known that, graphene can experience large values of strain prior to failure. In light of this, an accurate analysis of the mechanical behavior of graphene should account for large deformations and material nonlinearities.

Some recent formulations assume nonlinear constitutive behaviors for both sticks and springs by adopting proper interatomic potentials [141, 142]. This approach allows to investigate the response of graphene when subjected to large in-plane deformations. Nevertheless, significantly different results can be found in the literature even for the simplest case of pristine graphene. This indicates that there are still challenges that need to be addressed in order to establish reliable approaches.

In this chapter we present a fully nonlinear stick-and-spring model for graphene subjected to large in-plane deformations. Geometric nonlinearity is accounted for by writing the equilibrium of the graphene representative cell in deformed configuration, where the displacements of the nodes are assumed to be large. Material nonlinearity is introduced by adopting the modified Morse potential for the sticks and a nonlinear bond angle potential for the springs. The equilibrium equations are solved in the cases of uniaxial tensile load along zigzag and armchair directions. The case of equibiaxial load is also analyzed, which is an important test for the character-

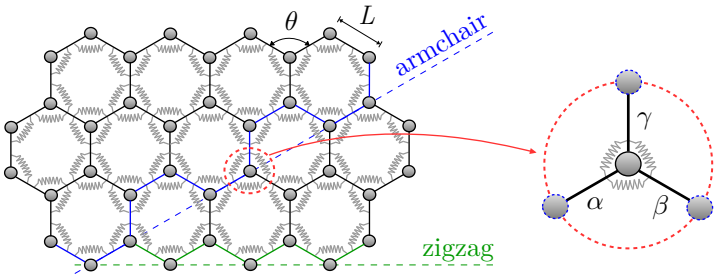

Figure 5.1: Graphene sheet regarded as a stick-and-spring system and representative cell obtained by placing fictitious atoms at the midpoints of the sticks

ization of graphene that have been scarcely investigated [143]. The stability of the equilibrium configurations is assessed using an energy criterion. The discrete results obtained from the stick-and-spring approach are homogenized in order to provide a comparison with previous results in the literature, which are often given in terms of engineering stress and strain.

In the following, basic assumptions and interatomic potentials for the representative cell of the graphene sheet are described. Consequently, kinematics and equilibrium of the stick-and-spring model are discussed. The equilibrium equations are solved in the cases of uniaxial tensile load along zigzag and armchair directions and in the case of equibiaxial tensile load. The stability of the equilibrium configurations is assessed and the results are presented and discussed. Comparisons with other works in the literature are also given. Finally, we present the linearization of the nonlinear formulation of the equilibrium, which is derived by assuming that the displacements of the nodes (atoms) are small. By doing so, the analytical expressions of Young's modulus and Poisson's ratio are obtained.

5.2 Preliminaries

The carbon atoms are regarded as hinged nodes of the planar hexagonal lattice of Fig. 5.1. The reference configuration is stress-free and the atoms can only move in the lattice plane. The undeformed bond length is $L = 0.142$ nm and, since the crystal structure of graphene is composed of regular hexagons, the undeformed bond angle is $\theta = 2\pi/3$.

The interaction between two adjacent carbon atoms is modeled through elastic stick elements. It is natural to consider that the C-C bond always remains straight regardless of the applied load, therefore we assume that each stick has infinite bending and shear stiffness. In addition, in order to account for the bond angle bending energy, rotational spring elements are incorporated into the model (Fig. 5.1). The link between real atomic structure and stick-and-spring model is established by using proper interatomic potentials for the constitutive laws of sticks and springs.

5.2.1 Interatomic potentials

The interatomic potential should account for both short and long range interactions between atoms. Long range interactions are less significant and thus usually neglected in molecular mechanics models [84, 130, 137]. In addition, given the assumption of plane problem, only the contributions of bond length and angular variations are considered in this work. Hence, in its general formula, the molecular potential energy is written as

$$V = \sum V_r + \sum V_\theta,$$

where V_r and V_θ are the terms related to bond length and bond angle variations, respectively.

As reported in Section 4.6.1, many works in literature showed that the modified Morse potential provides reliable predictions of the mechanical properties of graphene. Therefore, the modified Morse potential, expressed by (4.14), is assumed for the sticks. For reasons of convenience, its expression is given again in the following:

$$V(\Delta L) = D_e \left[\left(1 - e^{-\kappa \Delta L} \right)^2 - 1 \right], \tag{5.1}$$

with parametrization $D_e = 7.90 \times 10^{-10}$ N nm and $\kappa = 21.67$ nm^{-1}, as discussed in Section 4.6.1. Here we indicate the deformed length of the covalent bond with L', thus the length variation is $\Delta L = L' - L$. The axial constitutive law of the sticks is obtained by deriving (5.1). Namely,

$$n = \frac{dV(\Delta L)}{d(\Delta L)} = 2 D_e \kappa e^{-\kappa \Delta L} \left(1 - e^{-\kappa \Delta L} \right),$$

in which n is the axial force acting on the stick.

According to Belytschko et al. [80], the bond angle energy is expressed as

$$V_\theta(\Delta\theta) = \frac{1}{2} k_\theta \Delta\theta^2 \left(1 + k_s \Delta\theta^4 \right),$$

where the bond angle variation $\Delta\theta$ is defined as $\Delta\theta = \theta' - \theta$, with θ' that indicates the bond angle in deformed configuration. We assume the bond angle rigidity $k_\theta = 1.42 \times 10^{-9}$ N nm rad^{-2}, which was derived by Chang and Gao [137] by fitting the elastic constants of a graphene sheet. In accordance with Belytschko et al. [80], the value of parameter k_s is 0.754 rad^{-4}. The nonlinear constitutive relation for the spring, which links bending moment and angle variation, is the following:

$$m = \frac{dV_\theta(\Delta\theta)}{d(\Delta\theta)} = k_\theta \Delta\theta \left(1 + 3 k_s \Delta\theta^4 \right), \tag{5.2}$$

where m is the bending moment acting on the spring.

5.2.2 Representative cell of the graphene sheet

The analysis is focused on the representative cell of Fig. 5.1, which is obtained by cutting the sticks at their midpoints, where fictitious atoms are placed. After the

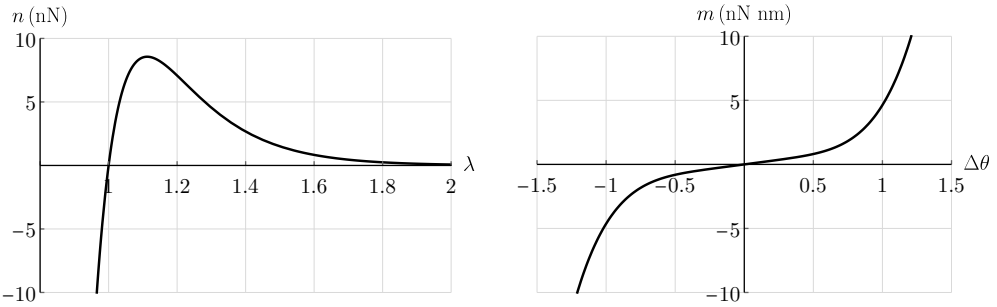

(a) Relation between axial force and longitudinal stretch for the sticks

(b) Relation between bending moment and bond angle variation for the springs

Figure 5.2: Constitutive behavior of the elements of the stick-and-spring model

deformation, sticks α, β and γ are subjected to a length variation that is half the length variation of the whole stick. Therefore, their potential is adjusted as

$$V(\Delta L_i) = \frac{1}{2} D_e \left[\left(1 - e^{-2\kappa \Delta L_i} \right)^2 - 1 \right], \quad i = \alpha, \beta, \gamma,$$

from which

$$n_i = 2 D_e \kappa e^{-2\kappa \Delta L_i} \left(1 - e^{-2\kappa \Delta L_i} \right), \quad i = \alpha, \beta, \gamma. \tag{5.3}$$

In this way it is ensured that the force acting on each stick of the representative cell is the same as the one that arises on the whole stick, viewed in the context of a graphene sheet. Constitutive equation (5.3) can be written as

$$n_i = 2 D_e \kappa e^{-2\kappa L_i (\lambda_i - 1)} \left[1 - e^{-2\kappa L_i (\lambda_i - 1)} \right], \quad i = \alpha, \beta, \gamma,$$

where $\lambda_i = L_i' / L_i$ is the stretch of the corresponding stick.

The bond angle variations of the representative cell are equal to the bond angle variations of the entire graphene sheet. Thus, no adjustment of the potential V_θ is required and the constitutive law of the springs is given by (5.2). Figs. 5.2a and 5.2b show the constitutive law of the sticks and the rotational springs, respectively.

5.3 The stick-and-spring model

In this section, kinematics and equilibrium equations of the representative cell are presented. Firstly, the equilibrium equations are written for the most general kinematics, displayed in Fig. 5.3a. The deformation of the representative cell involves two degrees of freedom for each of the nodes 1, 2, 3 and 4. In order to avoid rigid motions, the three degrees of freedom u_1, v_1 and u_2 are suppressed by introducing proper restraints.

This general formulation of the equilibrium allows investigating the response of graphene in the event that there are initial imperfections. For instance, this may

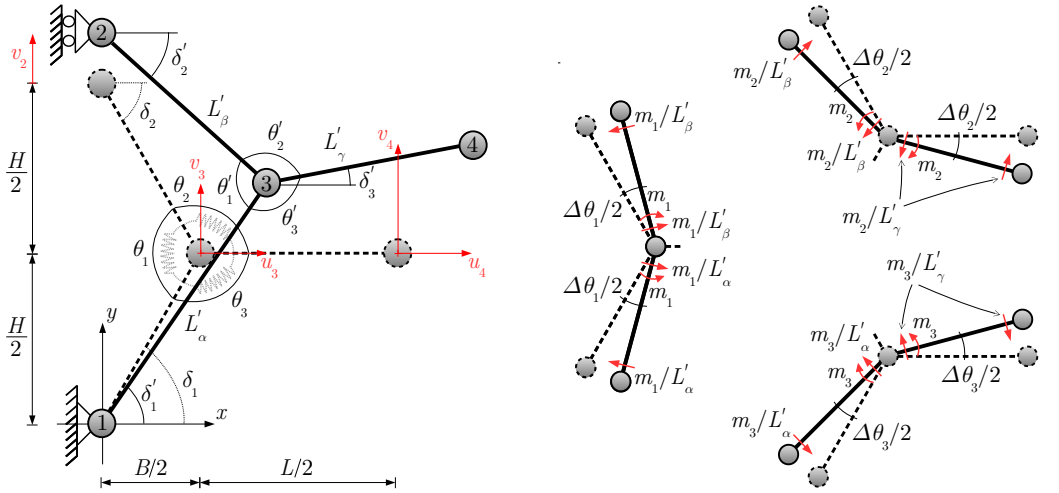

(a) Reference and deformed configurations. Each node has two degrees of freedom and restraints are introduced to avoid rigid motions

(b) Bending moments and shear forces that arise on the sticks due to bond angle variations

Figure 5.3: Analysis of the representative cell subjected to large in-plane deformations

be done by considering a non-zero initial value for a certain degree of freedom. The formulation can be also generalized for other lattice structures with different geometries.

In this paper we focus on the case of pristine graphene. Hence, in the second part of the present section, the general formulation is simplified by assuming that the system deforms maintaining its symmetry with respect to the horizontal axis through nodes 3 and 4. This appears to be the most reasonable assumption for the kinematics of the system in case that there are no initial imperfections.

5.3.1 Kinematics and equilibrium

The lengths of the sticks in reference configuration are

$$L_\alpha = \sqrt{(x_3 - x_1)^2 + (y_3 - y_1)^2}, \quad L_\beta = \sqrt{(x_3 - x_2)^2 + (y_3 - y_2)^2},$$
$$L_\gamma = \sqrt{(x_4 - x_3)^2 + (y_4 - y_3)^2},$$

while in deformed configuration

$$L'_\alpha = \sqrt{(x'_3 - x'_1)^2 + (y'_3 - y'_1)^2}, \quad L'_\beta = \sqrt{(x'_3 - x'_2)^2 + (y'_3 - y'_2)^2},$$
$$L'_\gamma = \sqrt{(x'_4 - x'_3)^2 + (y'_4 - y'_3)^2}, \tag{5.4}$$

where (x_j, y_j) and (x'_j, y'_j) are the coordinates of the nodes in reference and deformed configurations, respectively. The length variations are expressed as

$$\Delta L_i = L'_i - L_i, \quad i = \alpha, \beta, \gamma,$$

which provide

$$\begin{aligned}
\Delta L_\alpha &= \sqrt{\left(\frac{B}{2} + u_3\right)^2 + \left(\frac{H}{2} + v_3\right)^2} - \frac{L}{2}, \\
\Delta L_\beta &= \sqrt{\left(\frac{B}{2} + u_3\right)^2 + \left(\frac{H}{2} + v_2 - v_3\right)^2} - \frac{L}{2}, \\
\Delta L_\gamma &= \sqrt{\left(\frac{L}{2} - u_3 + u_4\right)^2 + (v_4 - v_3)^2} - \frac{L}{2},
\end{aligned}$$

where $B = L/2 = 0.071$ nm and $H = \sqrt{3}L/2 = 0.123$ nm.

As shown in Fig. 5.3a, the angles of the sticks with respect to axis x are δ_i and δ'_i in reference and deformed configurations, respectively. Underformed and deformed bond angles are indicated with θ_i and θ'_i. In reference configuration, $\delta_1 = \delta_2 = \pi/3$ and $\delta_3 = 0$, while $\theta_1 = \theta_2 = \theta_3 = 2\pi/3$. In such circumstance, the rotational springs do not produce bending moments on the sticks. In deformed configuration, angles δ_1, δ_2 and δ_3 become

$$\begin{aligned}
\delta'_1 &= \arctan\left(\frac{y'_3 - y'_1}{x'_3 - x'_1}\right) = \arctan\left(\frac{H + 2v_3}{B + 2u_3}\right), \\
\delta'_2 &= \arctan\left(\frac{y'_2 - y'_3}{x'_3 - x'_2}\right) = \arctan\left(\frac{H + 2v_2 - 2v_3}{B + 2u_3}\right), \\
\delta'_3 &= \arctan\left(\frac{y'_4 - y'_3}{x'_4 - x'_3}\right) = \arctan\left(\frac{2v_4 - 2v_3}{L - 2u_3 + 2u_4}\right),
\end{aligned}$$

and the bond angles are computed as

$$\theta'_1 = \delta'_1 + \delta'_2, \quad \theta'_2 = \pi - \delta'_2 - \delta'_3, \quad \theta'_3 = \pi - \delta'_1 + \delta'_3.$$

The bond angle variations are therefore obtained as follows:

$$\begin{aligned}
\Delta\theta_1 &= \theta'_1 - \theta_1 = \arctan\left(\frac{H + 2v_2 - 2v_3}{B + 2u_3}\right) + \arctan\left(\frac{H + 2v_3}{B + 2u_3}\right) - \frac{2}{3}\pi, \\
\Delta\theta_2 &= \theta'_2 - \theta_2 = -\arctan\left(\frac{H + 2v_2 - 2v_3}{B + 2u_3}\right) - \arctan\left(\frac{2v_4 - 2v_3}{L - 2u_3 + 2u_4}\right) + \frac{\pi}{3}, \\
\Delta\theta_3 &= \theta'_3 - \theta_3 = -\arctan\left(\frac{H + 2v_3}{B + 2u_3}\right) + \arctan\left(\frac{2v_4 - 2v_3}{L - 2u_3 + 2u_4}\right) + \frac{\pi}{3}.
\end{aligned} \tag{5.5}$$

The bond angle variations $\Delta\theta_i$ $(i = 1, 2, 3)$ produce the bending moments m_1, m_2 and m_3 acting on the corresponding sticks, according to the constitutive relation (5.2).

The loads are considered concentrated on the nodes and they reproduce the interactions with adjacent cells of the graphene sheet. The concentrated loads are

indicated with symbol p_{jk}, where $j = 1,2,3,4$ and $k = x,y$, denoting node and direction respectively. Note that loads p_{3x} and p_{3y} are equal to zero, because central node 3 does not have a direct interaction with other nodes outside the representative cell. Its interactions with nodes 1, 2 and 4 are represented by the internal actions (axial forces and bending moments) of sticks and springs.

In deformed configuration, axial forces n_α, n_β and n_γ arise on the sticks due to axial deformations. In addition, shear forces arise from the bending moments m_1, m_2 and m_3 generated by the springs due to bond angle variations (Fig. 5.3b). By combining the contributions of concentrated loads, axial forces and shear forces, the global equilibrium of the representative cell in deformed configuration reads

$$
\begin{aligned}
&\sum_i f^i_{1x} = n_\alpha c_1 - \frac{s_1}{L'_\alpha}(m_1 - m_3) + p_{1x} = 0,\\
&\sum_i f^i_{1y} = n_\alpha s_1 + \frac{c_1}{L'_\alpha}(m_1 - m_3) + p_{1y} = 0,\\
&\sum_i f^i_{2x} = n_\beta c_2 - \frac{s_2}{L'_\beta}(m_1 - m_2) + p_{2x} = 0,\\
&\sum_i f^i_{2y} = -n_\beta s_2 - \frac{c_2}{L'_\beta}(m_1 - m_2) + p_{2y} = 0,\\
&\sum_i f^i_{3x} = -n_\alpha c_1 - n_\beta c_2 + n_\gamma c_3 + m_1\left(\frac{s_1}{L'_\alpha} + \frac{s_2}{L'_\beta}\right) - m_2\left(\frac{s_2}{L'_\beta} + \frac{s_3}{L'_\gamma}\right) - m_3\left(\frac{s_1}{L'_\alpha} + \frac{s_3}{L'_\gamma}\right)\\
&\qquad = 0,\\
&\sum_i f^i_{3y} = -n_\alpha s_1 + n_\beta s_2 + n_\gamma s_3 - m_1\left(\frac{c_1}{L'_\alpha} - \frac{c_2}{L'_\beta}\right) - m_2\left(\frac{c_2}{L'_\beta} + \frac{c_3}{L'_\gamma}\right) + m_3\left(\frac{c_1}{L'_\alpha} + \frac{c_3}{L'_\gamma}\right)\\
&\qquad = 0,\\
&\sum_i f^i_{4x} = -n_\gamma c_3 + \frac{s_3}{L'_\gamma}(m_2 + m_3) + p_{4x} = 0,\\
&\sum_i f^i_{4y} = -n_\gamma s_3 + \frac{c_3}{L'_\gamma}(m_2 - m_3) + p_{4y} = 0,
\end{aligned}
\tag{5.6}
$$

where

$$
c_i = \cos\delta'_i, \quad s_i = \sin\delta'_i, \quad i = 1,2,3, \tag{5.7}
$$

while axial forces and bending moments are expressed by (5.3) and (5.2), respectively. Note that the equilibrium is written as a system of eight scalar equations in the eight unknown variables v_2, u_3, v_3, u_4, v_4, p_{1x}, p_{1y}, p_{2x}.

5.3.2 Simplified kinematics: symmetric deformation

It is now assumed that the system deforms maintaining its symmetry with respect to the horizontal axis through nodes 3 and 4. Under this assumption, the deformation of the cell is represented in Fig. 5.4a. The kinematics is fully described by the three components of displacement v_2, u_3, and u_4.

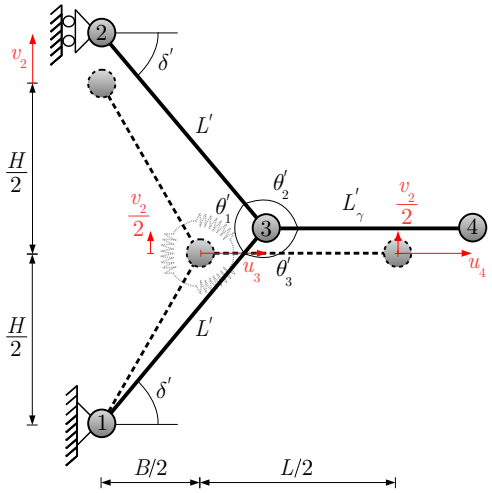

(a) Reference and deformed configurations. The kinematics is simplified and is now governed by three degrees of freedom only

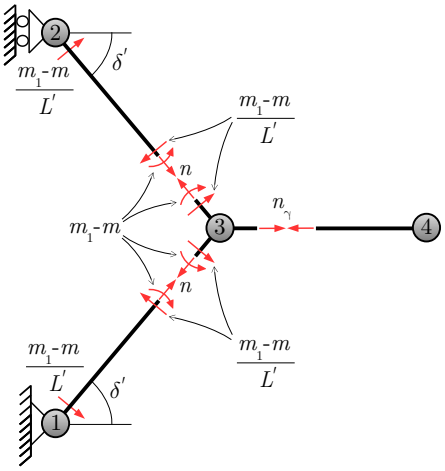

(b) Internal actions in deformed configuration

Figure 5.4: Representative cell in case of symmetric deformation

The lengths of the sticks in deformed configuration are computed using (5.4)

$$L'_\alpha = L'_\beta = L' = \sqrt{\left(\frac{B}{2}+u_3\right)^2+\left(\frac{H}{2}+\frac{v_2}{2}\right)^2}, \quad L'_\gamma = \frac{L}{2}+u_4-u_3, \tag{5.8}$$

The length variations are therefore expressed as

$$\Delta L_\alpha = \Delta L_\beta = \Delta L = \sqrt{\left(\frac{B}{2}+u_3\right)^2+\left(\frac{H}{2}+\frac{v_2}{2}\right)^2}-\frac{L}{2}, \quad \Delta L_\gamma = u_4-u_3.$$

Due to symmetry, $\delta'_1 = \delta'_2 = \delta'$ and $\delta'_3 = 0$. The bond angle variations, expressed by (5.5), assume the form

$$\Delta\theta_1 = 2\arctan\left(\frac{H+v_2}{B+2u_3}\right)-\frac{2}{3}\pi, \quad \Delta\theta_2 = \Delta\theta_3 = \Delta\theta = \frac{\pi}{3}-\arctan\left(\frac{H+v_2}{B+2u_3}\right). \tag{5.9}$$

Since $L'_\alpha = L'_\beta$ and $\Delta\theta_2 = \Delta\theta_3$, the corresponding axial forces and bending moments are equal, namely $n_\alpha = n_\beta = n$ and $m_2 = m_3 = m$. The internal actions in deformed configuration are shown in Fig. 5.4b. Stick γ is only subjected to axial force because the bending moments deriving from the springs cancel each other out.

The equilibrium of the representative cell is analyzed in case of load applied in armchair and zigzag directions. As shown in Fig. 5.5, the armchair and zigzag load cases correspond to a load applied in x and y directions, respectively. In particular, load p_{4x} reproduces the interaction of the cell with adjacent cells in the case that an external load is applied on the graphene sheet along the armchair direction. Similarly, load p_{2y} reproduces the interaction of the cell with adjacent cells in case of

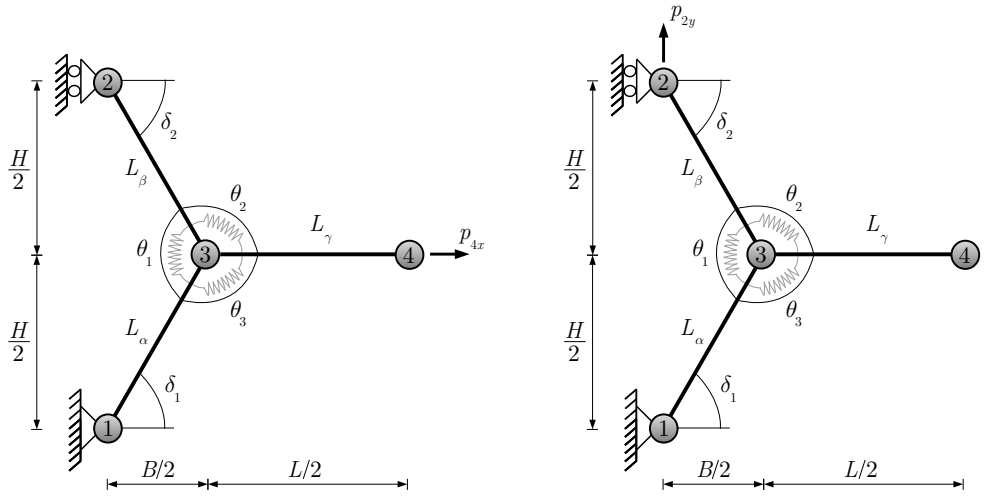

(a) Armchair load case (x direction)

(b) Zigzag load case (y direction)

Figure 5.5: Analysis of the representative cell, armchair and zigzag load cases

an external load applied along the zigzag direction. It is straightforward to conclude that in the armchair load case $p_{1x} = p_{2x} = -p_{4x}/2$ and $p_{1y} = 0$, while in the zigzag load case $p_{1x} = p_{2x} = 0$ and $p_{1y} = -p_{2y}$.

Under the assumption of symmetric deformation, the global equilibrium equations (5.6) reduce to the following system of three equations:

$$\begin{aligned}
&\sum_i F^i_{2y} = -n\sin\delta' - \frac{m_1 - m}{L'}\cos\delta' + p_{2y} = 0,\\
&\sum_i F^i_{3x} = -2n\cos\delta' + n_\gamma + 2\frac{m_1 - m}{L'}\sin\delta' = 0,\\
&\sum_i F^i_{4x} = -n_\gamma + p_{4x} = 0,
\end{aligned} \tag{5.10}$$

where

$$\cos\delta' = \left[1 + \left(\frac{H + v_2}{B + 2u_3}\right)^2\right]^{-\frac{1}{2}}, \quad \sin\delta' = \frac{H + v_2}{B + 2u_3}\left[1 + \left(\frac{H + v_2}{B + 2u_3}\right)^2\right]^{-\frac{1}{2}}. \tag{5.11}$$

The equilibrium equations (5.10) can be also derived by imposing the stationarity of the total potential energy

$$\Pi(u_3, u_4, v_2) = \sum_i V(\Delta L_i) + \sum_j V_\theta(\Delta\theta_j) - p_{4x}u_4 - p_{2y}v_2, \quad i = \alpha, \beta, \gamma, \quad j = 1, 2, 3. \tag{5.12}$$

For the sake of clarity, here we indicate u_3, u_4, and v_2 with $\bar{u}_1$, $\bar{u}_2$, and $\bar{u}_3$, respectively. The partial derivatives of the total potential energy (5.12) are written

as

$$\begin{aligned}\frac{\partial \Pi}{\partial \bar{u}_k} &= \sum_i \frac{\partial V(\Delta L_i)}{\partial \bar{u}_k} + \sum_j \frac{\partial V_\theta(\Delta\theta_j)}{\partial \bar{u}_k} - \frac{\partial}{\partial \bar{u}_k}\left(p_{4x}\bar{u}_2 - p_{2y}\bar{u}_3\right) \\ &= \sum_i n_i \frac{\partial(\Delta L_i)}{\partial \bar{u}_k} + \sum_j m_j \frac{\partial(\Delta\theta_j)}{\partial \bar{u}_k} - \frac{\partial}{\partial \bar{u}_k}\left(p_{4x}\bar{u}_2 - p_{2y}\bar{u}_3\right), \\ & i = \alpha,\beta,\gamma, \quad j = 1,2,3.\end{aligned} \tag{5.13}$$

We recall that $\Delta L_\alpha = \Delta L_\beta = \Delta L$, $\Delta\theta_2 = \Delta\theta_3 = \Delta\theta$, $n_\alpha = n_\beta = n$ and $m_2 = m_3 = m$. The following differential relations hold:

$$\begin{aligned}&\frac{\partial(\Delta L)}{\partial \bar{u}_1} = \cos\delta', \quad \frac{\partial(\Delta L_\gamma)}{\partial \bar{u}_1} = -1, \quad \frac{\partial(\Delta L)}{\partial \bar{u}_2} = 0, \quad \frac{\partial(\Delta L_\gamma)}{\partial \bar{u}_2} = 1, \\ &\qquad \frac{\partial(\Delta L)}{\partial \bar{u}_3} = \frac{\sin\delta'}{2}, \quad \frac{\partial(\Delta L_\gamma)}{\partial \bar{u}_3} = 0, \\ &\frac{\partial(\Delta\theta_1)}{\partial \bar{u}_1} = -2\frac{\sin\delta'}{L'}, \quad \frac{\partial(\Delta\theta)}{\partial \bar{u}_1} = \frac{\sin\delta'}{L'}, \quad \frac{\partial(\Delta\theta_1)}{\partial \bar{u}_2} = \frac{\partial(\Delta\theta)}{\partial \bar{u}_2} = 0, \\ &\qquad \frac{\partial(\Delta\theta_1)}{\partial \bar{u}_3} = \frac{\cos\delta'}{L'}, \quad \frac{\partial(\Delta\theta)}{\partial \bar{u}_3} = -\frac{\cos\delta'}{2L'}.\end{aligned} \tag{5.14}$$

The equilibrium equations (5.10) are retrieved by introducing relations (5.14) into (5.13) and imposing the stationarity condition $\partial\Pi/\partial\bar{u}_k = 0$ for $k = 1,2,3$. This gives a further support to the correctness of the formulation presented in this section.

5.3.3 Stability of the equilibrium

The Hessian matrix of the system is defined as

$$[\mathbf{K}] = \begin{bmatrix} \dfrac{\partial^2\Pi}{\partial\bar{u}_1^2} & \dfrac{\partial^2\Pi}{\partial\bar{u}_1\partial\bar{u}_2} & \dfrac{\partial^2\Pi}{\partial\bar{u}_1\partial\bar{u}_3} \\ \dfrac{\partial^2\Pi}{\partial\bar{u}_2\partial\bar{u}_1} & \dfrac{\partial^2\Pi}{\partial\bar{u}_2^2} & \dfrac{\partial^2\Pi}{\partial\bar{u}_2\partial\bar{u}_3} \\ \dfrac{\partial^2\Pi}{\partial\bar{u}_3\partial\bar{u}_1} & \dfrac{\partial^2\Pi}{\partial\bar{u}_3\partial\bar{u}_2} & \dfrac{\partial^2\Pi}{\partial\bar{u}_3^2} \end{bmatrix},$$

where the displacement components u_3, u_4, and v_2 have been again replaced by $\bar{u}_1$, $\bar{u}_2$, and $\bar{u}_3$ for the sake of clarity. The second partial derivatives of Π can be computed by applying the chain rule twice:

$$\begin{aligned}\frac{\partial^2\Pi}{\partial\bar{u}_k\partial\bar{u}_h} &= \sum_i \frac{\partial^2 V(\Delta L_i)}{\partial\bar{u}_k\partial\bar{u}_h} + \sum_j \frac{\partial^2 V_\theta(\Delta\theta_j)}{\partial\bar{u}_k\partial\bar{u}_h} - \frac{\partial^2}{\partial\bar{u}_k\partial\bar{u}_h}\left(p_{4x}\bar{u}_2 - p_{2y}\bar{u}_3\right) \\ &= \sum_i \frac{\partial^2 V(\Delta L_i)}{\partial(\Delta L_i)^2}\frac{\partial(\Delta L_i)}{\partial\bar{u}_k}\frac{\partial(\Delta L_i)}{\partial\bar{u}_h} + \sum_i n_i \frac{\partial^2(\Delta L_i)}{\partial\bar{u}_k\partial\bar{u}_h} \\ &+ \sum_j \frac{\partial^2 V_\theta(\Delta\theta_j)}{\partial(\Delta\theta_j)^2}\frac{\partial(\Delta\theta_j)}{\partial\bar{u}_k}\frac{\partial(\Delta\theta_j)}{\partial\bar{u}_h} + \sum_j m_j \frac{\partial^2(\Delta\theta_j)}{\partial\bar{u}_k\partial\bar{u}_h}, \quad i = \alpha,\beta,\gamma, \quad j = 1,2,3.\end{aligned}$$

The solution of the characteristic equation

$$\det\left(\mathbf{K}-\tau\mathbf{I}\right)=0 \tag{5.15}$$

provides the eigenvalues $\tau_1(\bar{u}_1,\bar{u}_2,\bar{u}_3)$, $\tau_2(\bar{u}_1,\bar{u}_2,\bar{u}_3)$ and $\tau_3(\bar{u}_1,\bar{u}_2,\bar{u}_3)$ and the stability analysis is carried out by studying their sign.

5.4 Results and discussion

Numerical solutions of the equilibrium equations are provided for the case of uniaxial load applied in both armchair and zigzag configurations. In addition, the case of equibiaxial load is analyzed. Results are given assuming that the thickness of graphene is $t = 0.335$ nm, which is the experimental value of the interlayer spacing between graphene sheets in the graphite structure [144, 145]. This is a common assumption in recent molecular mechanics models [91].

5.4.1 Uniaxial loads: armchair and zigzag load cases

The equilibrium equations (5.10) are solved numerically by increasing step by step a kinematic control parameter. For the armchair load, control parameter is u_4. For the zigzag load, control parameter is v_2. It is recalled that this simulation is performed under the hypothesis that symmetry is mantained during deformation, as discussed in Section 5.3.2.

In the literature, the mechanical properties of graphene are usually given in terms of engineering stress and strain, referring thus to a continuum. The nanoscopic results of the equilibrium are therefore homogenized in order to provide a comparison with previous results in the literature. The results are obtained in the context of nonlinear elasticity and thus the elastic quantities introduced with the homogenization are functions of the deformation. However, we will adopt the notation of the classical theory of linear elasticity, where the equilibrium is written in reference configuration and the elastic constants do not depend on the deformation. This notation is used with the sole purpose of providing straightforward comparisons with other results in the literature.

The homogenization of the discrete solution is performed by defining an equivalent continuum of base $\bar{B} = B/2 + L/2$ and height $\bar{H} = H$. The deformation (strain) components are then obtained as

$$\epsilon_x = \frac{u_4}{\bar{B}}, \quad \epsilon_y = \frac{v_2}{\bar{H}}, \tag{5.16}$$

and the Poisson's ratio along armchair configuration is computed as $\nu_{xy} = -\partial\epsilon_y/\partial\epsilon_x$, while along zigzag configuration $\nu_{yx} = -\partial\epsilon_x/\partial\epsilon_y$.

The stress components are computed by introducing the influence lengths of the applied loads, which are displayed in Fig. 5.6. The influence lengths of the loads in x and y directions are, respectively, $2\bar{H}$ and $2\bar{B}$. The stress components are computed as follows:

$$\sigma_x = \frac{p_{4x}}{2\bar{H}t}, \quad \sigma_y = \frac{p_{2y}}{2\bar{B}t}. \tag{5.17}$$

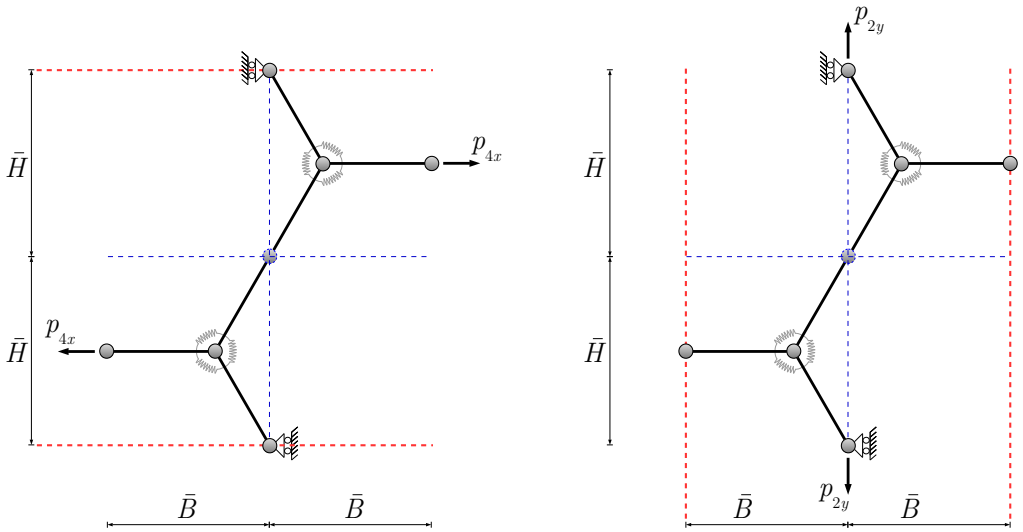

(a) Armchair load case (b) Zigzag load case

Figure 5.6: Influence lengths defined to compute the stress acting on the equivalent continuum

Finally, the expressions of tangent extensional stiffness in x and y directions are

$$k_x = \frac{\partial \sigma_x}{\partial \epsilon_x} t, \quad k_y = \frac{\partial \sigma_y}{\partial \epsilon_y} t.$$

Fig. 5.7 shows the equilibrium paths, namely relation between σ_x and ϵ_x for armchair configuration and relation between σ_y and ϵ_y for zigzag configuration. The results demonstrate that, in both cases, the graphene representative cell displays a softening behavior. The values of longitudinal strains and stresses at the limit configurations are

$$\epsilon_{x,lim} = 19.40\%, \quad \sigma_{x,lim} = 103.89 \ \frac{\text{nN}}{\text{nm}^2},$$
$$\epsilon_{y,lim} = 27.78\%, \quad \sigma_{y,lim} = 132.66 \ \frac{\text{nN}}{\text{nm}^2}.$$

These values are very close to the ones obtained by Genoese et al. [142], where the computational approach is also based on the stick-and-spring model with modified Morse potential and the homegenization is numerically performed through a strategy based on the least-squares method. Tab. 5.1 shows that good agreement is also found with other molecular mechanics (MM) and atomistic simulations, such as MD, density functional theory (DFT) and *ab initio*. The comparison of the results is given in terms of normalized stress, which is computed as stress multiplied by thickness t. In this way the results are compared consistently, irrespective of the value of thickness assumed for the graphene sheet. It is worth mentioning that a surprisingly good agreement is found with the experimental work carried out by Lee

Table 5.1: Values of stress and strain at the limit configurations and comparison with other results available in the literature. The stress is multiplied by t to compare results regardless of the assumptions on the graphene thickness

	Method	$\sigma_{x,lim}\,t$ (nN/nm)	$\epsilon_{x,lim}$	$\sigma_{y,lim}\,t$ (nN/nm)	$\epsilon_{y,lim}$
Present work	MM	34.80	0.194	44.44	0.278
Genoese et al. [142]	MM	34.80	0.192	44.44	0.280
Galhofo et al. [146]	MM	38.42	0.187	48.28	0.211
Nazarloo et al. [143]	MM	32.09	0.183	40.90	0.228
Georgantzinos et al. [141]	MM	31.96	0.198	40.80	0.269
Marenić et al. [147]	MM	30.60	0.15	40.80	0.2
Yanovsky et al. [148]	MD	30.32	0.123	46.43	0.123
Wang et al. [149]	MD	30.60	0.130	35.70	0.220
Zhao et al. [150]	MD	30.26	0.13	35.70	0.2
Ansari et al. [151]	MD	39.34	0.202	-	-
Xu [152]	MD	28.22	0.16	33.32	0.24
Shao et al. [153]	DFT	-	-	39.93	0.27
Liu et al. [154]	*ab initio*	37.40	0.194	41.14	0.266
Lee et al. [64]	Experimental	-	-	43.55	0.25

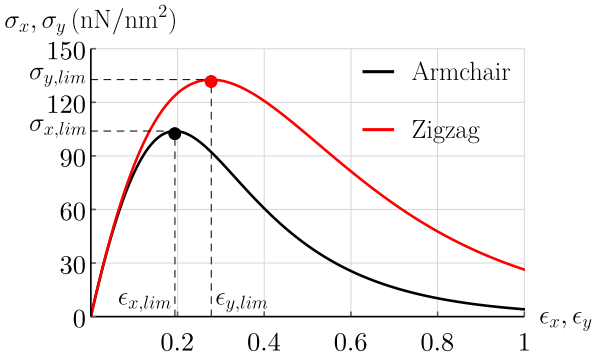

Figure 5.7: Equilibrium paths for the armchair and zigzag uniaxial loads

et al. [64], which provided an ultimate stress in zigzag direction of 130 GPa (43.55 nN/nm) at deformation 25%.

The sensible variability of the limit values given in Tab. 5.1 is due to different computational methods and interatomic potentials used for the interactions between carbon atoms. Furthermore, a certain potential with different set of parameters can lead to significant changes in the results [71]. It goes without saying that the aim of this work is not to analyze these issues, but they still deserve consideration. It is hard to say which potential and set of parameters is the best one, but the quite good agreement of the present solution with other works in the literature is encouraging. The modified Morse potential with parameters given in Section 5.2.1 may not be the best choice, but it is certain that it provides reliable results.

The kinematics of the system in case of armchair load is shown in Figs. 5.8a, 5.8c and 5.8e. In particular, Fig. 5.8c indicates that the elongation of the equivalent continuum affects mainly stick γ. Therefore, the constitutive response of the continuum is qualitatively similar to the one derived from the Morse potential (Fig. 5.2a) and employed for the sticks. This explains the softening behavior of the representative cell subjected to a uniaxial load along the armchair configuration.

Figs. 5.8b, 5.8d and 5.8f show the kinematics of the system in case of zigzag load. For obvious reasons of equilibrium, stick γ does not experience any deformation while sticks α and β undergo the same length variation (Fig. 5.8d). Sticks α and β are inclined with respect to the load direction (y axis). Therefore, the elongation corresponding to the maximum stress is achieved for a deformation $\epsilon_{y,lim}$ higher than $\epsilon_{x,lim}$. Moreover, the maximum stress $\sigma_{y,lim}$ is higher than $\sigma_{x,lim}$. This happens because in this case the whole deformation is absorbed by the two sticks α and β, while in the zigzag load case the sole stick γ undergoes the largest part of the deformation. Hence, the contribution of both sticks α and β add up by making graphene stronger in zigzag configuration.

The tangent extensional stiffness is depicted in Fig. 5.9a. The trend in both armchair and zigzag directions remarks the softening behavior of graphene. We notice that the initial value of both k_x and k_y is 360.29 nN/nm, which indicates that graphene is isotropic for small deformations. This property vanishes with the increase of deformation and graphene becomes anisotropic, as already observed in

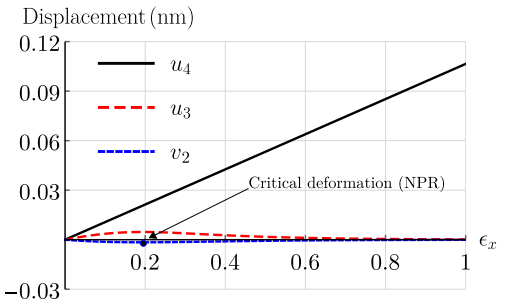

(a) Armchair load: displacements

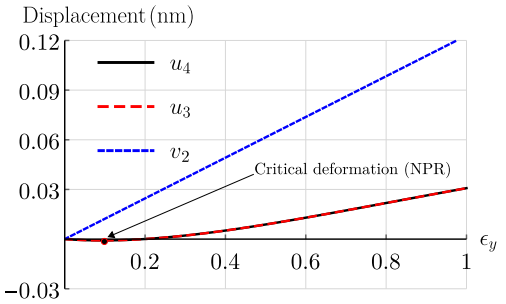

(b) Zigzag load: displacements

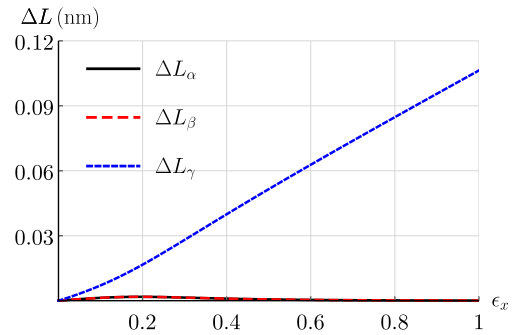

(c) Armchair load: length variations

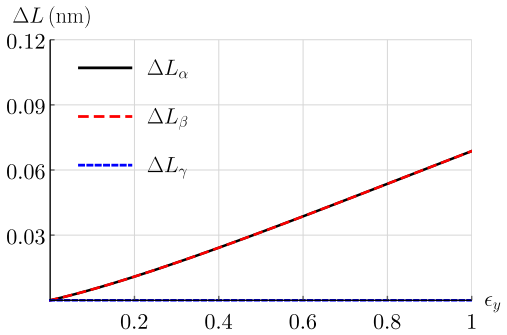

(d) Zigzag load: length variations

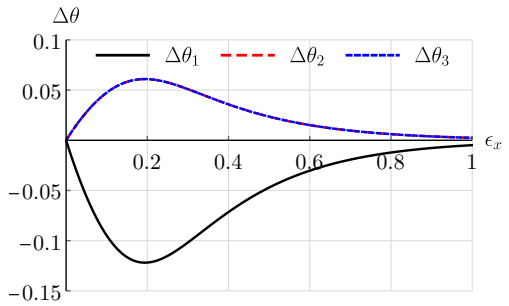

(e) Armchair load: angle variations

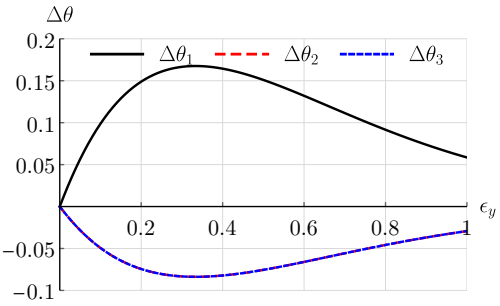

(f) Zigzag load: angle variations

Figure 5.8: Kinematics of the representative cell subjected to uniaxial load

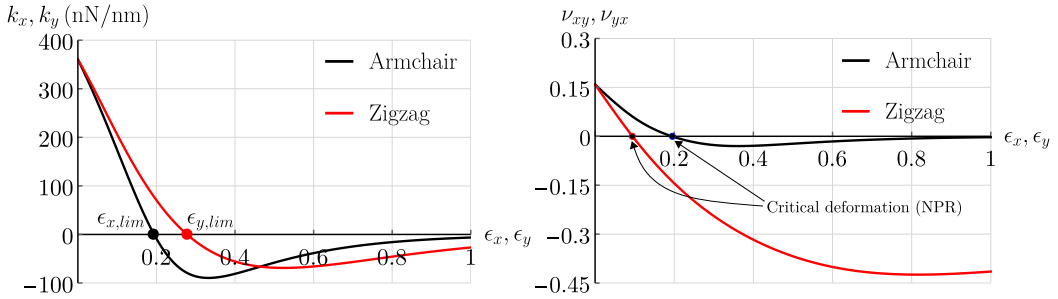

(a) Tangent extensional stiffness

(b) Poisson's ratio

Figure 5.9: Trend of elastic properties of the equivalent continuum with the increasing of the deformation

other works [87, 142, 155].

The stiffness coefficients computed by Singh and Patel [91] applying the Cauchy-Born rule show the same trend of Fig. 5.9a. However, there is a sensible difference in the numerical values because different interatomic potentials were adopted. Specifically, in [91], the Tersoff-Brenner potential with two distinct set of parameters provided the values of stiffness 184.40 and 339 nN/nm. The use of second generation REBO potential produced an extensional stiffness of 354.55 nN/nm. A part from the first of these three values, the other two agree with the initial stiffness 360.29 nN/nm, computed in the present work.

The trend of Poisson's ratio with longitudinal deformation is represented in Fig. 5.9b, for armchair and zigzag cases. The initial value of both ν_{xy} and ν_{yx} is 0.159, which again points out the isotropy of graphene for small deformations. As the deformation increases, anisotropy of Poisson's ratio appears. It is interesting to observe that graphene exhibits a negative Poisson's ratio (NPR) after the critical values of deformation 19.39% and 9.45%, for armchair and zigzag cases respectively. This behavior is explained by Figs. 5.8a and 5.8b. Fig. 5.8a shows that, while control parameter u_4 increases, the variation of v_2 is negative at first, but after the critical deformation its variation becomes positive, which causes a NPR. The same happens in Fig. 5.8a, but in this case control parameter is v_2 and the transversal displacements are u_3 and u_4.

This behavior was already observed in previous works [156–159] and it is explained by analyzing the interaction between the two in-plane deformation modes of graphene, which correspond to bond angle variations and bond length variations (Fig. 5.10). The first yields a positive Poisson's ratio, while the second causes a NPR. Jiang et al. [156] carried out atomistic simulations and observed that the contribute of bond angle variations is relevant when the deformation is relatively small. However, when the critical deformation is reached, bond length variations become dominant and graphene exhibits a NPR. Indeed, Figs. 5.8c, 5.8d, 5.8e and 5.8f show that the length variations increase monotonically with increasing deformation, until their contribute exceeds that of the bond angle variations and produces a NPR.

Although the mechanisms of the NPR phenomenon are the same, different ranges

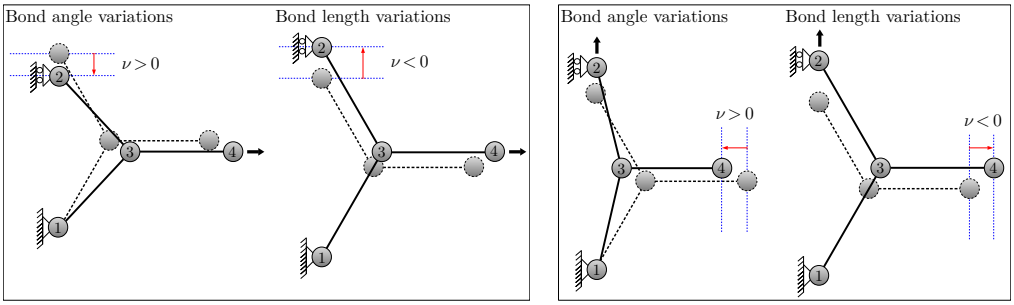

(a) Armchair load (b) Zigzag load

Figure 5.10: Deformation modes of the representative cell and corresponding effects on the Poisson's ratio of the equivalent continuum

of critical deformation were obtained in literature. For instance, Wang et al. [158] reported critical deformations ranging between 6% and 17% changing tensile direction while Qin [157] derived the values 18% and 17% in armchair and zigzag directions, respectively. The discrepancies between the values of critical deformation are due to different computational methods and different potentials for the interactions between carbon atoms.

5.4.2 Equibiaxial load

The equibiaxial load is characterized by $\sigma_x = \sigma_y = \sigma$. This condition is obtained by imposing $p_{2y} = \sqrt{3}p_{4x}/2$. As done previously, the equilibrium equations (5.10) are solved numerically. The solution is unique until the limit configuration

$$\epsilon_{x,lim} = \epsilon_{y,lim} = \epsilon_{lim} = 22.50\%, \quad \sigma_{x,lim} = \sigma_{y,lim} = \sigma_{lim} = 103.89 \ \frac{\text{nN}}{\text{nm}^2},$$

after which three separate solutions are found.

The first solution (Fig. 5.11a) is obtained by assuming v_2 or equivalently u_4 as control parameter. As v_2 or u_4 increases, the solution of the equilibrium equations is unique. However, after the limit configuration, other solutions are found depending on the control parameter considered. In detail, considering v_2 as control parameter, not only the first solution is found after the limit configuration, but also the second solution depicted in Fig. 5.11b exists. Considering u_4 as control parameter, the first solution is again not the only one after the limit configuration, but also the third solution given in Fig. 5.11c is found. Hence, depending on the control parameter, multiple solutions of the equilibrium are discovered.

The first solution preserves the isotropy regardless of the magnitude of deformation. In fact, both stress and strain along x and y directions coincide. The second solution after the limit configuration follows a second branch of equilibrium. Along this branch, the deformation of the equivalent continuum is non-symmetric. Specifically, the longitudinal strain along y axis is greater than the one along x axis. This means that the continuum undergoes a non-isotropic deformation despite the symmetry of the load. The third solution after the limit configuration follows a third

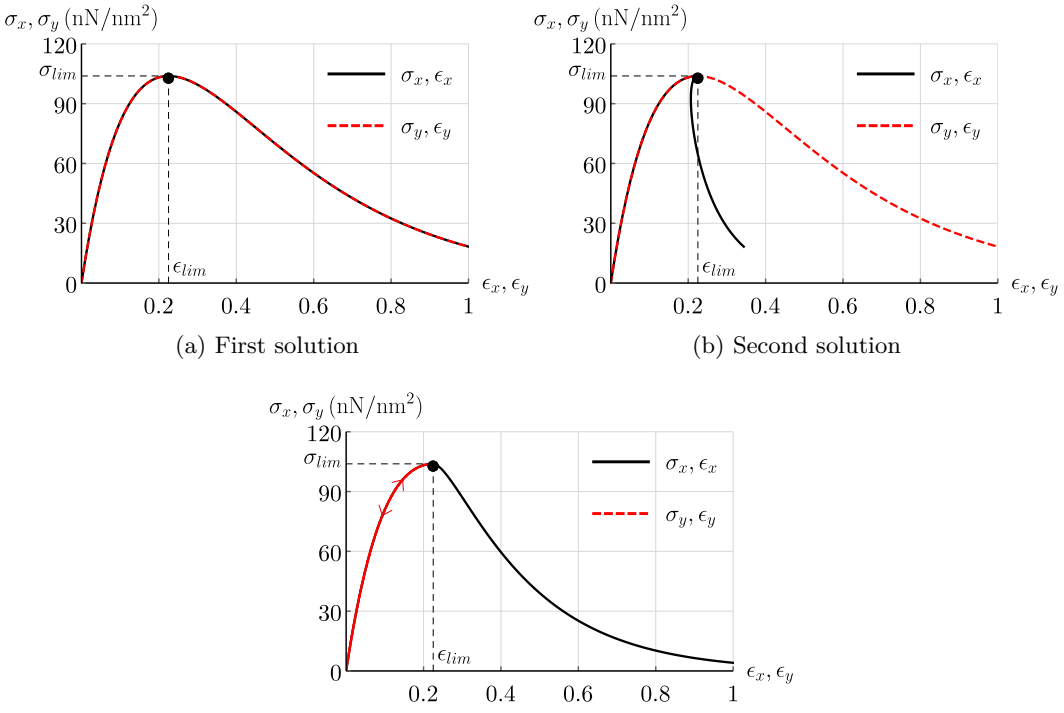

(a) First solution

(b) Second solution

(c) Third solution

Figure 5.11: Equilibrium paths for the case of equibiaxial load. The solution is unique until the limit configuration $(\epsilon_{lim}, \sigma_{lim})$, after which three separate solutions are found

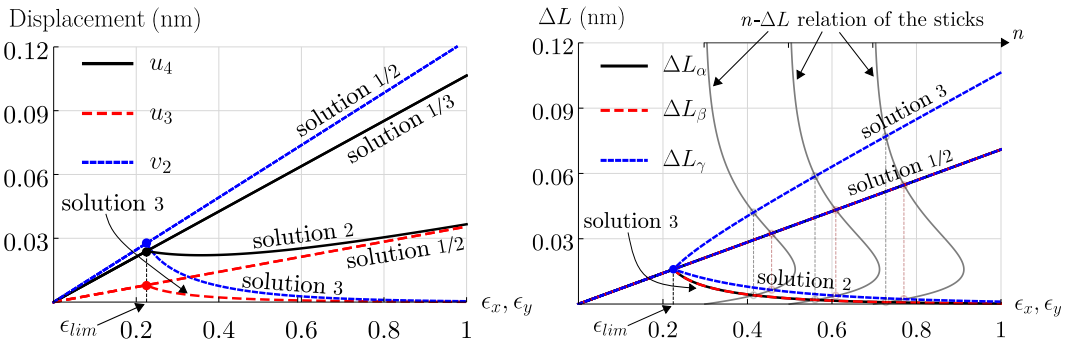

(a) Displacements

(b) Length variations and constitutive law of the sticks, which shows that in each configuration they are subjected to the same axial forces

Figure 5.12: Kinematics of the representative cell subjected to equibiaxial load

branch of equilibrium. The deformation along x axis increases, while the deformation along y axis decreases following the loading path backwards. Also in this case the continuum experiences a non-isotropic deformation.

Figs. 5.12a and 5.12b show the displacements of the nodes and the length variations of the sticks, respectively. It is again observed that the solution is unique only before the limit configuration. The bond angle variations are not reported because they are equal to zero for all three solutions. The configurations of minimum energy are therefore those where no bending moments arise on the sticks. This is not a surprise for the first solution, for which the behavior is isotropic. In this case, for a given deformed configuration, all the sticks undergo the same length variations and thus the same axial forces ($n_\alpha = n_\beta = n_\gamma$).

Regarding the second and third solutions, the geometry does not maintain the symmetry and therefore the axial strains ϵ_x and ϵ_y assume different values. Indeed, for a given deformed configuration, the length variations of the sticks assume different values as well. The gray curves of Fig. 5.12b represent the constitutive law of the sticks, expressed by (5.3). We notice that, in each configuration, the length variations are such that the sticks are subjected to the same axial forces. In other words, although the sticks undergo different length variations, their axial forces are equal. This explains why also for the second and third solutions the equilibrium is satisfied without bending moments on the sticks.

Non-isotropic responses of graphene when subjected to symmetric loads are somewhat surprising, but this behavior is also observed in other circumstances. For instance, the case of an isotropic and hyperelastic square membrane stretched by a double symmetric load was investigated in [49, 160, 161]. It was discovered that, depending on the stored energy function employed, the system may admit asymmetric solutions in addition to the expected symmetric one. Another similar result was obtained for the case of a cube subjected to equitriaxial dead-load tractions [37]. Again, when certain stored energy functions are adopted, symmetric loads may give rise to asymmetric deformations. The same conclusion is drawn from the results of

the present work, where asymmetric solutions appear because the Morse potential is employed for the sticks. In the event that a harmonic potential is adopted instead of the Morse potential, it is certain that such solutions do not exist. The present result gives an example of atomistic origin of multiple equilibrium solutions in the continuum theory.

5.4.3 Stable equilibrium configurations

The stability of the solutions obtained is now assessed by solving numerically the characteristic equation (5.15). The equilibrium paths for zigzag and armchair loads are given in Fig. 5.13a, where stable solutions are displayed with continuous lines and unstable solutions with dashed lines. The values of longitudinal strains and stresses at the critical configurations are

$$\epsilon_{x,cr} = 33.29\%, \quad \sigma_{x,cr} = 77.90 \ \frac{\text{nN}}{\text{nm}^2},$$
$$\epsilon_{y,cr} = 27.78\%, \quad \sigma_{y,cr} = 132.66 \ \frac{\text{nN}}{\text{nm}^2}.$$

For the zigzag load, the critical configuration takes place when the load reaches its maximum value. As expected, the softening branch is unstable. An unexpected result is instead obtained in case of armchair load, where the critical configuration $(\epsilon_{x,cr}, \sigma_{x,cr})$ does not match with the limit configuration $(\epsilon_{x,lim}, \sigma_{x,lim})$ and a portion of the softening branch is stable. The explanation for this unusual result is that we are analyzing a discrete structural system, but the results are reported referring to an equivalent continuum. Strictly speaking, this equivalence is not entirely consistent and both stress and strain components are conveniently defined in order to provide comparisons with other results found in the literature. This leads to the unexpected behavior mentioned above, which should be rather investigated in terms of discrete results of the stick-and-spring system.

In the case of equibiaxial load the solution of the equilibrium is stable until the critical configuration

$$\epsilon_{cr} = 22.50\%, \quad \sigma_{cr} = 103.89 \ \frac{\text{nN}}{\text{nm}^2},$$

which corresponds to the limit point (ϵ_{lim}, σ_{lim}). After this critical configuration, the three solutions are unstable, as shown in Fig. 5.13b. The fact that the three softening branches are unstable does not mean that they can not be observed. If a displacement controlled test is performed, such solutions can be potentially detected. Note that this analysis is limited to the representative cell of graphene. It goes without saying that this is not necessarily representative of the behavior of an entire graphene sheet composed of a certain number of atoms, where size effects and possible defects might influence its response. However, the present results provide interesting insights into the mechanical behavior of pristine graphene.

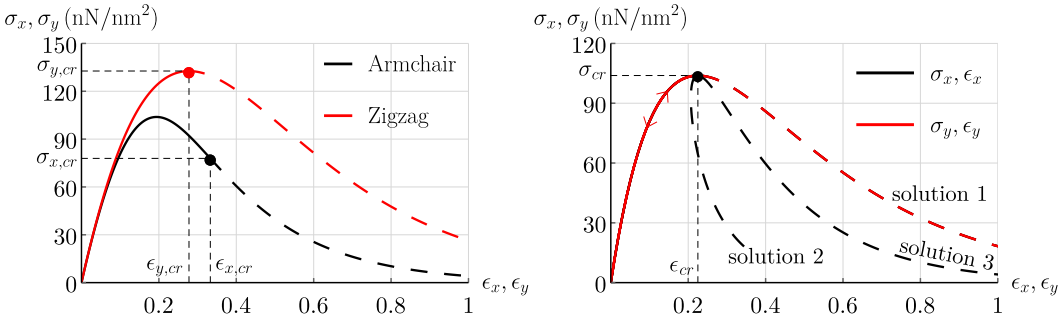

(a) Uniaxial loads along armchair and zigzag directions

(b) Equibiaxial load

Figure 5.13: Stable (*continuous lines*) and unstable (*dashed lines*) solutions of the equilibrium

5.5 Linearized solution of the equilibrium

The equilibrium equations are now linearized by introducing the hypothesis of small displacements. The linearization of the constitutive response of sticks and springs, given respectively by (5.3) and (5.2), reads

$$\begin{aligned} n_i &= 2k_L \Delta L_i, \quad i = \alpha, \beta, \gamma, \\ m_j &= k_\theta \Delta\theta_j, \quad j = 1, 2, 3, \end{aligned} \tag{5.18}$$

where $k_L = 2D_e\kappa^2 = 742$ nN/nm, which corresponds to the stiffness of the covalent bond given by Chang and Gao [137]. The stiffness of the sticks is $2k_L$ because the length variation is half the one of the entire covalent bond, as already pointed out when we introduced the constitutive relation (5.3).

The lengths of the sticks, expressed by (5.8), assume the linearized form

$$L'_\alpha = L'_\beta = \frac{1}{2}\left(L + u_3 + \frac{1}{2}\sqrt{3}\, v_2\right), \quad L'_\gamma = \frac{L}{2} + u_4 - u_3,$$

and their variations become

$$\Delta L_\alpha = \Delta L_\beta = \frac{1}{2}\left(u_3 + \frac{1}{2}\sqrt{3}\, v_2\right), \quad \Delta L_\gamma = u_4 - u_3. \tag{5.19}$$

The kinematic quantities in (5.11) turn into

$$\cos\delta' = \frac{2L + 6u_3 - \sqrt{3}\, v_2}{4L}, \quad \sin\delta' = \frac{2\sqrt{3}\, L - 2\sqrt{3}\, u_3 + v_2}{4L}, \tag{5.20}$$

and the bond angle variations, experssed by (5.9), assume the form

$$\Delta\theta_1 = \frac{v_2 - 2\sqrt{3}\, u_3}{L}, \quad \Delta\theta_2 = \Delta\theta_3 = -\frac{\Delta\theta_1}{2}. \tag{5.21}$$

The axial forces and bending moments are derived by substituting (5.19) and (5.21) into (5.18). Consequently, using (5.20), the linearized form of the equilibrium equations (5.10) is obtained

$$\begin{aligned} 2\sqrt{3}\,u_3\left(6k_\theta - k_L L^2\right) - 3v_2\left(k_L L^2 + 2k_\theta\right) + 4L^2 p_{2y} = 0, \\ 2u_3\left(k_L L^2 + 18k_\theta\right) + \sqrt{3}\,v_2\left(k_L L^2 - 6k_\theta\right) - 2L^2 p_{4x} = 0, \\ p_{4x} - 2k_L\left(u_4 - u_3\right) = 0. \end{aligned} \tag{5.22}$$

The solution of the system of equations (5.22) in the armchair load case ($p_{2y} = 0$) is

$$u_3 = \frac{\left(2k_\theta + k_L L^2\right) p_{4x}}{32 k_L k_\theta}, \quad u_4 = \frac{1}{32}\left(\frac{18}{k_L} + \frac{L^2}{k_\theta}\right) p_{4x}, \quad v_2 = -\frac{\left(k_L L^2 - 6k_\theta\right) p_{4x}}{16\sqrt{3} k_L k_\theta},$$

from which, using (5.16), the following deformation components are obtained:

$$\epsilon_x = \left(\frac{3}{4k_L L} + \frac{L}{24k_\theta}\right) p_{4x}, \quad \epsilon_y = -\left(\frac{L}{24k_\theta} - \frac{1}{4k_L L}\right) p_{4x}, \quad \nu_{xy} = 1 - \frac{24k_\theta}{k_L L^2 + 18k_\theta}.$$

Stress component σ_x is computed through (5.17) and the expression of the Young's modulus in armchair direction is derived

$$E_x = \frac{\sigma_x}{\epsilon_x} = \frac{8\sqrt{3} k_L k_\theta}{\left(k_L L^2 + 18k_\theta\right) t}.$$

The solution of the system of equations (5.22) in the zigzag load case ($p_{4x} = 0$) is

$$\begin{aligned} u_3 = u_4 = -\frac{\left(k_L L^2 - 6k_\theta\right) p_{2y}}{16\sqrt{3} k_L k_\theta}, \\ v_2 = \frac{1}{24}\left(\frac{18}{k_L} + \frac{L^2}{k_\theta}\right) p_{2y}, \end{aligned}$$

from which, using (5.16), the following deformation components are obtained:

$$\epsilon_x = -\frac{\left(k_L L^2 - 6k_\theta\right) p_{2y}}{12\sqrt{3} k_L k_\theta L}, \quad \epsilon_y = \frac{\left(k_L L^2 + 18k_\theta\right) p_{2y}}{12\sqrt{3} k_L k_\theta L}, \quad \nu_{yx} = 1 - \frac{24k_\theta}{k_L L^2 + 18k_\theta}.$$

Stress component σ_y is computed through (5.17) and the expression of the Young's modulus in zigzag direction is derived

$$E_y = \frac{\sigma_y}{\epsilon_y} = \frac{8\sqrt{3} k_L k_\theta}{\left(k_L L^2 + 18k_\theta\right) t}.$$

We notice that $E_x = E_y = E$ and $\nu_{xy} = \nu_{yx} = \nu$, which confirm the isotropy of graphene for small deformations.

The analytical expressions of Young's modulus and Poisson's ratio derived with the linearization of the nonlinear formulation correspond to the ones reported in

Table 5.2: Comparison of Young's modulus and Poisson's ratio with previous studies in the literature. The Young's modulus is multiplied by t to compare results regardless of the assumptions on the graphene thickness

	Method	Et (nN/nm)	ν
Present work	MM	360.29	0.159
Chang and Gao [137]	MM	360.29	0.159
Meo and Rossi [83]	MM	321.30	-
Genoese et al. [71]	MM	386.58	0.195
Alzebdeh [162]	MM	408.00	0.195
Milowska et al. [163]	DFT	357.00	0.169
Liu et al. [154]	*ab initio*	357.00	0.186
Kudin et al. [164]	*ab initio*	337.96	0.149
Shao et al. [153]	*ab initio*	350.01	-
Lee et al. [64]	Experimental	333.54	-
Koenig et al. [122]	Experimental	347	-

Refs. [137, 139]. This provides a further support to the approach presented in this work. By substituting the values of the constitutive constants into the expressions of Young's modulus and Poisson's ratio we obtain $E = 1075.5$ GPa and $\nu = 0.159$.

A comparison with the values given by other studies is reported in Tab. 5.2. Although different methods and potentials are employed in the literature, the results show good agreement. However, as pointed out in Section 5.4.1, variations in the parametrization of the potentials may cause sensible changes in the solution. In particular, the influence on the Poisson's ratio is the most significant. In fact, Genoese et al. [71] obtained $\nu = 0.345$ with the parameters of the Morse potential proposed by Belytschko et al. [80], while with the parameters of the present work they obtained the elastic constants given in Tab. 5.2 ($\nu = 0.195$). This large difference in the results reveals the importance of the parametrization of the potential adopted. Once again we remind that the scope of this work is not to analyze this issue and try to state which potential and parameters are the most proper. This should be probably addressed by analyzing carefully experimental data and simulations available in the literature. Nevertheless, the good match between the elastic constants given in Tab. 5.2 gives confidence in the results of the present work.

5.6 Concluding remarks on the results of the analysis

A fully nonlinear stick-and-spring model for graphene subjected to in-plane deformations was presented. The modified Morse potential and a nonlinear bond angle potential was used for the atomic interactions. The equilibrium equations were written in deformed configuration and numerical solutions was provided for uniaxial and equibiaxial loads. A good agreement was found between the present results and the ones reported in other works. The stability of the equilibrium solutions was also

investigated using an energy criterion.

It was discovered that graphene is isotropic only for small deformations, while it exhibits a strong anisotropy and a softening behavior when subjected to large deformations. A negative Poisson's ratio was found after critical values of deformation, which is explained by the interaction between the two in-plane deformation modes of graphene. In the case of equibiaxial load, the solution is unique until a limit configuration is reached. At this point, three separate equilibrium paths appear. Specifically, graphene can experience non-isotropic deformations when symmetric loads are applied.

The nonlinear formulation of the equilibrium was linearized with the assumption of small displacements of the nodes. The expressions of Young's modulus and Poisson's ratio reported in [137, 139] were retrieved, providing a further support to the results presented in this work.

Chapter 6

Conclusions and perspectives

This thesis presented a formulation for equilibrium and stability of truss structures in finite elasticity. Unlike the other models that can be found in the literature, both displacement and deformation fields are considered large. The kinematics is exactly described, without having recourse to hypotheses that are in contrast with the behavior of solids subjected to finite deformations. The equilibrium equations are derived for a general stored energy function. In this way, the equilibrium can be specialized for any isotropic material with a certain nonlinear constitutive response.

Applications and comparisons with other models found in the literature demonstrated that it is necessary to take into account both geometric and constitutive nonlinearities. The assumption of linear elastic material leads to results that are not consistent with the actual behavior of truss systems.

The validation of the proposed formulation was done through a comparison with experimental and numerical results. It was demonstrated that the model provides an accurate description of equilibrium and post-critical behavior of the von Mises truss, and therefore of truss structures in general. Hence, the model presented contributes to deepen the understanding of the nonlinear behavior of truss structures when subjected to large displacements and deformations.

The fully nonlinear formulation for truss structures presented in this thesis is not only valid for macroscopic systems, but also for nanostructures. In fact, the three-bar truss analyzed in Chapter 4 is representative for the analysis of the in-plane mechanical behavior of graphene. The modified Morse potential was employed for the constitutive behavior of the bars. In this way, the covalent bonds between carbon atoms are properly simulated. It was shown that the highly nonlinear constitutive behavior leads to a complex scenario of equilibrium solutions that includes multiple critical points, snap-through and bifurcation.

In the application of the three-bar truss to the graphene nanostructure, we neglected long range and angular interactions. Therefore, in Chapter 5, the truss model was extended by introducing nonlinear rotational springs. This allowed to give a complete and accurate description of the mechanics of graphene for large in-plane deformations. It was discovered that graphene is isotropic for small deformations, while it exhibits anisotropy when subjected to large deformations. A negative Poisson's ratio was observed after critical strains and, in the case of equibiaxial load,

multiple solutions of the equilibrium were found.

The main ideas and perspectives for future developments are listed in the following:

- The molecular mechanics model for graphene presented in this thesis is limited to the study of the representative cell of graphene. A future aim of the research is the extension of the formulation to a whole graphene sheet composed of a variable number of cells. Simulations of the mechanical behavior of graphene sheets with different size will allow to investigate the size effect on the global response and thus the transition from atomistic to continuum theory;

- An anisotropic stored energy function for graphene will be defined. A continuum model in finite elasticity that includes the size effect will be thus developed (for instance a membrane theory);

- Additional experimental tests on the von Mises truss will be carried out. Various loading conditions will be studied and the interaction between snap-through and Eulerian buckling will be further examined.

Bibliography

[1] L. Kwasniewski. Complete equilibrium paths for Mises trusses. *International Journal of Non-Linear Mechanics*, 44(1):19–26, 2009.

[2] R. V. Mises. Über die stabilitätsprobleme der elastizitätstheorie. *ZAMM-Journal of Applied Mathematics and Mechanics/Zeitschrift für Angewandte Mathematik und Mechanik*, 3(6):406–422, 1923.

[3] R. V. Mises and J. Ratzersdorfer. Die Knicksicherheit von Fachwerken. *ZAMM-Journal of Applied Mathematics and Mechanics/Zeitschrift für Angewandte Mathematik und Mechanik*, 5(3):218–235, 1925.

[4] D. A. Pecknold, J. Ghaboussi, and T. J. Healey. Snap-through and bifurcation in a simple structure. *Journal of Engineering Mechanics*, 111(7):909–922, 1985.

[5] S. S. Ligaro and P. S. Valvo. Large displacement analysis of elastic pyramidal trusses. *International Journal of Solids and Structures*, 43(16):4867–4887, 2006.

[6] M. Rezaiee-Pajand and A. R. Naghavi. Accurate solutions for geometric nonlinear analysis of eight trusses. *Mechanics Based Design of Structures and Machines*, 39(1):46–82, 2011.

[7] K. S. Novoselov, D. Jiang, F. Schedin, T. J. Booth, V. V. Khotkevich, S. V. Morozov, and A. K. Geim. Two-dimensional atomic crystals. *Proceedings of the National Academy of Sciences*, 102(30):10451–10453, 2005.

[8] T. Schioler and S. Pellegrino. Space frames with multiple stable configurations. *AIAA Journal*, 45(7):1740–1747, 2007.

[9] L. A. Danso and E. G. Karpov. Cusp singularity-based bistability criterion for geometrically nonlinear structures. *Extreme Mechanics Letters*, 13:135–140, 2017.

[10] D. Orlando, C. H. L. de Castro, and P. B. Gonçalves. Nonlinear vibrations and instability of a bistable shallow reticulated truss. *Nonlinear Dynamics*, 94(2):1479–1499, 2018.

[11] P. Schorr, V. Böhm, L. Zentner, and K. Zimmermann. Motion characteristics of a vibration driven mobile tensegrity structure with multiple stable equilibrium states. *Journal of Sound and Vibration*, 437:198–208, 2018.

[12] A. López, I. Puente, and M. A. Serna. Numerical model and experimental tests on single-layer latticed domes with semi-rigid joints. *Computers & Structures*, 85(7-8):360–374, 2007.

[13] J. Paulose, A. S. Meeussen, and V. Vitelli. Selective buckling via states of self-stress in topological metamaterials. *Proceedings of the National Academy of Sciences*, 112(25):7639–7644, 2015.

[14] Y. Zhang, M. Tichem, and F. van Keulen. Rotational snap-through behavior of multi-stable beam-type metastructures. *International Journal of Mechanical Sciences*, 193:106172, 2021.

[15] S. Barbarino, F. S. Gandhi, and R. Visdeloup. A bi-stable von-Mises truss for morphing applications actuated using shape memory alloys. In *Smart Materials, Adaptive Structures and Intelligent Systems*, volume 56031, page V001T01A004. ASME, 2013.

[16] B. Camescasse, A. Fernandes, and J. Pouget. Bistable buckled beam: Elastica modeling and analysis of static actuation. *International Journal of Solids and Structures*, 50(19):2881–2893, 2013.

[17] M. J. Frazier and D. M. Kochmann. Band gap transmission in periodic bistable mechanical systems. *Journal of Sound and Vibration*, 388:315–326, 2017.

[18] C. Armanini, F. Dal Corso, D. Misseroni, and D. Bigoni. From the elastica compass to the elastica catapult: an essay on the mechanics of soft robot arm. *Proceedings of the Royal Society A: Mathematical, Physical and Engineering Sciences*, 473(2198):20160870, 2017.

[19] A. Cazzolli and F. Dal Corso. Snapping of elastic strips with controlled ends. *International Journal of Solids and Structures*, 2018.

[20] P. Moser, S. Barbarino, and F. Gandhi. Helicopter rotor-blade chord extension morphing using a centrifugally actuated von Mises truss. *Journal of Aircraft*, 51(5):1422–1431, 2014.

[21] Z. P. Bažant and L. Cedolin. *Stability of structures: elastic, inelastic, fracture and damage theories*. World Scientific, 1991.

[22] P. X. Bellini. The concept of snap-buckling illustrated by a simple model. *International Journal of Non-Linear Mechanics*, 7(6):643–650, 1972.

[23] M. A. Savi, P. M. C. L. Pacheco, and A. M. B. Braga. Chaos in a shape memory two-bar truss. *International Journal of Non-Linear Mechanics*, 37(8):1387–1395, 2002.

[24] M. Psotny and J. Ravinger. Von Mises truss with imperfection. *Slovak Journal of Civil Engineering*, 11:1–7, 2003.

[25] F. Bazzucchi, A. Manuello, and A. Carpinteri. Interaction between snap-through and Eulerian instability in shallow structures. *International Journal of Non-Linear Mechanics*, 88:11–20, 2017.

[26] M. Mooney. A theory of large elastic deformation. *Journal of Applied Physics*, 11(9):582–592, 1940.

[27] Y. Basar and D. Weichert. *Nonlinear continuum mechanics of solids: fundamental mathematical and physical concepts*. Springer Science & Business Media, 2013.

[28] J. L. Ericksen. Deformations possible in every isotropic, incompressible, perfectly elastic body. *Zeitschrift für angewandte Mathematik und Physik ZAMP*, 5(6):466–489, 1954.

[29] A. M. Tarantino. The singular equilibrium field at the notch-tip of a compressible material in finite elastostatics. *Zeitschrift für angewandte Mathematik und Physik ZAMP*, 48(3):370–388, 1997.

[30] J. L. Synge and A. Schild. *Tensor calculus*, volume 5. Courier Corporation, 1978.

[31] A. E. Green and W. Zerna. *Theoretical elasticity*. Courier Corporation, 1992.

[32] A. Hoger and D. E. Carlson. Determination of the stretch and rotation in the polar decomposition of the deformation gradient. *Quarterly of Applied Mathematics*, 42(1):113–117, 1984.

[33] G. Piola. *La meccanica de'corpi naturalmente estesi: trattata col calcolo delle variazioni*. Presso Paolo Emilio Giusti, 1833.

[34] M. M. Carroll. Finite strain solutions in compressible isotropic elasticity. *Journal of Elasticity*, 20(1):65–92, 1988.

[35] J. E. Marsden and T. J. R. Hughes. *Mathematical foundations of elasticity*. Courier Corporation, 1994.

[36] L. Lanzoni and A. M. Tarantino. Equilibrium configurations and stability of a damaged body under uniaxial tractions. *Zeitschrift für angewandte Mathematik und Physik ZAMP*, 66(1):171–190, 2015.

[37] A. M. Tarantino. Homogeneous equilibrium configurations of a hyperelastic compressible cube under equitriaxial dead-load tractions. *Journal of Elasticity*, 92(3):227, 2008.

[38] A. M. Tarantino. Equilibrium paths of a hyperelastic body under progressive damage. *Journal of Elasticity*, 114(2):225–250, 2014.

[39] W. T. Koiter. *On the stability of elastic equilibrium*, volume 833. National Aeronautics and Space Administration, 1967.

[40] L. Cedolin et al. *Stability of structures: elastic, inelastic, fracture and damage theories*. World Scientific, 2010.

[41] C. H. Yoo and S. Lee. *Stability of structures: principles and applications*. Elsevier, 2011.

[42] H. Ziegler. *Principles of structural stability*, volume 35. Birkhäuser, 2013.

[43] F. Faa di Bruno. Sullo sviluppo delle funzioni. *Annali di scienze matematiche e fisiche*, 6:479–480, 1855.

[44] R. S. Rivlin and A. G. Thomas. Rupture of rubber. I. Characteristic energy for tearing. *Journal of Polymer Science*, 10(3):291–318, 1953.

[45] R. S. Rivlin and D. W. Saunders. Large elastic deformations of isotropic materials vii. experiments on the deformation of rubber. *Philosophical Transactions of the Royal Society of London. Series A, Mathematical and Physical Sciences*, 243(865):251–288, 1951.

[46] L. Lanzoni and A. M. Tarantino. A simple nonlinear model to simulate the localized necking and neck propagation. *International Journal of Non-Linear Mechanics*, 84:94–104, 2016.

[47] A. M. Tarantino. Thin hyperelastic sheets of compressible material: field equations, airy stress function and an application in fracture mechanics. *Journal of Elasticity*, 44(1):37–59, 1996.

[48] A. M. Tarantino. Crack propagation in finite elastodynamics. *Mathematics and Mechanics of Solids*, 10(6):577–601, 2005.

[49] A. M. Tarantino and A. Nobili. Finite homogeneous deformations of symmetrically loaded compressible membranes. *Zeitschrift für angewandte Mathematik und Physik ZAMP*, 58(4):659–678, 2007.

[50] P. G. Ciarlet and G. Geymonat. Sur les lois de comportement en élasticité non linéaire compressible. *CR Acad Sci Paris Sér II*, 295:423–426, 1982.

[51] A. M. Tarantino. Nonlinear fracture mechanics for an elastic Bell material. *Quarterly Journal of Mechanics and Applied Mathematics*, 50(3):435–456, 1997.

[52] A. M. Tarantino. On the finite motions generated by a mode I propagating crack. *Journal of Elasticity*, 57(2):85–103, 1999.

[53] L. Lanzoni and A. M. Tarantino. Damaged hyperelastic membranes. *International Journal of Non-Linear Mechanics*, 60:9–22, 2014.

[54] L. Lanzoni and A. M. Tarantino. Finite anticlastic bending of hyperelastic solids and beams. *Journal of Elasticity*, 131(2):137–170, 2018.

[55] F. O. Falope, L. Lanzoni, and A. M. Tarantino. The bending of fully nonlinear beams. Theoretical, numerical and experimental analyses. *International Journal of Engineering Science*, 145:103167, 2019.

[56] M. Pelliciari and A. M. Tarantino. Equilibrium paths for von Mises trusses in finite elasticity. *Journal of Elasticity*, 138(2):145–168, 2020.

[57] R. W. Ogden. Large deformation isotropic elasticity: on the correlation of theory and experiment for compressible rubberlike solids. *Proceedings of the Royal Society of London. A. Mathematical and Physical Sciences*, pages 567–583, 1972.

[58] A. N. Gent. A new constitutive relation for rubber. *Rubber Chemistry and Technology*, 69(1):59–61, 1996.

[59] O. F. Falope, M. Pelliciari, L. Lanzoni, and A. M. Tarantino. Snap-through and Eulerian buckling of the bi-stable von Mises truss in nonlinear elasticity: A theoretical, numerical and experimental investigation. *International Journal of Non-Linear Mechanics*, accepted.

[60] M. Grediac. The use of full-field measurement methods in composite material characterization: interest and limitations. *Composites Part A: Applied Science and Manufacturing*, 35(7-8):751–761, 2004.

[61] A. B. Comsol. COMSOL multiphysics user's guide. *Version: September*, 10:333, 2005.

[62] D. Whitley. A genetic algorithm tutorial. *Statistics and Computing*, 4(2):65–85, 1994.

[63] Y. Cengiz Toklu, R. Temür, and G. Bekdaş. Computation of nonunique solutions for trusses undergoing large deflections. *International Journal of Computational Methods*, 12(03):1550022, 2015.

[64] C. Lee, X. Wei, J. W. Kysar, and J. Hone. Measurement of the elastic properties and intrinsic strength of monolayer graphene. *Science*, 321(5887):385–388, 2008.

[65] C. A. Marianetti and H. G. Yevick. Failure mechanisms of graphene under tension. *Physical Review Letters*, 105(24):245502, 2010.

[66] H. Bu, Y. Chen, M. Zou, H. Yi, K. Bi, and Z. Ni. Atomistic simulations of mechanical properties of graphene nanoribbons. *Physics Letters A*, 373(37):3359–3362, 2009.

[67] M. Pelliciari and A. M. Tarantino. Equilibrium paths of a three-bar truss in finite elasticity with an application to graphene. *Mathematics and Mechanics of Solids*, 25(3):705–726, 2020.

[68] Z. Peng, H. Yonggang, P. H. Geubelle, and H. Kehchih. On the continuum modeling of carbon nanotubes. *Acta Mechanica Sinica*, 18(5):528–536, 2002.

[69] J. Tersoff. New empirical approach for the structure and energy of covalent systems. *Physical Review B*, 37(12):6991, 1988.

[70] D. W. Brenner. Empirical potential for hydrocarbons for use in simulating the chemical vapor deposition of diamond films. *Physical Review B*, 42(15):9458, 1990.

[71] A. Genoese, A. Genoese, N. L. Rizzi, and G. Salerno. On the derivation of the elastic properties of lattice nanostructures: the case of graphene sheets. *Composites Part B: Engineering*, 115:316–329, 2017.

[72] J. L. Ericksen. On the Cauchy-Born rule. *Mathematics and Mechanics of Solids*, 13(3-4):199–220, 2008.

[73] Y. Sun and K. M. Liew. Mesh-free simulation of single-walled carbon nanotubes using higher order Cauchy-Born rule. *Computational Materials Science*, 42(3):444–452, 2008.

[74] C. D. Reddy, S. Rajendran, and K. M. Liew. Equilibrium configuration and continuum elastic properties of finite sized graphene. *Nanotechnology*, 17(3):864, 2006.

[75] R. Ansari, A. Shahabodini, and H. Rouhi. Prediction of the biaxial buckling and vibration behavior of graphene via a nonlocal atomistic-based plate theory. *Composite Structures*, 95:88–94, 2013.

[76] X. Guo, J. Liao, and X. Wang. Investigation of the thermo-mechanical properties of single-walled carbon nanotubes based on the temperature-related higher order Cauchy-Born rule. *Computational Materials Science*, 51(1):445–454, 2012.

[77] H. Jiang, P. Zhang, B. Liu, Y. Huang, P. H. Geubelle, H. Gao, and K. C. Hwang. The effect of nanotube radius on the constitutive model for carbon nanotubes. *Computational Materials Science*, 28(3-4):429–442, 2003.

[78] M. Arroyo and T. Belytschko. Finite crystal elasticity of carbon nanotubes based on the exponential Cauchy-Born rule. *Physical Review B*, 69(11):115415, 2004.

[79] X. Guo, J. B. Wang, and H. W. Zhang. Mechanical properties of single-walled carbon nanotubes based on higher order Cauchy-Born rule. *International Journal of Solids and Structures*, 43(5):1276–1290, 2006.

[80] T. Belytschko, S. P. Xiao, G. C. Schatz, and R. S. Ruoff. Atomistic simulations of nanotube fracture. *Physical Review B*, 65(23):235430, 2002.

[81] F. Scarpa, S. Adhikari, and A. S. Phani. Effective elastic mechanical properties of single layer graphene sheets. *Nanotechnology*, 20(6):065709, 2009.

[82] F. Scarpa, S. Adhikari, and R. Chowdhury. The transverse elasticity of bilayer graphene. *Physics Letters A*, 374(19-20):2053–2057, 2010.

[83] M. Meo and M. Rossi. Prediction of Young's modulus of single wall carbon nanotubes by molecular-mechanics based finite element modelling. *Composites Science and Technology*, 66(11-12):1597–1605, 2006.

[84] J. R. Xiao, B. A. Gama, and J. W. Gillespie Jr. An analytical molecular structural mechanics model for the mechanical properties of carbon nanotubes. *International Journal of Solids and Structures*, 42(11-12):3075–3092, 2005.

[85] C. Baykasoglu and A. Mugan. Nonlinear fracture analysis of single-layer graphene sheets. *Engineering Fracture Mechanics*, 96:241–250, 2012.

[86] B. I. Costescu, I. B. Baldus, and F. Gräter. Graphene mechanics: I. efficient first principles based morse potential. *Physical Chemistry Chemical Physics*, 16(24):12591–12598, 2014.

[87] Z. Ni, H. Bu, M. Zou, H. Yi, K. Bi, and Y. Chen. Anisotropic mechanical properties of graphene sheets from molecular dynamics. *Physica B*, 405(5):1301–1306, 2010.

[88] Y. Gao and P. Hao. Mechanical properties of monolayer graphene under tensile and compressive loading. *Physica E*, 41(8):1561–1566, 2009.

[89] M. Xu, J. T. Paci, J. Oswald, and T. Belytschko. A constitutive equation for graphene based on density functional theory. *International Journal of Solids and Structures*, 49(18):2582–2589, 2012.

[90] Q. Lu and R. Huang. Nonlinear mechanics of single-atomic-layer graphene sheets. *International Journal of Applied Mechanics*, 1(03):443–467, 2009.

[91] S. Singh and B. P. Patel. Nonlinear elastic properties of graphene sheet under finite deformation. *Composite Structures*, 119:412–421, 2015.

[92] P. Zhang, Y. Huang, P. H. Geubelle, P. A. Klein, and K. C. Hwang. The elastic modulus of single-wall carbon nanotubes: a continuum analysis incorporating interatomic potentials. *International Journal of Solids and Structures*, 39(13-14):3893–3906, 2002.

[93] J. Zhou and R. Huang. Internal lattice relaxation of single-layer graphene under in-plane deformation. *Journal of the Mechanics and Physics of Solids*, 56(4):1609–1623, 2008.

[94] J. B. Wang, X. Guo, H. W. Zhang, L. Wang, and J. B. Liao. Energy and mechanical properties of single-walled carbon nanotubes predicted using the higher order Cauchy-Born rule. *Physical Review B*, 73(11):115428, 2006.

[95] M. Pelliciari and A. M. Tarantino. A nonlinear molecular mechanics model for graphene subjected to large in-plane deformations. *International Journal of Engineering Science*, under review.

[96] M. Pelliciari and A. M. Tarantino. Equilibrium and stability of anisotropic hyperelastic graphene membranes. *Journal of Elasticity*, accepted.

[97] A. K. Geim and K. S. Novoselov. The rise of graphene. In *Nanoscience and Technology: a Collection of Reviews from Nature Journals*, pages 11–19. World Scientific, 2010.

[98] J. Nilsson, A. H. C. Neto, F. Guinea, and N. M. R. Peres. Electronic properties of graphene multilayers. *Physical Review Letters*, 97(26):266801, 2006.

[99] A. H. Castro Neto, F. Guinea, N. M. R. Peres, K. S. Novoselov, and A. K. Geim. The electronic properties of graphene. *RvMP*, 81(1):109–162, 2009.

[100] C. H. Lui, L. Liu, K. F. Mak, G. W. Flynn, and T. F. Heinz. Ultraflat graphene. *Nature*, 462(7271):339–341, 2009.

[101] H. Kim, A. A. Abdala, and C. W. Macosko. Graphene/polymer nanocomposites. *Macromolecules*, 43(16):6515–6530, 2010.

[102] C. Chung, Y. K. Kim, D. Shin, S. R. Ryoo, B. H. Hong, and D. H. Min. Biomedical applications of graphene and graphene oxide. *Accounts of Chemical Research*, 46(10):2211–2224, 2013.

[103] X. Zang, Q. Zhou, J. Chang, Y. Liu, and L. Lin. Graphene and carbon nanotube (CNT) in MEMS/NEMS applications. *Microelectronic Engineering*, 132:192–206, 2015.

[104] Z. H. Khan, A. R. Kermany, A. Öchsner, and F. Iacopi. Mechanical and electromechanical properties of graphene and their potential application in MEMS. *Journal of Physics D: Applied Physics*, 50(5):053003, 2017.

[105] J. Pu, Y. Mo, S. Wan, and L. Wang. Fabrication of novel graphene-fullerene hybrid lubricating films based on self-assembly for MEMS applications. *Chemical Communications*, 50(4):469–471, 2014.

[106] Y. Zhang, H. Han, N. Wang, P. Zhang, Y. Fu, M. Murugesan, M. Edwards, K. Jeppson, S. Volz, and J. Liu. Improved heat spreading performance of functionalized graphene in microelectronic device application. *Advanced Functional Materials*, 25(28):4430–4435, 2015.

[107] G. Ruhl, S. Wittmann, M. Koenig, and D. Neumaier. The integration of graphene into microelectronic devices. *Beilstein Journal of Nanotechnology*, 8(1):1056–1064, 2017.

[108] M. Pumera. Graphene-based nanomaterials for energy storage. *Energy & Environmental Science*, 4(3):668–674, 2011.

[109] R. Raccichini, A. Varzi, S. Passerini, and B. Scrosati. The role of graphene for electrochemical energy storage. *Nature Materials*, 14(3):271–279, 2015.

[110] H. Shen, L. Zhang, M. Liu, and Z. Zhang. Biomedical applications of graphene. *Theranostics*, 2(3):283, 2012.

[111] T. Ji, Y. Feng, M. Qin, and W. Feng. Thermal conducting properties of aligned carbon nanotubes and their polymer composites. *Composites Part A: Applied Science and Manufacturing*, 91:351–369, 2016.

[112] M. Tarfaoui, K. Lafdi, and A. El Moumen. Mechanical properties of carbon nanotubes based polymer composites. *Composites Part B: Engineering*, 103:113–121, 2016.

[113] X. Sun, H. Sun, H. Li, and H. Peng. Developing polymer composite materials: carbon nanotubes or graphene? *Advanced Materials*, 25(37):5153–5176, 2013.

[114] B. Liang, Z. Song, M. Wang, L. Wang, and W. Jiang. Fabrication and thermoelectric properties of graphene/composite materials. *Journal of Nanomaterials*, 2013, 2013.

[115] Z. Pan, L. He, L. Qiu, A. H. Korayem, G. Li, J. W. Zhu, F. Collins, D. Li, W. H. Duan, and M. C. Wang. Mechanical properties and microstructure of a graphene oxide-cement composite. *Cement and Concrete Composites*, 58:140–147, 2015.

[116] G. Korznikova, T. Czeppe, G. Khalikova, D. Gunderov, E. Korznikova, L. Litynska-Dobrzynska, and M. Szlezynger. Microstructure and mechanical properties of Cu-graphene composites produced by two high pressure torsion procedures. *Materials Characterization*, 161:110122, 2020.

[117] D. G. Papageorgiou, I. A. Kinloch, and R. J. Young. Mechanical properties of graphene and graphene-based nanocomposites. *Progress in Materials Science*, 90:75–127, 2017.

[118] M. A. Rafiee, J. Rafiee, Z. Wang, H. Song, Z. Z. Yu, and N. Koratkar. Enhanced mechanical properties of nanocomposites at low graphene content. *ACS Nano*, 3(12):3884–3890, 2009.

[119] M. Fang, K. Wang, H. Lu, Y. Yang, and S. Nutt. Covalent polymer functionalization of graphene nanosheets and mechanical properties of composites. *Journal of Materials Chemistry*, 19(38):7098–7105, 2009.

[120] I. W. Frank, D. M. Tanenbaum, A. M. van der Zande, and P. L. McEuen. Mechanical properties of suspended graphene sheets. *Journal of Vacuum Science & Technology B: Microelectronics and Nanometer Structures Processing, Measurement, and Phenomena*, 25(6):2558–2561, 2007.

[121] M. Poot and H. S. J. van der Zant. Nanomechanical properties of few-layer graphene membranes. *Applied Physics Letters*, 92(6):063111, 2008.

[122] S. P. Koenig, N. G. Boddeti, M. L. Dunn, and J. S. Bunch. Ultrastrong adhesion of graphene membranes. *Nature Nanotechnology*, 6(9):543, 2011.

[123] R. Rafiee and R. M. Moghadam. On the modeling of carbon nanotubes: a critical review. *Composites Part B: Engineering*, 56:435–449, 2014.

[124] C. Y. Wang and L. C. Zhang. An elastic shell model for characterizing single-walled carbon nanotubes. *Nanotechnology*, 19(19):195704, 2008.

[125] T. Chang. A molecular based anisotropic shell model for single-walled carbon nanotubes. *Journal of the Mechanics and Physics of Solids*, 58(9):1422–1433, 2010.

[126] K. Ghorbani, A. Rajabpour, and M. Ghadiri. Determination of carbon nanotubes size-dependent parameters: Molecular dynamics simulation and nonlocal strain gradient continuum shell model. *Mechanics Based Design of Structures and Machines*, pages 1–18, 2019.

[127] S. Brischetto. A continuum shell model including van der Waals interaction for free vibrations of double-walled carbon nanotubes. *CMES-Computer Modeling in Engineering & Sciences*, 104:305, 2015.

[128] F. Khademolhosseini, R. Rajapakse, and A. Nojeh. Torsional buckling of carbon nanotubes based on nonlocal elasticity shell models. *Computational Materials Science*, 48(4):736–742, 2010.

[129] B. I. Yakobson, C. J. Brabec, and J. Bernholc. Nanomechanics of carbon tubes: instabilities beyond linear response. *Physical Review Letters*, 76(14):2511, 1996.

[130] G. M. Odegard, T. S. Gates, L. M. Nicholson, and K. E. Wise. Equivalent-continuum modeling of nano-structured materials. *Composites Science and Technology*, 62(14):1869–1880, 2002.

[131] Z. Xin, Z. Jianjun, and O. Y. Zhong Can. Strain energy and Young's modulus of single-wall carbon nanotubes calculated from electronic energy-band theory. *Physical Review B*, 62(20):13692, 2000.

[132] K. I. Tserpes and P. Papanikos. Finite element modeling of single-walled carbon nanotubes. *Composites Part B: Engineering*, 36(5):468–477, 2005.

[133] A. Sakhaee-Pour. Elastic properties of single-layered graphene sheet. *Solid State Communications*, 149(1-2):91–95, 2009.

[134] C. D. Reddy, A. Ramasubramaniam, V. B. Shenoy, and Y. W. Zhang. Edge elastic properties of defect-free single-layer graphene sheets. *Applied Physics Letters*, 94(10):101904, 2009.

[135] L. Shen, H. S. Shen, and C. L. Zhang. Temperature-dependent elastic properties of single layer graphene sheets. *Materials & Design*, 31(9):4445–4449, 2010.

[136] S. S. Gupta and R. C. Batra. Elastic properties and frequencies of free vibrations of single-layer graphene sheets. *Journal of Computational and Theoretical Nanoscience*, 7(10):2151–2164, 2010.

[137] T. Chang and H. Gao. Size-dependent elastic properties of a single-walled carbon nanotube via a molecular mechanics model. *Journal of the Mechanics and Physics of Solids*, 51(6):1059–1074, 2003.

[138] S. K. Georgantzinos, G. I. Giannopoulos, and N. K. Anifantis. Numerical investigation of elastic mechanical properties of graphene structures. *Materials & Design*, 31(10):4646–4654, 2010.

[139] I. E. Berinskii and F. M. Borodich. Elastic in-plane properties of 2D linearized models of graphene. *Mechanics of Materials*, 62:60–68, 2013.

[140] J. Hou, Z. Yin, Y. Zhang, and T. Chang. Structure dependent elastic properties of supergraphene. *Acta Mechanica Sinica*, 32(4):684–689, 2016.

[141] S. K. Georgantzinos, D. E. Katsareas, and N. K. Anifantis. Graphene characterization: a fully non-linear spring-based finite element prediction. *Physica E*, 43(10):1833–1839, 2011.

[142] A. Genoese, A. Genoese, N. L. Rizzi, and G. Salerno. On the in-plane failure and post-failure behaviour of pristine and perforated single-layer graphene sheets. *Mathematics and Mechanics of Solids*, 24(11):3418–3443, 2019.

[143] A. S. Nazarloo, M. T. Ahmadian, and K. Firoozbakhsh. On the mechanical characteristics of graphene nanosheets: a fully nonlinear modified morse model. *Nanotechnology*, 31(11):115708, 2019.

[144] Z. H. Ni, H. M. Wang, J. Kasim, H. M. Fan, T. Yu, Y. H. Wu, Y. P. Feng, and Z. X. Shen. Graphene thickness determination using reflection and contrast spectroscopy. *Nano Letters*, 7(9):2758–2763, 2007.

[145] Y. Geng, S. J. Wang, and J. K. Kim. Preparation of graphite nanoplatelets and graphene sheets. *Journal of Colloid and Interface Science*, 336(2):592–598, 2009.

[146] D. Galhofo, N. Silvestre, B. Faria, and C. Guarda. Monotonic and hysteretic in-plane behaviour of graphene through an atomistic FE model. *Composites Part B: Engineering*, 156:310–318, 2019.

[147] E. Marenić, A. Ibrahimbegovic, J. Sorić, and P. A. Guidault. Homogenized elastic properties of graphene for small deformations. *Materials*, 6(9):3764–3782, 2013.

[148] Y. G. Yanovsky, E. A. Nikitina, Y. N. Karnet, and S. M. Nikitin. Quantum mechanics study of the mechanism of deformation and fracture of graphene. *Physical Mesomechanics*, 12(5-6):254–262, 2009.

[149] M. C. Wang, C. Yan, L. Ma, N. Hu, and M. W. Chen. Effect of defects on fracture strength of graphene sheets. *Computational Materials Science*, 54:236–239, 2012.

[150] H. Zhao, K. Min, and N. R. Aluru. Size and chirality dependent elastic properties of graphene nanoribbons under uniaxial tension. *Nano Letters*, 9(8):3012–3015, 2009.

[151] R. Ansari, B. Motevalli, A. Montazeri, and S. Ajori. Fracture analysis of monolayer graphene sheets with double vacancy defects via MD simulation. *Solid State Communications*, 151(17):1141–1146, 2011.

[152] Z. Xu. Graphene nano-ribbons under tension. *Journal of Computational and Theoretical Nanoscience*, 6(3):625–628, 2009.

[153] T. Shao, B. Wen, R. Melnik, S. Yao, Y. Kawazoe, and Y. Tian. Temperature dependent elastic constants and ultimate strength of graphene and graphyne. *The Journal of Chemical Physics*, 137(19):194901, 2012.

[154] F. Liu, P. Ming, and J. Li. *Ab initio* calculation of ideal strength and phonon instability of graphene under tension. *Physical Review B*, 76(6):064120, 2007.

[155] M. Z. Hossain, T. Ahmed, B. Silverman, M. S. Khawaja, J. Calderon, A. Rutten, and S. Tse. Anisotropic toughness and strength in graphene and its atomistic origin. *Journal of the Mechanics and Physics of Solids*, 110:118–136, 2018.

[156] J. W. Jiang, T. Chang, X. Guo, and H. S. Park. Intrinsic negative Poisson's ratio for single-layer graphene. *Nano Letters*, 16(8):5286–5290, 2016.

[157] Z. Qin, G. Qin, and M. Hu. Origin of anisotropic negative Poisson's ratio in graphene. *Nanoscale*, 10(22):10365–10370, 2018.

[158] Y. Wang, J. Lei, and Z. Liu. Molecular dynamics study on the anisotropic Poisson's ratio of the graphene. *Diamond and Related Materials*, 93:66–74, 2019.

[159] G. Qin and Z. Qin. Negative Poisson's ratio in two-dimensional honeycomb structures. *npj Computational Materials*, 6(1):1–6, 2020.

[160] E. A. Kearsley. Asymmetric stretching of a symmetrically loaded elastic sheet. *International Journal of Solids and Structures*, 22(2):111–119, 1986.

[161] A. M. Tarantino. Asymmetric equilibrium configurations of symmetrically loaded isotropic square membranes. *Journal of Elasticity*, 69(1-3):73–97, 2002.

[162] K. I. Alzebdeh. An atomistic-based continuum approach for calculation of elastic properties of single-layered graphene sheet. *Solid State Communications*, 177:25–28, 2014.

[163] K. Z. Milowska, M. Woinska, and M. Wierzbowska. Contrasting elastic properties of heavily B-and N-doped graphene with random impurity distributions including aggregates. *The Journal of Physical Chemistry C*, 117(39):20229–20235, 2013.

[164] K. N. Kudin, G. E. Scuseria, and B. I. Yakobson. C_2F, BN, and C nanoshell elasticity from *ab initio* computations. *Physical Review B*, 64(23):235406, 2001.